

Helicity Asymmetry Measurement for π^0 Photoproduction with FROST

by Hideko Iwamoto

A Dissertation submitted to
The Faculty of
The Columbian College of Arts and Sciences
of The George Washington University
in partial fulfillment of the requirements for the degree of
Doctor of Philosophy

August 15, 2011

Dissertation directed by

William Briscoe

Professor of Physics

The Columbian College of Arts and Sciences of The George Washington University certifies that Hideko Iwamoto has passed the Final Examination for the degree of Doctor of Philosophy as of May 06, 2011. This is the final and approved form of the dissertation.

Hideko Iwamoto

Helicity Asymmetry Measurement for π^0 Photoproduction with FROST

Dissertation Research Committee:

William Briscoe, Professor of Physics, Dissertation Director

Donald Lehman, Professor of Physics, Committee Member

Allena Opper, Professor of Physics, Committee Member

Helmut Haberzettl, Associate Professor of Physics, Committee Member

Mark Paris, Assistant Research Professor of Physics, Committee Member

Franz Klein, Associate Professor of Physics (The Catholic University of America), Committee Member

©Copyright 2011 by Hideko Iwamoto

All rights reserved

Abstract of Dissertation

Helicity Asymmetry Measurement for π^0 Photoproduction with FROST

This thesis reports on the first helicity asymmetry measurement for single neutral pion photoproduction using the CLAS detector in Hall B at the Thomas Jefferson National Accelerator Facility (JLab). This measurement used longitudinally polarized protons and circularly polarized photons at energies between 350 MeV and 2400 MeV. The experimental results are compared to three available model calculations.

The target used in this experiment was butanol (C_4H_9OH). The protons in the target were polarized via the Dynamical Nuclear Polarization (DNP) technique. During the experiment, the target polarization was kept between 78% and 92%. The relaxation time of the target polarization was about 2,000 hours during the experiment. The photon beam was produced by the photon tagging system in Hall B. Two different electron beam energies, 1.465 GeV and 2.478 GeV, with a longitudinal electron polarization between 80 ~ 87% were used to produce the circularly polarized photon beam on a thin gold radiator. An additional carbon target, positioned downstream of the butanol target, was used to subtract the background from bound-nucleon reactions.

The helicity asymmetry E was measured with high statistics of about 12 Million events using the missing mass technique. The result is in good agreement with model calculations up to $E_\gamma = 1.35$ GeV. However, significant deviations are observed at the backward pion scattering angles, $-0.75 \leq \cos \theta \leq 0$.

The helicity asymmetry is very sensitive to various dynamical reaction effects, such as channel coupling and final state interactions. Therefore, the new data will help to constrain the parameters of the theoretical models.

Table of Contents

Abstract of Dissertation	iv
Table of Contents	v
List of Figure	vii
List of Table	x
chapter 1 Introduction	1
1.1 Quantum chromodynamics	2
1.2 Baryons in QCD	5
1.3 Experimental methods	8
chapter 2 Resonance and Models	12
2.1 Partial wave representation	12
2.2 Unitarity	13
2.3 Resonance phenomena	14
2.4 Models	17
chapter 3 Double polarization observables and FROST experiments	20
3.1 Helicity amplitudes	21
3.2 CGLN amplitudes	22
3.3 Spin observables	25
3.4 Rules for observables	27
3.5 FROST experiment	29
chapter 4 Experimental Facility	37
4.1 The facility	37
4.2 CLAS	38
4.3 Electron beam	50
4.4 Photon beam	52
4.5 Data acquisition	55

chapter 5	Data Analysis 1: Event Selection	58
5.1	Data reduction procedure	58
5.2	Event reconstruction for the $p\pi^0$ final state	60
5.3	Missing-mass squared cut	74
5.4	Event vertex and selection of targets	75
5.5	Missing mass sorted by different helicity states and targets . . .	77
chapter 6	Data Analysis 2: Helicity Asymmetry Extraction	83
6.1	Helicity asymmetry E	83
6.2	Run periods	84
6.3	Extraction of asymmetry E	85
chapter 7	Statistical and systematic uncertainties	94
7.1	Statistical uncertainties	94
7.2	Systematic uncertainties	96
chapter 8	Result/Discussion	107
8.1	Events and polarizations for $\pi^0 p$ channel	107
8.2	Result of measured asymmetry E	109
8.3	Summary	134
	Appendices	146

List of Figures

Figure 1.1	Screening of the charges	3
Figure 1.2	Ground-state baryons	9
Figure 1.3	Total cross section data of meson production	10
Figure 2.1	Resonant part of the phase shift	15
Figure 2.2	Some of the singularities of $S_l(k)$ in the complex k plane	16
Figure 3.1	Degree of circular polarization of photon	33
Figure 3.2	Side view of the FROST cryostat	34
Figure 3.3	Trend of the polarization of the butanol target	36
Figure 4.1	Schematic layout of the CEBAF accelerator	38
Figure 4.2	CEBAF Large Acceptance Spectrometer (CLAS)	39
Figure 4.3	Drift Chamber	42
Figure 4.4	Section through Region 3 of the drift chamber	43
Figure 4.5	Photograph of CLAS	44
Figure 4.6	Start counter	46
Figure 4.7	Čerenkov counter and an electron track through it	48
Figure 4.8	Forward electromagnetic calorimeter	49
Figure 4.9	Large angle calorimeter	50
Figure 4.10	Beamline components in Hall B	51
Figure 4.11	Tagging spectrometer in cross-section	57
Figure 5.1	Momentum vs. beta for the all positive particles	61
Figure 5.2	Momentum vs. beta difference before the 3σ cut	62
Figure 5.3	beta difference for different momentum intervals	63
Figure 5.4	beta difference vs. momentum and beta vs. momentum	64
Figure 5.5	Mass of positive particles	65
Figure 5.6	Angular distribution of proton	66
Figure 5.7	ϕ and θ distribution after the fiducial cuts	67

Figure 5.8	Number of photons	68
Figure 5.9	Time differences before and after the cut	69
Figure 5.10	Proton mass	70
Figure 5.11	β distribution before and after the energy loss correction	70
Figure 5.12	$\Delta\beta$ and ΔE distributions of proton	71
Figure 5.13	Angles of pion and proton in the laboratory system	72
Figure 5.14	ϕ dependence of the missing mass	74
Figure 5.15	Missing-mass squared distribution	75
Figure 5.16	ϕ dependence of the missing mass	76
Figure 5.17	Positions of butanol, carbon, and polyethylene	77
Figure 5.18	Vertices position of three targets	78
Figure 5.19	Missing-mass distributions (1)	79
Figure 5.20	Missing-mass distributions (2)	80
Figure 5.21	Helicity difference vs. missing mass	81
Figure 6.1	Event ratio between butanol and carbon targets	86
Figure 6.2	Peaks in sector 6	87
Figure 6.3	Some of the scale factors from sectors 1 and 6	89
Figure 6.4	Negative missing-mass squared	90
Figure 6.5	Missing-mass squared for different sectors	91
Figure 6.6	Application of norm factor to the number of events	92
Figure 6.7	Dilution factor	92
Figure 7.1	Systematic error by the fiducial cut	98
Figure 7.2	Systematic error of missing-mass squared cut	99
Figure 7.3	Systematic error of the vertex cut	100
Figure 7.4	Dilution factor in case 1	101
Figure 7.5	Some of the points of asymmetry E in case 1	101
Figure 7.6	Uncertainty in case 1	102
Figure 7.7	Range of the scale factor in case 2	103
Figure 7.8	Dilution factor in case 2	103
Figure 7.9	Uncertainty in case 2	104
Figure 7.10	Dilution factors by sector in case 3	105
Figure 7.11	Uncertainty in case 3	106
Figure 8.1	Number of events	108
Figure 8.2	Asymmetry E for all groups in the different E_γ (1)	110

Figure 8.3	Asymmetry E for all groups in the different E_γ (2)	111
Figure 8.4	Asymmetry E for all groups in the different E_γ (3)	112
Figure 8.5	Asymmetry E for all groups in the different E_γ (4)	114
Figure 8.6	Asymmetry E for all groups in the different E_γ (5)	115
Figure 8.7	Asymmetry E for all groups in the different E_γ (6)	116
Figure 8.8	Asymmetry E for all groups in the different E_γ (7)	117
Figure 8.9	Asymmetry E for all groups in the different E_γ (8)	118
Figure 8.10	Asymmetry E for all groups in the different E_γ (9)	119
Figure 8.11	Asymmetry E for all groups in the different E_γ (10)	120
Figure 8.12	Polarization of the photon beams	121
Figure 8.13	Asymmetry E: group 1 ~ 3 vs. group 4 ~ 7 (1)	123
Figure 8.14	Asymmetry E: group 1 ~ 3 vs. group 4 ~ 7 (2)	124
Figure 8.15	Asymmetry E: group 1 ~ 3 vs. group 4 ~ 7 (3)	125
Figure 8.16	Asymmetry E: group 1 ~ 3 vs. group 4 ~ 7 (4)	126
Figure 8.17	Asymmetry E for all groups in the different $\cos\theta$ (1)	127
Figure 8.18	Asymmetry E for all groups in the different $\cos\theta$ (2)	128
Figure 8.19	Asymmetry E for all groups in the different $\cos\theta$ (3)	129
Figure 8.20	Asymmetry E for all groups in the different $\cos\theta$ (4)	130
Figure 8.21	Asymmetry E for all groups in the different $\cos\theta$ (5)	131
Figure 8.22	Asymmetry E for all groups in the different $\cos\theta$ (6)	132
Figure 8.23	Asymmetry E for all groups in the different $\cos\theta$ (7)	133
Figure 8.24	Asymmetry E: FROST vs. MAMI (1)	135
Figure 8.25	Asymmetry E: FROST vs. MAMI (2)	136

List of Tables

Table 1.1	The faces of QCD	4
Table 1.2	Nucleon resonances	6
Table 1.3	Physical Baryons	8
Table 3.1	Basic properties of π	20
Table 3.2	Helicity Amplitudes	21
Table 3.3	Observables in the Double polarization	25
Table 3.4	Spin observables	26
Table 3.5	Triggers for observables E and G	31
Table 3.6	Polarization of the electron beam	32
Table 4.1	Summary of the CLAS detector characteristics	40
Table 4.2	CLAS electron beam properties	52
Table 5.1	Maximum scattering angles of proton	73
Table 5.2	Location of three targets	77
Table 6.1	Polarization status of each run period	85
Table 7.1	Statistical uncertainties	96
Table 7.2	Systematic errors	106
Table 8.1	Number of events in each period	107
Table 8.2	Polarization and events (1.645 GeV and 2.478 GeV) . . .	138
Table 8.3	Polarization and events (Total)	139
Table 8.4	Comparison between FROST and MAMI	140
Table A.1	Spin observables (1)	148
Table A.2	Spin observables (2)	149

Chapter 1

Introduction

Matter is thought to be made up from two types of fundamental and structureless particles, leptons and quarks. Charged leptons, for example electrons, interact via electromagnetic and weak forces, where the exchange particles are bosons such as photons. Quarks interact strongly via exchange of gluons with three different types of associated charges, so-called color charges. The quarks bind through strong interactions and form two different types of hadrons: mesons (e.g. pion, kaon) and baryons (e.g. proton, neutron). However, these processes are not fully understood. The strong interactions of colored quarks and gluons are described in Quantum Chromodynamics (QCD). The charges in QCD have three different colors and the colored gluons interact with each other. Additionally, a large coupling constant α_s in the low energy regime prevents us from using perturbation theory.

Baryons are composed of three quarks. The study of their excited states, the so-called baryon resonances, is one of the ways to investigate the structure of hadronic system. The experimental method for studying the structure of hadrons is generally through elastic and inelastic scattering. Since the 1960's, a huge amount of data were taken with unpolarized or singularly polarized experiments. However, more sophisticated experiments are necessary to extract its different features. Baryon resonances are unstable states and their lifetimes are so short that resonances can not be observed.

Resonance experiments have been performed by many collaborations, such as A2 (Germany), GRAAL (France), CLAS (USA), where enormous amounts of meson productions data with high precision have been accumulated. For the theoretical approach, one of the key methods in the low-energy regime, where the perturbation theory does not work, is lattice QCD. Lattice QCD is based on path integrals and provides exact numerical solutions for the strong

interaction.

This thesis reports on the experimental results for helicity asymmetry E for neutral pion photoproduction, measured in Hall B at JLab using the CLAS detector. In this experiment a circularly polarized beam and a longitudinally polarized target were used. In this thesis the angular distribution of the neutral pion is studied as a function of photon beam energy, E_γ and as function of the center-of-mass energy, W .

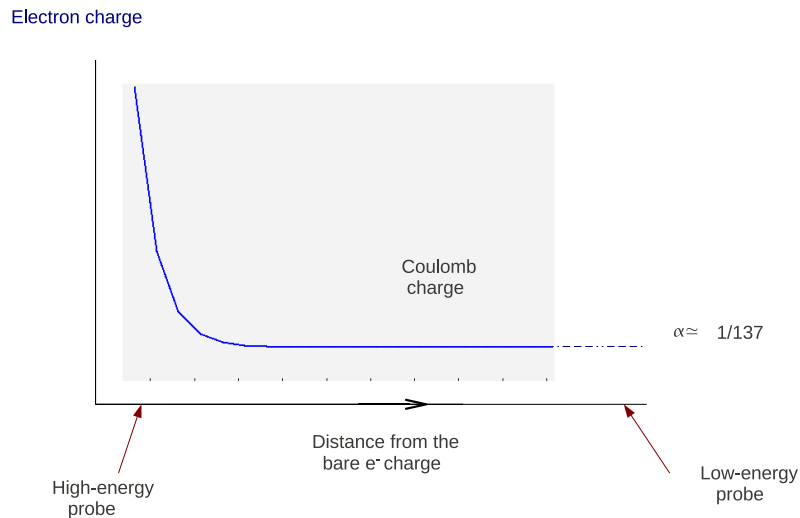
Single and double polarization experiments are very important since they allow for extracting the helicity amplitudes without any ambiguities if the set of measurements is carefully selected. These helicity amplitudes can be decomposed into partial waves or electric and magnetic multipoles. Since each resonance decays to different particles or channels, resonances can be reconstructed from partial waves of these decay channels with their form factors. Thus, these single and double polarization measurements enable us to construct baryon resonances.

The following sections will give short descriptions of QCD, quark models, and experimental methods for the study of resonances.

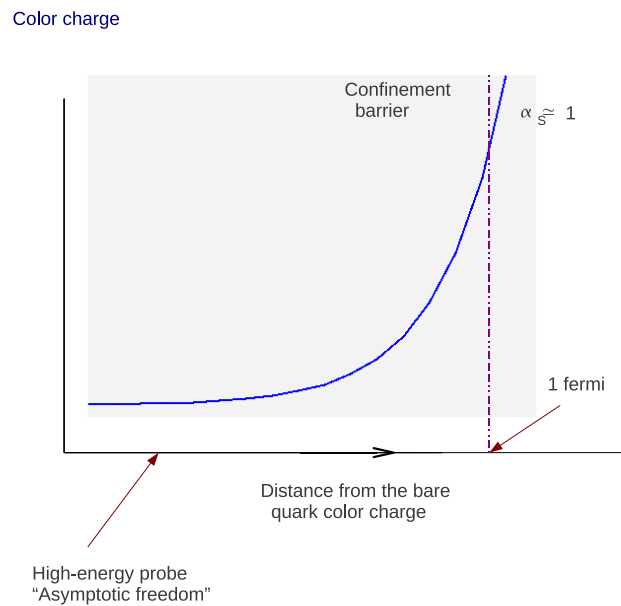
1.1 Quantum chromodynamics

Quantum Chromodynamics (QCD) is the fundamental theory of strong interaction. It is a non-abelian gauge theory, in which the generators do not commute with each other. Therefore, the equations of motion are nonlinear in the vector field and the vector bosons, gluons, interact with each other, unlike photons in electromagnetic interactions.

Hadrons, such as p, n, π or K are composite particles and are categorized into two families: mesons and baryons. Mesons are composed of a quark and an antiquark pair surrounded by a sea of gluons and other quark and anti-quark pairs. Baryons are composed of three quarks surrounded by a similar sea. Quarks in nucleons are bound by gluons, which are bosons. The crucial difference of magnitudes of couplings between QCD and QED, Quantum Electrodynamics, is shown in Figure 1.1. In QED, the strength of the Coulomb field decreases with distance. On the other hand, in QCD, if a single quark is attempted to be removed from a meson (or baryon), the energy increases with the distance between quarks. The quark will be separated from its neighbors



(a) QED



(b) QCD

Figure 1.1: Screening of the (a) electronic and (b) color charge in quantum field theory[1].

until the energy between them becomes big enough to create a quark-antiquark pair. This property of quarks is called “confinement”.

Features of QCD are summarized in Table 1.1. The coupling of QCD, α_s , becomes small at sufficiently high energies. This is called “asymptotic freedom”, a regime where perturbation theory can be used. In contrast to the electromagnetic coupling, the color coupling becomes large at low energies (confinement). In the high energy or short distance regime, QCD has been thoroughly tested but the confinement regime remains a challenge. QCD is

Table 1.1: The faces of QCD

Regime (Degree of freedom)	Feature	Theory	Experiment
high energies/ short distances (quarks and gluons)	small α_s “asymptotic freedom” (weak QCD) → perturbative in α_s (Feynman diagram)	pQCD	DIS
low energies/ long distances (hadrons (p, n, $\Delta, \pi, \rho \dots$))	large α_s “confinement” (strong QCD)	lattice QCD	resonance experiment

unsolved in the confinement regime where the coupling strength is too large to permit perturbative methods to be used. One of the central problems in nuclear physics remains the connection of observed properties of the hadrons to the underlying theoretical framework of QCD. The solution requires advances in both theory and experiment.

In the absence of analytic solutions to QCD, lattice gauge theories provide the most promising approach for theoretical predictions of properties of the hadronic ground states and also their excited states. In a few specific cases, Lattice QCD, in combination with Chiral perturbation theory, has allowed the extrapolation of full lattice simulations to physical quark masses. Thus, it provides a direct comparison with experimental observables. However, lattice QCD calculations require enormous computational power, and are still far

from being able to find solutions for low and intermediate energy scattering reactions.

1.2 Baryons in QCD

A large number of nucleon resonances has been observed experimentally. These resonances could be accounted for by the dynamics of three confined valence quarks. Isgur and Karl[2, 3] used the basis generated by an oscillator potential to diagonalize the hyperfine and the tensor one-gluon exchange potentials. This is a highly successful model in spectroscopy and baryon structure. It is not clear why a nonrelativistic model is so successful because the motion of light quarks should be relativistic.

In the simplest relativistic versions of the quark model, the motion of the quarks, confined in a static potential or cavity, is governed by the Dirac equation. Bogolioubov[4] considered the single-particle solutions of the Dirac equation in a spherical cavity of fixed radius. This evolved into the M.I.T. bag model of the nucleon[5, 6]. The relativistic shell model of the nucleon, with potentials of other shapes has also been studied by Leal Ferreira et al.[7], Weise[8], and others.

1.2.1 Baryon resonances

A large number of excited states of the nucleon have been identified in the energy range of $1 \sim 3$ GeV. These excited states decay strongly to their ground states, and typically have a width in the range of $100 \sim 300$ MeV. Consequently, the resonances overlap considerably with increasing excitation energy¹.

Nucleon resonances were mostly found in $N\pi$ scattering and in pion photo- and electroproduction. Strong interactions have only two independent scatter-

¹Resonances exist very short times. For example, the P_{11} , N(1440) state, Breit-Wigner full width is about 300 MeV ($\Gamma \simeq 300$ MeV). The mean life time, τ , is

$$\tau = \frac{\hbar}{\Gamma} = \frac{\hbar}{0.3\text{GeV}} = \frac{\hbar c}{0.3\text{GeV} \cdot c} \simeq \frac{200\text{MeV fm}}{300\text{MeV} \times 3 \times 10^8\text{m/s}} = \frac{2}{9} \times 10^{-23}\text{s} \simeq 10^{-24}\text{s}. \quad (1.1)$$

$\Gamma/\hbar = 1/\tau$ is a transition rate for the resonance to decay into particles.

ing amplitudes corresponding to the isospin $I = 1/2$ and $I = 3/2$ (independent of the third component I_3). A few low-lying prominent resonances are visible in the total πN cross section as a function of the center of mass energy $W \left[= \sqrt{s} = \sqrt{(p_\pi + p_N)^2} \right]$. However, the majority of resonances were found through careful partial wave analysis of the data. This analysis comprises of a partial wave decomposition of the scattering amplitude. Since a unique set of partial wave parameters cannot be extracted from the data alone, it is necessary to apply theoretical constraints of analyticity through dispersion relations. Each partial wave is analyzed using a smoothly varying background term and Breit-Wigner type resonance terms. Table 1.2 shows the Breit-Wigner con-

Table 1.2: Nucleon resonances. **** denotes the existence is certain, *** denotes the existence is from very likely to certain, ** the evidence of existence is only fair, and * the evidence of existence is poor.

Particle	$L_{2I,2J}$	BW mass	BW width	decay to $N\pi$	status
N(1440)	P_{11}	1440	300	$0.55 \sim 0.75$	****
N(1520)	D_{13}	1520	115	$0.55 \sim 0.65$	****
N(1535)	S_{11}	1535	150	$0.35 \sim 0.55$	****
N(1650)	S_{11}	1655	165	$0.60 \sim 0.95$	****
N(1675)	D_{15}	1675	150	$0.35 \sim 0.45$	****
N(1700)	D_{13}	1700	100	$0.05 \sim 0.15$	***
N(1710)	P_{11}	1710	100	$0.10 \sim 0.20$	***
N(1720)	P_{13}	1720	200	$0.10 \sim 0.20$	****
N(1900)	P_{13}	1900	-	-	**
N(2080)	D_{13}	2080	-	-	**
N(2090)	S_{11}	2090	-	-	*
$\Delta(1232)$	P_{33}	1232	118	1.00	****
$\Delta(1600)$	P_{33}	1600	350	$0.10 \sim 0.25$	***
$\Delta(1620)$	S_{31}	1630	145	$0.20 \sim 0.30$	****
$\Delta(1700)$	D_{33}	1700	300	$0.10 \sim 0.20$	****
$\Delta(1750)$	P_{31}	1750	-	-	*
$\Delta(1900)$	S_{31}	1900	200	$0.10 \sim 0.30$	**

ventional masses, widths, ratios of decay to $N\pi$, and the status estimated by the particle data group[9]. The lower-mass resonances have three- or four-star status, which denote the existence of these resonances to be certain or very

likely certain. However, the status of higher-mass resonances is typically one- or two-star, which denotes the existence of these particles to be poor or only fair.

Reaction models that provide means to extract resonance properties are described in chapter 2 and are compared to our experimental results in chapter 8.

1.2.2 Constituent quark model

Overwhelming experimental evidence has shown that nucleons are composite particles. In 1964, Gell-Mann and Zweig proposed the quark model that explained hadrons not as elementary particles but composed of quarks and antiquarks. The quark model, which was based upon approximate flavor SU(3) symmetries among strongly interacting particles, organized a large number of hadrons very well and had success in predicting new hadronic states. Despite the phenomenological success of the original quark model, it had two serious problems. First, no free particles with fractional charge were found. Second, the model contradicted the expectation that quarks should obey Fermi-Dirac statistics. For example, the wave functions of baryons, which are fermions and have three quarks, were totally symmetric under the interchange of the quark spin and flavor quantum numbers. To solve these problems, Han and Nambu, Greenberg, and Gell-Mann proposed that quarks carry an additional unobserved quantum number called color. The property of color had been described by non-abelian gauge theories.

The model originally arose from the analysis of symmetry patterns using group theory. In the standard nonrelativistic quark model, the effective degrees of freedom are three equivalent constituent quarks: up, down, and strange. These constituent quarks are valence quarks, contributions from gluons and sea quarks are adapted in the large effective masses of these valence quarks. The model is also motivated by one gluon exchange and is independent of flavor. Quarks are strongly interacting fermions with spin 1/2, positive parity, and the additive baryon number 1/3. The electric charge Q is related to the quark's quantum numbers through the generalized Gell-Mann-Nishijima formula

$$Q = I_3 + \frac{\mathcal{B} + S}{2}. \quad (1.2)$$

where I_3 , \mathcal{B} , and S are the third component of isospin, the baryon number, and the strangeness of the quark, respectively. Up and down quarks are assumed to have the same mass and the color part of their wave functions is completely antisymmetric. According to the quark model, quarks bound together in different ways and make hadrons.

In the case of baryons, the total number of possible combinations of three quarks is 27. Since the quarks are fermions, the state function must be antisymmetric under interchange of any two equal mass quarks. Thus it can be written as

$$|qqq\rangle_A = |color\rangle_A \times |space, spin, flavor\rangle_S \quad (1.3)$$

where the subscripts S and A indicate symmetry or antisymmetry under interchange of any two equal-mass quarks. It is antisymmetric in color and overall symmetric in space, spin and flavor structure. The resultant ground-state baryons are octet with spin 1/2 and decuplet with spin 3/2, which are based on quark and antiquark multiplets, as seen in Figure 1.2. Table 1.3 shows

Multiplet	Baryons	s	I_3	S
Octet	N	1/2	1/2	0
	Λ	1/2	0	-1
	Σ	1/2	1	-1
	Ξ	1/2	1/2	-2
Decuplet	Δ	3/2	3/2	0
	Σ^*	3/2	1	-1
	Ξ^*	3/2	1/2	-2
	Ω^*	3/2	0	-3

Table 1.3: Physical Baryons as members of the multiplets, octet and decuplet.

baryons and quantum numbers of octet and decuplet.

1.3 Experimental methods

In atomic physics, the study of excited states of hydrogen is closely linked to the development of the theories and understanding the atom. This led into the Balmer series, the Schrödinger equation, the Dirac equation, and Lamb shift.

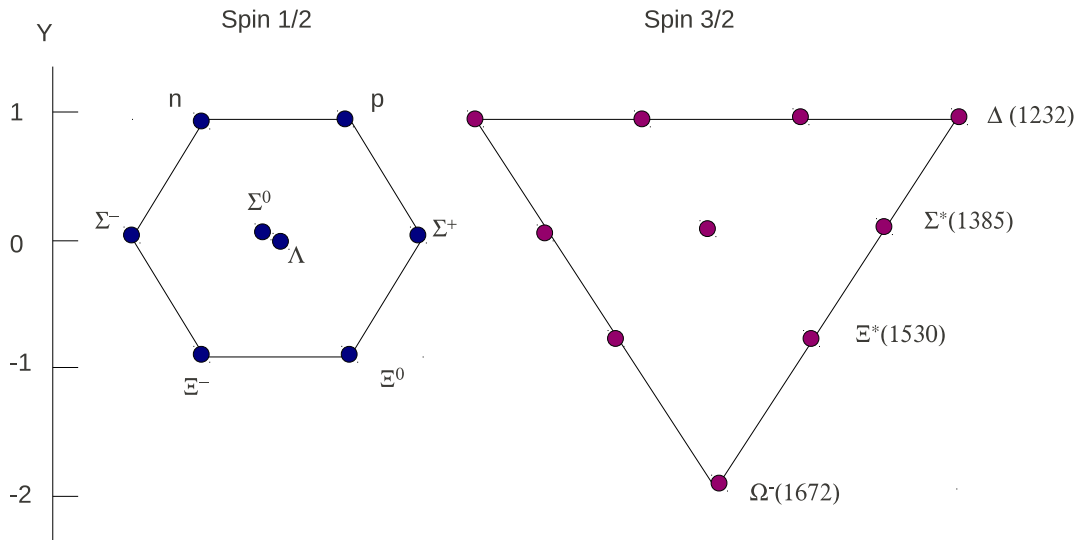


Figure 1.2: Ground-state baryons: octet and decuplet [1].

However, nuclear physics is more complex than atomic physics. The study of nucleon resonance is similar to that of nuclear resonance: using high-energy particles, such as electrons and pions, to impinge the targets and analyze the outgoing particles. In 1951, Fermi and his collaborators discovered the proton excited state for the first time. They observed a peak in the cross section measuring the scattering of pions from protons. From this result, Brueckner suggested that this behavior could be explained as an excited nucleon state with spin 3/2 [10].

Most of the experiments have been performed for the meson-induced reactions since the 1960's. The development of high-duty electron beams and detectors over the past few decades has led to an increase in the electro- and photoproduction data.

Figure 1.3 shows the total cross sections of meson production in γp reac-

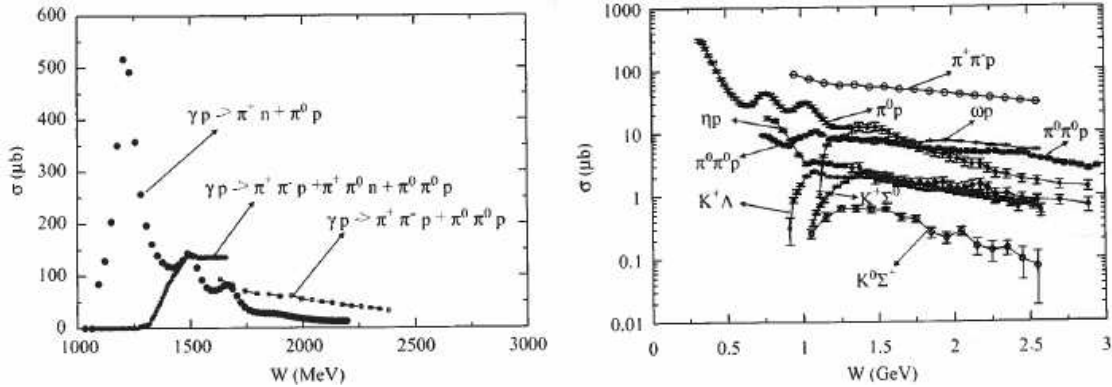


Figure 1.3: Total cross section data of meson production in γp reaction. Left: Comparison of 1- π and 2- π production. Right: $KY(K^+\Lambda, K^+\Sigma^0, K^0\Sigma^+)$, ηp and ωp production are compared with 1- π and 2- π production [11].

tions. The figure shows that single pion photoproductions dominate the photoabsorption cross section up to $W \simeq 1400$ MeV, but above $W \simeq 1400$ MeV, two pion production channels dominate. Pion photoproduction has been analyzed for a long time in order to extract the photo-decay amplitudes associated with N^* and Δ^* resonances.

Over the past twenty years, the high-precision data for electromagnetic meson production have been extensively accumulated by collaborations, such as A2 (MAMI, Mainz, Germany), CLAS (CEBAF, Newport News, USA), Crystal Barrel (ELSA, Bonn, Germany), GRAAL (ESRF, Grenoble, France), LEGS (BNL, Upton, USA), LEPS (SPring-8, Hyogo, Japan), PHOENICS (ELSA, Bonn, Germany), SAPHIR (ELSA, Bonn, Germany), and others. The main purpose of all these experiments is to study nucleon resonances.

1.3.1 Double polarization experiment

Since 1960's, many hadronic experiments were performed, and the measurements of the experimental observables evolved from cross section and single-polarization experiments to double-polarization experiments. There are three types of double-spin observables: beam-target, beam-recoil, and target-recoil. These double polarization observables and also single polarization observables can be expressed by helicity amplitudes and partial waves. In chapter 3, the double polarization observables, helicity amplitudes and partial waves, the re-

lation between observables and these amplitudes will be explained in detail.

The FROST experiment is a double polarization experiment with linearly and circularly polarized photon beams and the longitudinally and transversely polarized butanol targets. Double polarization observables H , F , G , and E can be obtained with the FROST experiment. The measurement of the double polarization observable E using circularly polarized photons and longitudinally polarized protons is presented in this thesis. FROST experiment, including a description of how the beam and target were polarized, will be explained in chapter 3, and the facility used this experiment will be described in chapter 4.

In this thesis, the reaction channel $\gamma p \rightarrow \pi^0 p$ has been analyzed. To get the final results with lower uncertainties and with higher quality, it is necessary to remove backgrounds as much as possible. In chapter 5, the steps how to select the final events for the analysis will be explained.

The butanol target, which was used in the FROST experiment, contains not only free protons, but also bound nucleons. Thus, a carbon target was used to remove background reactions, the bound nucleon reactions. In chapter 6, it will be discussed how the carbon target was used and how scale and dilution factors were determined for the extraction of the helicity asymmetry E .

In chapter 7, the statistical and systematic uncertainties will be discussed. The helicity asymmetry E for $\gamma p \rightarrow \pi^0 p$ channel will be shown in detail in chapter 8, and compared with previous data, three theoretical models.

Chapter 2

Resonance and Models

A cross section sometimes becomes suddenly large with rapid changes of the phase shift in a very small range of energy without any background or smooth change of background. This phenomenon is called a resonance [12, 13]. The cross section of resonances is typically expressed by the Breit-Wigner form with a half-width $\Gamma/2$. Since the 1950's, many variety of hadron models for the baryon resonances have been developed. Even though models may have different concepts, the majority of them are able to be compared to the low-lying resonance spectra with suitable phenomenological procedures. However, their predictions are sometime quite different for higher excited states.

In this chapter, partial waves, resonances and three models, SAID, MAID, and EBAC, are studied.

2.1 Partial wave representation

The incident state of the projectile is described by a plane wave composed of states of all angular momenta. In the case of a two-body system of spinless particles, the orbital angular momentum of the interacting pair is the total angular momentum. It is conserved with a spherical potential, $V(\vec{r}) = V(r)(|\vec{r}| = r)$ for a short-ranged interaction. The incident plane wave traveling along the z -direction may be expressed in terms of a superposition of angular momentum eigenstates, l ,

$$e^{i\vec{k}\cdot\vec{z}} = e^{ikr\cos\theta} = \sum_{l=0}^{\infty} i^l (2l+1) j_l(kr) P_l(\cos\theta), \quad (2.1)$$

where $j_l(kr)$ is the spherical Bessel function. After the particle scatters from the spherical potential $V(r)$, each of the partial waves is distorted by the po-

tential. This distortion can be expressed by a single real number, the phase shift δ_l . Since the total angular momentum is conserved, each component scatters independently. The system is axially symmetric about the z -axis and the wave function does not depend on the azimuthal angle ϕ because of a central potential.

The scattered wave function may be expressed as a superposition of the incident wave and the scattered wave

$$\begin{aligned}\psi(\vec{r}) = \psi(r, \theta) &\simeq e^{ikz} + f(\theta) \frac{e^{ikr}}{r}, \\ &= \sum_{l=0}^{\infty} i^l (2l+1) j_l(kr) P_l(\cos \theta) + f(\theta) \frac{e^{ikr}}{r},\end{aligned}\tag{2.2}$$

with $\phi = 0$ (the incident plane wave travels along the z -direction), and $f(\theta)$ is the scattering amplitude,

$$f(\theta) = \frac{1}{k} \sum_{l=0}^{\infty} (2l+1) e^{i\delta_l} \sin \delta_l P_l(\cos \theta).\tag{2.3}$$

The cross section is

$$\sigma = \int \frac{d\sigma}{d\Omega} d\Omega = \int_0^\pi |f(\theta)|^2 \sin \theta d\theta \int_0^{2\pi} d\phi,\tag{2.4}$$

where all $f(\theta)$, $d\sigma/d\Omega$, and σ depend on the phase shift δ_l . The principle importance of the partial-wave series is that only a small number of the phase shifts $\delta_l(E)$ are nonzero at low energies. Thus, the infinite series of l reduces to a finite sum.

2.2 Unitarity

Unitarity is the consequences of probability conservation and has a significant property for the scattering. The probability of S matrix of finding the system in some particular final state f in the purely elastic scattering (inelasticity = 1) is given by $|S_{fi}|^2$, and the all possible final states (or different decay channels) are given by the sum of the all probabilities and this value is equal to 1. Since the S matrix operator, which contains all important information of experimental interest, consists of non-interacting part and the transition part

expressed by the T matrix, the S matrix can be written as $S = 1 + iT$. A direct consequence of the unitarity of the S matrix is the optical theorem: the imaginary part of the forward scattering amplitude is proportional to the total cross section [14]. The unitarity relation in terms of the T matrix reads [15]

$$\mathcal{T}_{fi} - \mathcal{T}_{if}^* = i \sum_n (2\pi)^4 \delta^4(P_n - P_i) \mathcal{T}_{nf}^* \mathcal{T}_{ni}. \quad (2.5)$$

The left side of Eq. (2.5) is proportional to the imaginary part of the amplitude and the states n includes an arbitrary number of particles.

The expression of Eq. (2.3) rests on the principals of rotational invariance and probability conservation. The unitarity relation for the l th partial wave is $|S_l| = 1$. During a scattering, the phase of the partial wave changes, and thus, the magnitude of the amplitude changes. The unitarity relation restricts the way in which this partial-wave amplitude changes by the phase shift. This relation can be conveniently seen in an Argand diagram for $k f_l$. In this diagram, a unitary circle with a radius $\frac{1}{2}$ is in a complex plane of $k f_l$ and the magnitude of an amplitude is measured by the length from the origin to a point which is on the circle with the angle of $2\delta_l$. In the case of inelastic scattering, an inelasticity is less than 1 and the amplitude leaves the unitary circle [9]. In both cases, if the phase shift is small the amplitude must stay near the real axis of $k f_l$. On the other hand, if the phase shift is close to $\pi/2$, the amplitude is almost purely imaginary and the magnitude of the amplitude becomes maximum. Under such a condition, the l th partial wave may be in resonance [12].

2.3 Resonance phenomena

A nucleon resonance may be produced in high energy collisions of hadronic and electromagnetic probes impinging on a nuclear target. These hadronic resonances are interpreted as excited states of the nucleon. They are unstable particle-like excitations denoted by their isospin, I , total angular momentum, J , and parity, P . The detailed character of how the nucleon can be excited gives information on the dynamics of constituents of these composite systems. Resonances have very short lifetimes, thus its decay mesons and baryons, such as π, η, K, p, n are analyzed through partial wave analysis (PWA) to extract useful information about underlying interactions. There are various theoretical approaches to resonance phenomena.

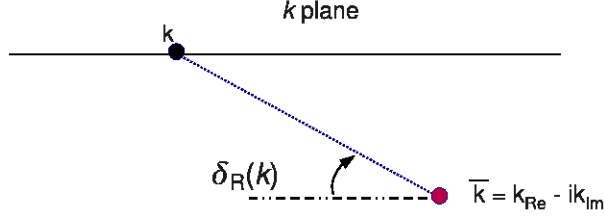


Figure 2.1: Resonant part of the phase shift, $\delta_R(k)$ [16].

Near resonance, the cross section, which is expressed by Eq. 2.4 may have a rapid variation with energy. This is related to the existence of a metastable state with energy E_R . Eq. 2.4 expresses the cross section. The partial cross section of spinless particles, which provides insight on the resonance signature without unnecessary complications associated with spin, is written by

$$\sigma_l(E) = \frac{4\pi(2l+1)}{k^2} \sin^2 \delta_l(E). \quad (2.6)$$

This partial cross section depends on the phase shift, $\delta_l(E)$. Sometimes the phase shift rises rapidly from 0 to π in a small range of E . At the same time, a rapid variation in σ_l is observed. Near the resonance energy ($E = E_R$), the phase shift consists of background (δ_{bg}) and resonance (δ_R) parts and may be written as $\delta_l(E) = \delta_{bg}(E) + \delta_R(E)$. A phase shift for the background has a smooth function of the energy.

The resonant part of the phase shift $\delta_R(p)$ is the angle shown in Figure 2.1, and is written as

$$\sin \delta_R(E) = \frac{\Gamma/2}{[(E - E_R)^2 + (\Gamma/2)^2]^{1/2}}, \quad (2.7)$$

where Γ is the width, or decay rate which is defined as:

$$\Gamma \equiv \frac{\text{Number of decay per unit time}}{\text{Number of unstable particles present}}. \quad (2.8)$$

The scattering amplitude corresponding to the phase shift, $\delta_R = \tan^{-1} \frac{\Gamma/2}{E_R - E}$ is unti-proportional to $(E - E_R + i\Gamma/2)$. In particular, in the simple case where

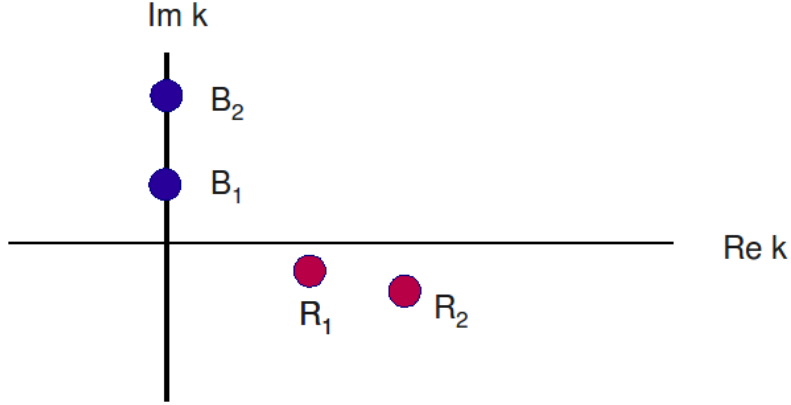


Figure 2.2: Some of the singularities of $S_l(k)$ in the complex k plane. The dots on the positive imaginary axis stand for bound state poles and the dots below the real axis stand for resonance poles. The physical (or experimentally) accessible region is along the real axis, where S_l has the form $\eta e^{2i\delta_l}$ [13].

the background phase vanishes, thus $\delta_l = \delta_R$. The partial cross section is given by:

$$\sigma_l(E) \propto \sin^2 \delta_R(E) = \frac{(\Gamma/2)^2}{(E - E_R)^2 + (\Gamma/2)^2}. \quad (2.9)$$

This is the Breit-Wigner formula and can be extracted from the wave function of a decaying state [17].

The form of the S matrix in a resonant partial wave for inelastic scattering, neglecting background ($\delta_{bg} = 0$) and with $\tan \delta_l = (\Gamma/2)/(E_R - E)$ is $S_l(k) = \eta e^{2i\delta_l}$. $S_l(k)$ is considered a function of complex E or k although both E and k are real in any experiment. Then, the resonance is considered to correspond to a pole in S_l at a complex point, $E = E_R - i\Gamma/2$ where $E_R = \hbar^2 k_R^2 / (2\mu)$ (μ is a reduced mass) as seen in Figure 2.2. When Γ is small, the pole is very close to the real axis.

If $k = i\kappa$ and $\kappa > 0$, energy E is real and have negative value ($E = \hbar^2 k^2 / 2\mu = -\hbar^2 \kappa^2 / 2\mu$). Under this condition and at some special values of κ , S_l becomes infinite number and it forms bound states [13] (see Figure 2.2). The difference between a resonance and a bound state is the sign of energy E . A resonance corresponding to a pole at $E = E_R - i\Gamma/2$ is a metastable bound state with a positive energy.

2.4 Models

The development of theoretical models for investigating electromagnetic pion production began in the 1950's. The models based on the dispersion relation approach [18, 19, 20, 21], which developed by Chew, Goldberger, Low, and Nambu, for pion-production analysis have been produced especially in the subsequent years. Since then, several different types of models have been developed. The models for the baryon resonances have to include information of dominant decay channels and possess basic properties, such as unitarity. Due to unitarity, if important channels are found, the other channels in the models will be influenced.

SAID and KSU (Kent-state university) model [22, 23, 24, 25, 26, 27, 28, 29, 30], which are based on K -matrix approach, include the most important final states, phase space and threshold effects. These models are not dynamical models, thus, the background of the reactions is not extracted and the final state particles don't have relativistic spin structures.

The isobar models [31] were developed to extract the parameters of higher mass nucleon resonance. A unitary isobar model (MAID, CB-Elsa) [32, 33, 34, 35] are based on the isobar model assuming that contributions in the relevant multipoles have Breit-Wigner forms [36] and it has the unitarized final amplitude.

The effective Lagrangian models account for the symmetries of the fundamental theory QCD. These models, however, include only effective degrees of freedom. Unitarity and analyticity in these models are involved in satisfying the physical constraints because of the complicated interaction structure. There are variety of unitary models for πN scattering using Lippmann-Schwinger equations. Dynamical models (EBAC, Juelich) [37, 38, 39, 40, 41, 42, 43, 44, 45, 46, 47, 48, 49, 50, 51, 52, 53] are the effective Lagrangian models. A dynamical coupled-channel model (EBAC) is based on an energy-independent Hamiltonian [11] using a unitary transformation method. The resulting amplitude's are written as a sum of resonant and non-resonant amplitudes.

2.4.1 SAID

The SAID k -matrix analysis is based on the parametrization of the partial-wave amplitudes, which can be written by polynomials. This parametrization is

unitary at the two-body level [54]. SAID is one of the multi-channel k-matrix¹ calculations. SAID calculates non-resonance term from the standard pseudo-scalar Born term and ρ and ω exchange [52]. The parameters are determined by fitting the data. Then, the resonance N^* parameters are extracted by fitting the resulting amplitude to a Breit-Wigner parametrization whose energies are near the resonance position.

2.4.2 MAID2007 (Unitary isobar model)

MAID unitary isobar model developed by Mainz group is one of the isobar models. This model has been modified several times since the original version, MAID98. MAID98 model was constructed with limited set of nucleon resonances described by Breit-Wigner forms. A non-resonant background was constructed from Born terms and t-channel vector meson contributions [32, 55]. Each partial wave was unitarized up to the two-pion threshold by use of Watson's theorem. MAID2007 uses the basic equations taken from the dynamical Dubna-Mainz-Taipei model [45, 56]. The background contributions are complex functions including the pion-nucleon elastic scattering amplitudes. The phase shifts and the inelasticity parameters of these elastic scattering amplitudes are taken from GWU/SAID analysis [55, 23]. The resonance contributions with Breit-Wigner forms [36] are same to the original version of MAID98, and written by

$$t_{\gamma\pi}^{R,\alpha}(E) = \bar{A}_\alpha^R(E) \frac{f_{\gamma N}(E) \Gamma_{tot} M_R f_{\pi N}(E)}{M_R^2 - W^2 - i M_R \Gamma_{tot}} e^{i\phi_R}, \quad (2.10)$$

where $f_{\gamma N}(E)$ is the form factor describing the decay of N^* [55]. This model contains thirteen resonances of four-star below 2 GeV. MAID predictions are similar to SAID in low energies, but the differences between them can be observed in the second and the third resonance regions [55].

2.4.3 Dynamical coupled-channel model

EBAC (the Excited Baryon Analysis Center) has developed a dynamical model. The dynamical model accounts for the off-shell scattering effects that

¹k-matrix is Hermitian, real, and symmetric.

can be related to the meson-baryon scattering wave functions in the short-range region.

The coupled-channel model includes the $\gamma N, \pi N, \eta N$ channels, and is expected to be valid below the onset of three pion production[11].

A set of Lagrangians describing the interactions between mesons and baryons are constrained by various well-established symmetry properties including invariance under isospin, parity, and gauge transformation. The matrix elements of the interactions are calculated from the usual Feynman amplitudes with their time components in the propagators of intermediate states defined by the three momenta of the initial and final states, as specified by the unitary transformation method. They are independent of the collision energy E . The resonant term, which is similar to the Breit-Wigner form, is defined by

$$t_{MB, M'B'}^R(k, k') = \sum_{N^*} \frac{\bar{\Gamma}_{N^*, MB}(k) \bar{\Gamma}_{M'B', N^*}(k')}{E - M_{N^*(E)} + \frac{i}{2} \Gamma_{N^*}(E)}, \quad (2.11)$$

where Γ and M_{N^*} are dressed vertex and mass parameters, respectively, and are related to self-energies. The non-resonant amplitudes and the resonant amplitudes include the states of $\pi N, \eta N, \pi \Delta, \rho N$, and σN . The sum of the non-resonant amplitudes and the resonant amplitudes can be used directly to calculate the cross sections of $\pi N \rightarrow \pi N, \eta N$ and $\gamma N \rightarrow \pi N, \eta N$ reactions.

Chapter 3

Double polarization observables and FROST experiments

The theory of photoproduction of pions has been written since the 1950's, and the general formalism for the reaction $\gamma N \rightarrow \pi N$ was developed by Chew *et al.* (CGLN amplitudes) [57, 58]. Fubin *et al.* extended the earlier predictions of low energy theorems by including the hypothesis of a partially conserved axial current(PCAC). In the late 1960's, the existing data were analyzed in terms of a multipole decomposition. The multipole amplitudes were presented up to excitation energies of 500 MeV.

The basic properties of the pion are listed in Table 3.1. The isospin symme-

Table 3.1: Basic properties of π .

	I^G	J^{PC}	Mass(MeV)	Lifetime(s)	$c\tau$ (m)	Decay modes	(%)
π^\pm	1^-	0^-	139.57	2.60×10^{-8}	7.80	$\mu\nu_\mu$	(100)
π^0	1^-	0^{-+}	134.97	8.4×10^{-17}	25.1×10^{-9}	$\gamma\gamma$ γe^+e^-	(98.8) (1.2)

try between charged and neutral pions is broken, giving rise to a mass splitting of about 5 MeV due to electromagnetic interactions, and it dramatically decreases the lifetime of neutral pions which decay $\pi^0 \rightarrow \gamma\gamma$.

The data of hadronic experiments including pion production has been accumulated since 1960's, and the experiments have been moved from measurements of unpolarized and singularly polarized observables to that of double polarized one, which needs more sophisticated technique. There are fifteen different single-spin and double-spin observables and each of them can be expressed by bilinear equations of helicity amplitudes, $H_1 \sim H_4$ (see Section 3.1).

These helicity amplitudes can be rewritten by CGLN amplitudes $\mathcal{F}_1 \sim \mathcal{F}_4$, or partial waves. The helicity amplitudes can be determined without any ambiguity if at least eight measurements of these single and double observables are performed [59]. The observables including observable E , which was analyzed in this thesis, follow rules (see Section 3.4).

In this chapter, the helicity amplitudes, the CGLN amplitudes, the relation between these amplitudes and partial waves, the rules of observables, and FROST experiment, which is a double polarization experiment using a polarized photon beam and a polarized target, will be introduced.

3.1 Helicity amplitudes

The helicity λ is the projection of the spin s onto the direction of motion of the particle. If initial and final spins are along the directions of photon beam and recoil proton in the c.m. frame, there are eight different initial- and final-helicity combinations [31, 60]. In the reaction $\gamma p \rightarrow \pi^0 p$ the total initial helicity is given by $\lambda_i = \lambda_\gamma - \lambda_{p_{target}} = \pm\frac{1}{2}, \pm\frac{3}{2}$ and total final helicity by $\lambda_f = \lambda_\pi - \lambda_{p_{recoil}} = \pm\frac{1}{2}$. Thus, there exist eight different transition amplitudes from any initial helicity state to any final helicity state. These amplitudes are so-called helicity amplitudes as seen in Table 3.2. Since they are rotationally invariant, parity and four momentum conserving, the helicity amplitudes have the symmetry properties of the interaction. The eight helicity amplitudes are related by parity and the four helicity amplitudes with $\lambda_\gamma = -1$ is simply related to the other four helicity amplitudes with $\lambda_\gamma = +1$ by the equation [31]:

$$H_{-\lambda_f, -\lambda_i} = e^{i(\lambda_i - \lambda_f)\pi} H_{\lambda_f, \lambda_i}. \quad (3.1)$$

The helicity amplitudes are defined as $H_i(\theta) \equiv \langle \lambda_2 | J_{1\lambda_\gamma} | \lambda_1 \rangle$ [60, 59];

Table 3.2: Helicity Amplitudes $H_i(\theta)$. $\lambda_i = \lambda_\gamma - \lambda_{p_{target}}$, and $\lambda_{p_{recoil}}$.

$\lambda_f \backslash \lambda_i$	$\lambda_\gamma = +1$		$\lambda_\gamma = -1$		$\lambda_{p_{recoil}} \backslash \lambda_{p_{target}}$	$\lambda_\gamma = +1$		$\lambda_\gamma = -1$	
	$\frac{3}{2}$	$\frac{1}{2}$	$-\frac{1}{2}$	$-\frac{3}{2}$		1	$-\frac{1}{2}$	$+\frac{1}{2}$	$-\frac{1}{2}$
$\frac{1}{2}$	H_3	H_4	$-H_2$	H_1	$-\frac{1}{2}$	H_3	H_4	$-H_2$	H_1
$-\frac{1}{2}$	H_1	H_2	H_4	$-H_3$	$+\frac{1}{2}$	H_1	H_2	H_4	$-H_3$

$$\begin{aligned}
H_1(\theta) &\equiv \langle +\frac{1}{2} | J_{11} | -\frac{1}{2} \rangle = +\langle -\frac{1}{2} | J_{1-1} | +\frac{1}{2} \rangle, \\
H_2(\theta) &\equiv \langle +\frac{1}{2} | J_{11} | +\frac{1}{2} \rangle = -\langle -\frac{1}{2} | J_{1-1} | -\frac{1}{2} \rangle, \\
H_3(\theta) &\equiv \langle -\frac{1}{2} | J_{11} | -\frac{1}{2} \rangle = -\langle +\frac{1}{2} | J_{1-1} | +\frac{1}{2} \rangle, \\
H_4(\theta) &\equiv \langle -\frac{1}{2} | J_{11} | +\frac{1}{2} \rangle = +\langle +\frac{1}{2} | J_{1-1} | -\frac{1}{2} \rangle,
\end{aligned} \tag{3.2}$$

where $J_{1\lambda\gamma}$ is defined as

$$J_{1\lambda\gamma} = \mp \frac{J_x \pm iJ_y}{\sqrt{2}}. \tag{3.3}$$

The helicity amplitudes are related to the CGLN (Chew-Goldberger-Low-Nambu) amplitudes with $\phi = 0$:

$$\begin{aligned}
H_1(\theta) &\equiv \frac{i}{\sqrt{2}} \sin \theta \sin \frac{\theta}{2} [\mathcal{F}_3 - \mathcal{F}_4], \\
H_2(\theta) &\equiv -i\sqrt{2} \sin \frac{\theta}{2} \left[\mathcal{F}_1 + \mathcal{F}_2 + (\mathcal{F}_4 + \mathcal{F}_3) \cos^2 \frac{\theta}{2} \right], \\
H_3(\theta) &\equiv \frac{i}{\sqrt{2}} \sin \theta \cos \frac{\theta}{2} [\mathcal{F}_3 + \mathcal{F}_4], \\
H_4(\theta) &\equiv -i\sqrt{2} \cos \frac{\theta}{2} \left[\mathcal{F}_1 - \mathcal{F}_2 + (\mathcal{F}_4 - \mathcal{F}_3) \sin^2 \frac{\theta}{2} \right].
\end{aligned} \tag{3.4}$$

The cross section of the unpolarized beam and unpolarized target is

$$\frac{d\sigma}{d\Omega}(\theta) \equiv \sigma_0(\theta) = \rho_0 \mathcal{I}(\theta) = \frac{1}{2} \frac{q}{k} \sum_{i=1}^4 |H_i|^2, \tag{3.5}$$

where the factor $\rho_0 = q/k$ is the ratio of the final to initial state momenta, and \mathcal{I} is the differential cross section intensity.

The fifteen spin observables (see Section 3.3) in terms of CGLN amplitudes are given in Appendix A.

3.2 CGLN amplitudes

For spin-dependent observables of the π photoproduction, $\gamma N \rightarrow \pi N$, the T matrix is defined in terms of a current operator \mathbf{J} and photon polarization

vector $\hat{\epsilon}_\lambda(\vec{k})$ [60]:

$$\begin{aligned}\langle \mathbf{q} m_{s'} | T | \mathbf{k} m_s \lambda_\gamma \rangle &= \langle m_{s'} | \mathcal{F}_{\lambda_\gamma} | m_s \rangle \\ &= \langle m_{s'} | \mathbf{J} | m_s \rangle \cdot \boldsymbol{\epsilon}_\lambda(\mathbf{k}),\end{aligned}\tag{3.6}$$

where $\langle m_{s'} | \mathcal{F}_{\lambda_\gamma} | m_s \rangle$ is the scattering amplitude.

The scattering amplitude is constructed from a rank one spherical tensor operator

$$\mathcal{F}_{\lambda_\gamma} \equiv \mathbf{J} \cdot \boldsymbol{\epsilon}_\lambda(\mathbf{k}) = J_{1\lambda_\gamma}\tag{3.7}$$

in the Pauli-spinor space of the initial and final nucleon with spin projections m_s and $m_{s'}$. The current \mathbf{J} and $\mathcal{F}_{\lambda_\gamma}$ can be expressed by CGLN amplitudes [60]

$$\begin{aligned}\mathbf{J} &= i\boldsymbol{\sigma}\mathcal{F}_1 + \frac{(\boldsymbol{\sigma} \cdot \mathbf{q})(\boldsymbol{\sigma} \times \hat{\mathbf{k}})}{qk}\mathcal{F}_2 + i\frac{\boldsymbol{\sigma} \cdot \mathbf{k}}{qk}\mathbf{q}\mathcal{F}_3 + i\frac{\boldsymbol{\sigma} \cdot \mathbf{q}}{q^2}\mathbf{q}\mathcal{F}_4, \\ \mathcal{F}_\lambda &= \mathbf{J} \cdot \boldsymbol{\epsilon}_{\lambda_\gamma} \\ &= i\boldsymbol{\sigma} \cdot \hat{\boldsymbol{\epsilon}}_{\lambda_\gamma}\mathcal{F}_1 + (\boldsymbol{\sigma} \cdot \hat{\mathbf{q}})\boldsymbol{\sigma} \cdot (\hat{\mathbf{k}} \times \hat{\boldsymbol{\epsilon}}_{\lambda_\gamma})\mathcal{F}_2 + i(\boldsymbol{\sigma} \cdot \hat{\mathbf{k}})(\hat{\mathbf{q}} \cdot \hat{\boldsymbol{\epsilon}})\mathcal{F}_3 + i(\boldsymbol{\sigma} \cdot \hat{\mathbf{q}})(\hat{\mathbf{q}} \cdot \hat{\boldsymbol{\epsilon}})\mathcal{F}_4.\end{aligned}\tag{3.8}$$

The CGLN amplitudes \mathcal{F}_i are functions of energy and scattering angle, and are subject to unitarity and analyticity.

As mentioned before, with two photon polarization states, $\lambda_\gamma = \pm 1$, two initial target spin states, and two final recoil spin states, we have eight matrix elements of T , however, only four of these amplitudes are independent by virtue of rotational invariance and parity requirements. As a result, only four complex amplitudes, or equivalently at least eight real numbers are needed to specify the total amplitudes at each angle and energy. Therefore, only eight out of the sixteen polarization observables (Section 3.3) are independent at each angle and energy.

3.2.1 CGLN amplitudes and multipoles

For the analysis of the experimental data and also in order to study individual baryon resonances, pion photoproduction amplitudes are usually expressed in terms of two types of multipoles, electric ($E_{l\pm}$), and magnetic ($M_{l\pm}$) with pion angular momentum l and total angular momentum $j = l \pm \frac{1}{2}$ [57, 58].

Multipoles incorporate the orbital angular momentum of the final state, which are small near the threshold, and thus provide a natural truncation to just a few amplitudes.

The CGLN amplitudes \mathcal{F}_i can be expanded in terms of eigenstates of the total angular momentum, $j = l \pm \frac{1}{2}$ and parity $-(-1)^l$ in a multipole decomposition:

$$\begin{aligned}
\mathcal{F}_1 &= \sum_{l=0}^{\infty} [lM_{l+} + E_{l+}] P'_{l+1}(x) + [(l+1)M_{l-} + E_{l-}] P'_{l-1}(x), \\
\mathcal{F}_2 &= \sum_{l=1}^{\infty} [(l+1)M_{l+} + lM_{l-}] P'_l(x), \\
\mathcal{F}_3 &= \sum_{l=1}^{\infty} [E_{l+} - M_{l+}] P''_{l+1}(x) + [E_{l-} + M_{l-}] P''_{l-1}(x), \\
\mathcal{F}_4 &= \sum_{l=1}^{\infty} [M_{l+} - E_{l+} - M_{l-} - E_{l-}] P''_l(x).
\end{aligned} \tag{3.9}$$

Above equation can be inverted to electro- and magnetic-multipoles:

$$\begin{aligned}
M_{l\pm} &= \frac{1}{2} \begin{pmatrix} \frac{1}{l+1} \\ -\frac{1}{l} \end{pmatrix} \int_{-1}^{+1} dx \left[\mathcal{F}_1 P_l(x) - \mathcal{F}_2 P_{l\pm 1}(x) - \mathcal{F}_3 \frac{P_{l-1}(x) - P_{l+1}(x)}{2l+1} \right], \\
E_{l\pm} &= \frac{1}{2} \begin{pmatrix} \frac{1}{l+1} \\ \frac{1}{l} \end{pmatrix} \int_{-1}^{+1} dx \left[\mathcal{F}_1 P_l(x) - \mathcal{F}_2 P_{l\pm 1}(x) + \begin{pmatrix} l \\ -(l+1) \end{pmatrix} \mathcal{F}_3 \frac{P_{l-1}(x) - P_{l+1}(x)}{2l+1} \right. \\
&\quad \left. + \begin{pmatrix} l+1 \\ 2l+3 \end{pmatrix} \mathcal{F}_4 (P_l(x) - P_{l\pm 2}(x)) \right].
\end{aligned} \tag{3.10}$$

The energy-dependent amplitudes $M_{l\pm}$ and $E_{l\pm}$ refer to transitions initiated by magnetic and electric radiation, respectively. They lead to final states of orbital angular momentum l and total angular momentum $j = l \pm \frac{1}{2}$. These multipole amplitudes are labeled by the following good quantum numbers:

- (1) The final state orbital angular momentum l ,
- (2) the total state angular momentum, $j = l \pm \frac{1}{2}$,
- (3) the parity $(-1)^{l+1}$,
- (4) the angular momentum of the photon:

$$\begin{cases} j_\gamma = l_\gamma & \text{for magnetic photons} \\ j_\gamma = l_\gamma \pm 1 & \text{for electric photons.} \end{cases} \tag{3.11}$$

3.3 Spin observables

To determine the four helicity amplitudes (or transversity amplitudes) without ambiguities for pseudoscalar meson photoproduction, eight carefully selected measurements are necessary[59].

The spin observables are categorized as: three single-spin observables Σ , T , and P ; twelve double-spin observables G , H , E , F , O_x , O_z , C_x , C_z , T_x , T_z , L_x , and L_z . The differential cross section (unpolarized) is denoted as $\sigma(\theta)$. There are three different types of double polarized experiments for 12 double-spin observables: beam-target (BT), beam-recoil (BR), and target-recoil (TR) spin observables (Table 3.3).

$\sigma(\theta)$ and the three single-spin observable measurements determine the magnitudes of the four transversity amplitudes unambiguously. Three double-spin observables can in general, determine the relative phases between the four helicity amplitudes, and one double-spin observable eliminates discrete ambiguities. Transversity helicity amplitudes provide the advantage of having

Table 3.3: Observables in the Double polarization beam-target (BT), beam-recoil (BR), and target-recoil (TR).

photon (pol.)	beam	Target			Recoil			Target + Recoil			
	-	-	-	-	x'	y'	z'	x'	x'	z'	z'
	-	x	y	z	-	-	-	x	z	x	z
unpol.	σ_0		T			P		$T_{x'}$	$L_{x'}$	$T_{z'}$	$L_{z'}$
linear	$-\Sigma$	H	$(-P)$	$-G$	$O_{x'}$	$(-T)$	$O_{z'}$	$(L_{z'})$	$(T_{z'})$	$(-L_{x'})$	$(-T_{x'})$
circular		F		$-E$	$(-C_{x'})$		$(-C_{z'})$				

all single-spin observables ($\sigma(\theta), \Sigma, T, P$) expressed in terms of the amplitude magnitudes only (Table 3.4). The transversity amplitudes b_1, b_2, b_3 , and b_4 are expressed in terms of the helicity amplitudes H_1, H_2, H_3 , and H_4 :

$$b_i = U_{ij}^{(4)} H_j$$

$$U^{(4)} = \frac{1}{2} \begin{pmatrix} 1 & -i & i & 1 \\ 1 & i & -i & 1 \\ 1 & i & i & -1 \\ 1 & -i & -i & -1 \end{pmatrix}. \quad (3.12)$$

Table 3.4: Spin observables: The 16 spin observables are expressed in helicity and transversity representations. They are classified into four type sets [59]: type \mathcal{S} for the differential cross section and single-spin observables, and types \mathcal{BT} , \mathcal{BR} , and \mathcal{TR} for beam-target, beam-recoil, and target-recoil spin observables, respectively. $\mathcal{I}(\theta) = \frac{k}{q}\sigma_0(\theta)$ [59].

Spin observable	Helicity representation	Transversity representation	Set
$\mathcal{I}(\theta)$	$\frac{1}{2}(H_1^2 + H_2^2 + H_3^2 + H_4^2)$	$\frac{1}{2}(b_1^2 + b_2^2 + b_3^2 + b_4^2)$	\mathcal{S}
$\Sigma\mathcal{I}$	$Re(-H_1H_4^* + H_2H_3^*)$	$\frac{1}{2}(b_1^2 + b_2^2 - b_3^2 - b_4^2)$	
$-T\mathcal{I}$	$Im(H_1H_2^* + H_3H_4^*)$	$\frac{1}{2}(- b_1^2 + b_2^2 + b_3^2 - b_4^2)$	
$P\mathcal{I}$	$Im(-H_1H_3^* - H_2H_4^*)$	$\frac{1}{2}(- b_1^2 + b_2^2 - b_3^2 + b_4^2)$	
$G\mathcal{I}$	$Im(H_1H_4^* - H_3H_2^*)$	$Im(-b_1b_3^* - b_2b_4^*)$	\mathcal{BT}
$H\mathcal{I}$	$Im(-H_2H_4^* + H_1H_3^*)$	$Re(b_1b_3^* - b_2b_4^*)$	
$E\mathcal{I}$	$\frac{1}{2}(H_1^2 - H_2^2 + H_3^2 - H_4^2)$	$Re(b_1b_3^* + b_2b_4^*)$	
$F\mathcal{I}$	$Re(-H_2H_1^* - H_4H_3^*)$	$Im(b_1b_3^* - b_2b_4^*)$	
$O_x\mathcal{I}$	$Im(-H_2H_1^* + H_4H_3^*)$	$Re(-b_1b_4^* + b_2b_3^*)$	\mathcal{BR}
$-O_z\mathcal{I}$	$Im(H_1H_4^* - H_2H_3^*)$	$Im(-b_1b_4^* - b_2b_3^*)$	
$-C_x\mathcal{I}$	$Re(H_2H_4^* + H_1H_3^*)$	$Im(b_1b_4^* - b_2b_3^*)$	
$-C_z\mathcal{I}$	$\frac{1}{2}(H_1^2 + H_2^2 - H_3^2 - H_4^2)$	$Re(b_1b_4^* + b_2b_3^*)$	
$-T_x\mathcal{I}$	$Re(-H_1H_4^* - H_2H_3^*)$	$Re(-b_1b_2^* + b_3b_4^*)$	\mathcal{TR}
$-T_z\mathcal{I}$	$Re(-H_1H_2^* + H_4H_3^*)$	$Im(b_1b_2^* - b_3b_4^*)$	
$L_x\mathcal{I}$	$Re(H_2H_4^* - H_1H_3^*)$	$Im(-b_1b_2^* - b_3b_4^*)$	
$L_z\mathcal{I}$	$\frac{1}{2}(- H_1^2 + H_2^2 + H_3^2 - H_4^2)$	$Re(-b_1b_2^* - b_3b_4^*)$	

In the following equations, the relation between the differential cross section and the spin observables are given for the three types of double-polarization experiments:

(a) Polarized beam and polarized target [61, 62]:

$$\begin{aligned} \frac{d\sigma}{d\Omega} = & \sigma_0[1 - P_T\Sigma \cos(2\phi) - P_x(P_T H \sin(2\phi) - P_\odot F) \\ & + P_y(T - P_T P \cos(2\phi)) + P_z(P_T G \sin(2\phi) - P_\odot E)]. \end{aligned} \quad (3.13)$$

The polarization observables are related by the following equations:

$$\begin{aligned} E^2 + F^2 + G^2 + H^2 &= 1 + P^2 - \Sigma^2 - T^2 \\ FG - EH &= P - T\Sigma. \end{aligned} \quad (3.14)$$

(b) Polarized beam and recoil target [61]:

$$\begin{aligned} \rho_f \frac{d\sigma}{d\Omega} = \sigma_0 [& 1 + \sigma_y P - P_T \cos(2\phi)(\Sigma + \sigma_y T) \\ & - P_T \sin(2\phi)(O_x \sigma_x + O_z \sigma_z) - P_\odot (C_x \sigma_x + C_z \sigma_z)]. \end{aligned} \quad (3.15)$$

(c) Polarized target and recoil target [61]:

$$\rho_f \frac{d\sigma}{d\Omega} = \sigma_0 [1 + \sigma_y P + P_x (T_x \sigma_x + T_z \sigma_z) + P_y (T + \Sigma \sigma_y) - P_z (L_x \sigma_x - L_z \sigma_z)], \quad (3.16)$$

where $\rho_f = \frac{1}{2}(\mathcal{I} + \sigma \cdot P_f)$, P_f , and \mathcal{I} are the density matrix of the recoil nucleon, its polarization, and the identity matrix, respectively.

3.4 Rules for observables

There are some general rules for the behavior of the fifteen single and double polarization observables [60]. Because the angle dependence of helicity amplitudes is stored in the Wigner d -functions, it is particularly helpful to work with them for this purpose. The Wigner d -functions have many simple and useful properties (Appendix C.2).

The multipole decomposition suggests a truncation of the number of amplitudes due to the centrifugal barrier near threshold. And it also provides other simple rules for the sixteen observables. The helicity amplitudes expanded into partial waves are

$$H_i(\theta) = \sum_j (2j+1) H_i^j d_{\lambda_f \lambda_i}^j(\theta), \quad (3.17)$$

where $d^J(\theta)$ is the Wigner d -function in the case of $\phi = 0$. The four helicity amplitudes become [60]:

$$\begin{aligned} H_1(\theta) &= \sum_j (2j+1) H_1^j d_{-\frac{1}{2} \frac{3}{2}}^j(\theta), \\ H_2(\theta) &= \sum_j (2j+1) H_2^j d_{-\frac{1}{2} \frac{1}{2}}^j(\theta), \\ H_3(\theta) &= \sum_j (2j+1) H_3^j d_{\frac{1}{2} \frac{3}{2}}^j(\theta), \\ H_4(\theta) &= \sum_j (2j+1) H_4^j d_{\frac{1}{2} \frac{1}{2}}^j(\theta). \end{aligned} \quad (3.18)$$

H_4 is a no helicity flip amplitude ($\lambda_i - \lambda_f = 0$), H_2 and H_3 are single helicity flip amplitudes ($|\lambda_i - \lambda_f| = 1$), and H_1 is a double flip amplitude ($|\lambda_i - \lambda_f| = 2$), where the total helicity change $\lambda_f - \lambda_i$ is the total spin flip. From the properties $d_{\lambda\lambda'}^j(0^\circ) = \delta_{\lambda\lambda'}$ and $d_{\lambda\lambda'}^j(180^\circ) = (-1)^{j-\lambda'}\delta_{\lambda-\lambda'}$, it follows that amplitudes H_1 and H_3 vanish at both the 0° and 180° end points, whereas $H_2(0^\circ) = 0$ and $H_4(180^\circ) = 0$. These properties are also seen directly from Eq. (3.4).

The sixteen observables may be grouped into four classes by their dependence on the H_i (see Section 3.3).

$$\begin{aligned}
(1) \mathcal{I}, E, C_{z'}, L_{z'} &; \quad \sum_i \pm |H_i(\theta)|^2, \\
(2) P, H, C_{x'}, L_{x'} &; \quad \pm H_2(\theta)H_4(\theta)^* \pm H_1(\theta)H_3(\theta)^*, \\
(3) T, F, O_{x'}, T_{z'} &; \quad \pm H_1(\theta)H_2(\theta)^* \pm H_3(\theta)H_4(\theta)^*, \\
(4) \Sigma, G, O_{z'}, T_{x'} &; \quad \pm H_1(\theta)H_4(\theta)^* \pm H_2(\theta)H_3(\theta)^*.
\end{aligned} \tag{3.19}$$

The group (1), $\mathcal{I}, E, C_{z'}, L_{z'}$, take on simple forms in the forward direction

$$\begin{aligned}
\mathcal{I}(0) &= +\frac{1}{2}|H_4(0)|^2, \\
E(0) &= -\frac{1}{2}|H_4(0)|^2, \\
C_{z'}(0) &= +\frac{1}{2}|H_4(0)|^2, \\
L_{z'}(0) &= -\frac{1}{2}|H_4(0)|^2,
\end{aligned} \tag{3.20}$$

where for example $H_4(\theta = 0)$ is the no spin-flip helicity amplitudes at zero degrees, and in the backward direction

$$\begin{aligned}
\mathcal{I}(\pi) &= +\frac{1}{2}|H_2(\pi)|^2, \\
E(\pi) &= -\frac{1}{2}|H_2(\pi)|^2, \\
C_{z'}(\pi) &= -\frac{1}{2}|H_2(\pi)|^2, \\
L_{z'}(\pi) &= +\frac{1}{2}|H_2(\pi)|^2,
\end{aligned} \tag{3.21}$$

where for example $H_2(\theta = \pi)$ is one of the single spin-flip helicity amplitudes

at angle π . These general results lead to:

$$\begin{aligned}
E(0) &= E(\pi) = -1, \\
C_{z'}(0) &= -C_{z'}(\pi) = +1, \\
L_{z'}(0) &= -L_{z'}(\pi) = -1.
\end{aligned}
\tag{3.22}$$

As a result, E is nodeless or has an even number of sign-changing nodes, but $C_{z'}$ and $L_{z'}$ have odd number of sign-changing nodes.

In the group (1), there are the following relations between observables :

$$\begin{aligned}
1 + L_{z'} + E + C_{z'} &= 2|H_3|^2 \geq 0, \\
1 - L_{z'} - E + C_{z'} &= 2|H_4|^2 \geq 0, \\
1 + L_{z'} - E - C_{z'} &= 2|H_2|^2 \geq 0, \\
1 - L_{z'} + E - C_{z'} &= 2|H_1|^2 \geq 0.
\end{aligned}
\tag{3.23}$$

If $\sigma(0) > \sigma(\pi)$ (same as if the cross section has a forward peak), then it must be that $|\mathbf{H}_4(0)| > |\mathbf{H}_2(\pi)|$ ($|\mathbf{H}_1(0)| = |\mathbf{H}_2(0)| = |\mathbf{H}_3(0)| = |\mathbf{H}_1(\pi)| = |\mathbf{H}_3(\pi)| = |\mathbf{H}_4(\pi)|$). This peaking rule of the cross section becomes simply $Re |\mathcal{F}_1 \mathcal{F}_2^*| < 0$ using Eq. (3.4) (the result is $|\mathcal{F}_1 - \mathcal{F}_2| > |\mathcal{F}_1 + \mathcal{F}_2|$)¹. This forward peaking rule constrains the multipole amplitudes.

The observable of group (1) ($\mathcal{I}, E, C_{z'}, L_{z'}$) depend on the magnitude of the four helicity amplitudes, which have the following dependence on the combined Wigner d -functions:

$$\begin{aligned}
|H_1(\theta)|^2 &\sim \sum d_{-\frac{1}{2}\frac{3}{2}}^j(\theta) \\
|H_2(\theta)|^2 &\sim \sum d_{-\frac{1}{2}\frac{1}{2}}^j(\theta) \\
|H_3(\theta)|^2 &\sim \sum d_{\frac{1}{2}\frac{3}{2}}^j(\theta) \\
|H_4(\theta)|^2 &\sim \sum d_{\frac{1}{2}\frac{1}{2}}^j(\theta).
\end{aligned}
\tag{3.24}$$

3.5 FROST experiment

The FROST experiment is a double polarization experiment using a polarized photon beam and a polarized target. The polarization observables

¹ Let $\mathcal{F}_1 = f_1^R + i f_1^I, \mathcal{F}_2 = f_2^R + i f_2^I$. Since $|\mathcal{F}_1 - \mathcal{F}_2|^2 > |\mathcal{F}_1 + \mathcal{F}_2|^2$, $f_1^R f_2^R + f_1^I f_2^I < 0$. $Re |\mathcal{F}_1 \mathcal{F}_2^*| = f_1^R f_2^R + f_1^I f_2^I$, which is same to above.

obtained from this experiment can be written as bilinear equations of helicity amplitudes $H_1 \sim H_4$ (see Table 3.4). These helicity amplitudes can be rewritten by CGLN amplitudes $\mathcal{F}_1 \sim \mathcal{F}_4$ [Eq. (3.4)], or partial waves [Eq. (3.9)]. If the helicity amplitudes are determined without any ambiguity, resonances can be constructed through the partial waves. Thus, double polarization experiments are important for investigation of the nucleon.

The goal of the FROST (FRozen Spin Target) experiment is the measurement of a large sets of single and double polarization observables in associated light pseudo-scalar mesons (π, η, K), vector mesons (ρ, ω), and hyperons (Λ, Σ) in the two-body and three-body ($\pi^+\pi^-N$) final states[63, 64, 65, 66]. Some specific goals for the above mentioned channels are:

- For $\gamma p \rightarrow K^+\Lambda, K^+\Sigma^0$, and $K^0\Sigma^+$: Extract the transition amplitudes not only of established baryon resonances but also from resonant states which are not yet experimentally observed. Due to the weak decay of Λ and Σ^+ , the recoil polarization can be determined in coincidence with polarization states of beam and target [67].

- For ρ and ω production: Determine the tensor polarization of the vector mesons via analysis of the angular distribution of their decay particles.

- For $\gamma p \rightarrow \pi^+\pi^-N$: Better understanding of the $P_{11}(1440)$ resonance [68].

All analyses will contribute to a better understanding of baryon resonances. The extracted observables will be analyzed together with observables from other CLAS run groups. For single pion production these run groups are:

- CLAS-g1: (Observable σ_0) unpolarized beam and unpolarized target,
- CLAS-g8: (Observable Σ) linearly polarized beam and unpolarized target,
- CLAS-g9a: (Observable E and G) linearly and circularly polarized beam, and longitudinally polarized target,
- CLAS-g9b: (Observable H, F and P) linearly and circularly polarized beam, and tangentially polarized target.

The FROST experiment is those with polarized beam and polarized target. These above experiments have been performed using the Hall-B photon beam facility and the CLAS detector with a polarized frozen spin butanol target. The measurements cover almost the full angular range and a large energy range.

The measurement of the observables E and G was carried out during about 100 days between November 3rd, 2007 and February 12th, 2008. In total more than 10.5 billion events with at least one charged track were recorded. The detailed numbers of triggers by observable and by energy are shown in Table

3.5.

Table 3.5: The triggers for observables E and G .

Polarization of beam	Observable	$E_{electron}$ (GeV)	E_{γ} (GeV)	Production (Million)
Circularly	E	1.645	0.5	1100
		2.478	~ 2.4	2300
Linearly	G		0.7	300
			0.9	500
			1.1	500
			1.3	600
			1.5	600
			1.7	850
			1.9	720
			2.1	800
		2.3	780	
Total		10.5 billion triggers		

3.5.1 Linearly polarized electron beam

During the FROST experiment, linearly polarized electron beam was used to get circularly polarized photon beam. When an electron hits heavy atoms, it produces real photons. The determination of the electron beam polarization is performed via a Møller polarimeter. Table 3.6 shows the results of the Møller measurement of the electron beam. During the experiment, the average polarization of the primary electron beam was about 83.5 %, and the range of polarization was 79.8 % \sim 87.6 %. In case that several Møller measurements were performed within a short time interval (same corresponding run number), the averaged value is used as electron beam polarization until the next Møller measurements. The polarization values, which are used in the analysis during certain run ranges, are listed in the third column.

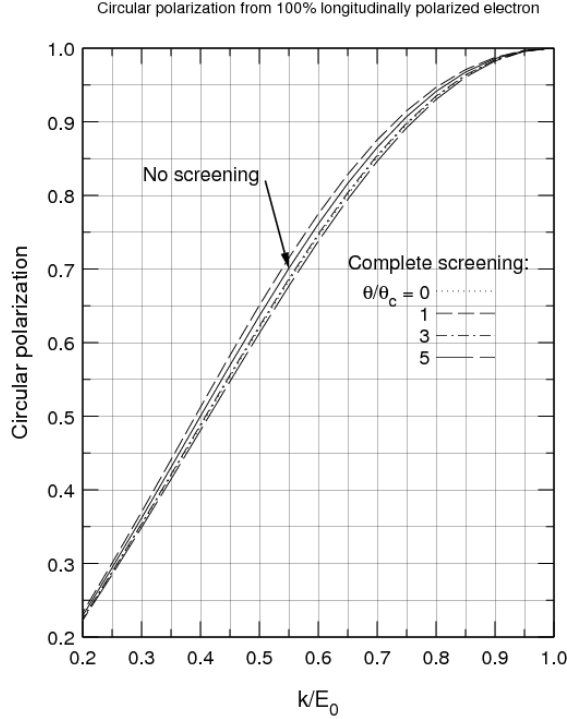
Table 3.6: Polarization of the electron beam obtained from Møller measurements during the experiment and averaged polarizations used for the analysis.

Energy of Electron beam	Run number	Møller Measurement(%)	Run range average pol.(%)
1.645 GeV	55544	- 85.228 \pm 1.420 + 78.523 \pm 1.350 + 79.150 \pm 1.26 - 88.700 \pm 1.480	55521 ~ 55551 82.90
	55552	- 84.167 \pm 1.330 + 84.725 \pm 1.530	55552 ~ 55587 84.45
	55588	+ 86.531 \pm 1.380 - 88.409 \pm 1.440 - 87.753 \pm 1.480	55588 ~ 55607 87.56
2.478 GeV	55608	+ 82.534 \pm 1.400	55608 ~ 55625 82.53
	55627	+ 79.450 \pm 1.410 - 80.060 \pm 1.400	55630 ~ 56193 79.76
	56194	+ 83.267 \pm 1.380	56196 ~ 56201 83.27
	56202	+ 83.248 \pm 1.320	56202 ~ 56233 83.25

3.5.2 Circularly polarized photon beam

If the electron beam is itself longitudinally polarized, the resulting bremsstrahlung photons possess circular polarization. The circularly polarized photon beam is generated when the electron beam goes through a thin radiator. The radiator was a gold plate on a thin carbon support foil.

The degree of polarization transfer to the photon in the bremsstrahlung process is almost 100 % when the photons carry off the maximum available energy, but decreases as the function of available energy given to the photon reduces. This transfer can be calculated and is illustrated in Figure 3.1, where it can be seen that for photon energies 50 % of the beam energy, the polarization transfer is around 60 % [69].



Corrected 5 June 1992

04-22-96
CERN/SL/96.11.T

Figure 3.1: The degree of circular polarization as a function of momentum energy transfer to the bremsstrahlung photon [69]. k and E_0 are the photon energy and the electron energy, respectively.

The polarization of the photon, P_{\odot} , is approximately given by

$$P_{\odot} = P_e \frac{4x - x^2}{4 - 4x + 3x^2}, \quad (3.25)$$

where $x = E_k/E_0$ is the ratio of photon energy (E_k) and electron energy (E_0), and P_e is the degree of longitudinal polarization of the incident electrons. The degree of polarization rises with x (see Figure 3.1). Because $P_{\odot}/P_e < 60\%$ for $x < 0.5$, it is desirable to trigger only on the high energy photons. We used the existing instrumented collimator ($r = 1\text{mm}$), which allows the photon beam position to be monitored. The collimation diminishes the photon flux on the target significantly: for $E_0 = 1.6\text{ GeV}$ to 32 % and $E_0 = 2.6\text{ GeV}$ to 47 % of the uncollimated flux [70]. The fraction of photons after collimation varies slightly with photon energy.

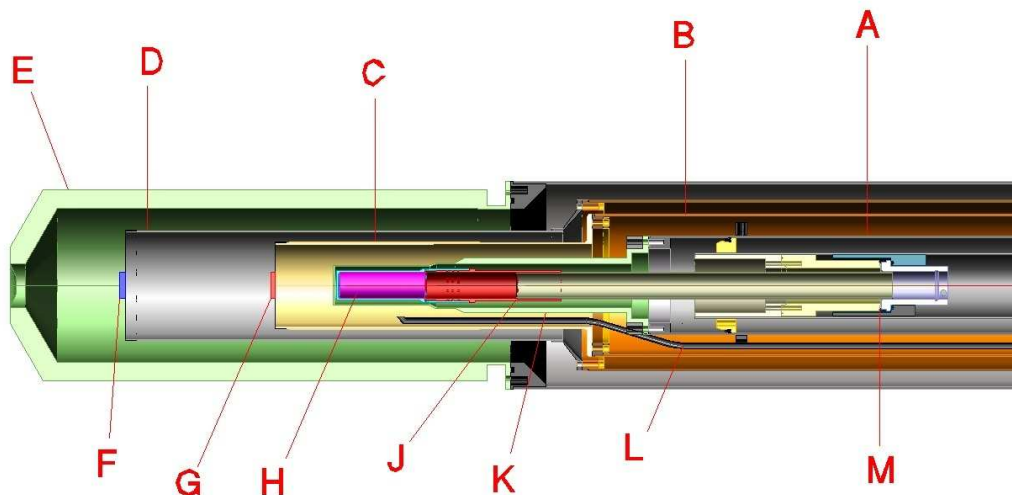


Figure 3.2: Side view of the FROST cryostat with beam entering from right. The letters correspond to: (A) Primary heat exchanger, (B) 1 k heat shield, (C) Holding coil, (D) 20 K heat shield, (E) Outer vacuum can, (F) Polyethylene target, (G) Carbon target, (H) Butanol target, (J) Target insert, (K) Mixing chamber, (L) Microwave waveguide, and (M) Kapton cold seal.

3.5.3 Longitudinally polarized target

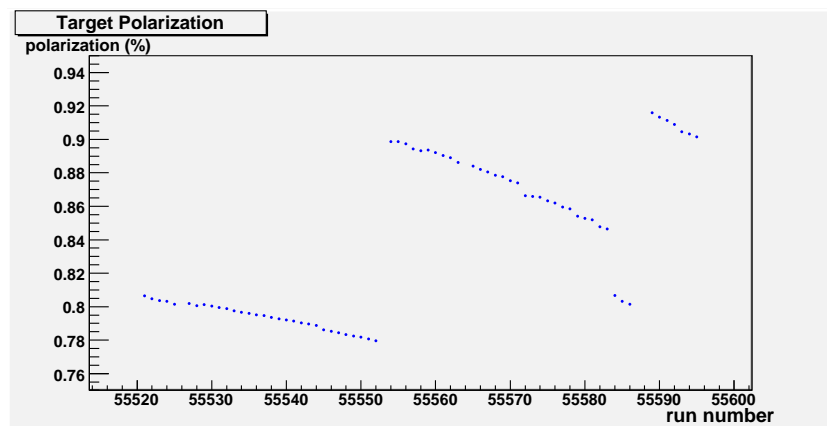
The target used in the experiment is made out of butanol C_4H_9OH beads surrounded by liquid helium. Figure 3.2 shows side view of the target including the polarizing magnet. Protons in frozen butanol are highly polarized via a technique called Dynamic Nuclear Polarization (DNP). The DNP technique results from transferring spin polarization from electrons to nuclei. Therefore, the nuclear spins align to the extent that electron spins are aligned. The alignment of electron spins at a given magnetic field and temperature is described by the Boltzmann distribution under thermal equilibrium. When electron spin polarization deviates from its thermal equilibrium value, polarization transfers between electron and nuclei can occur spontaneously.

The DNP process is performed at a “moderate” temperature of approximately 0.3 Kelvin inside a homogeneous magnetic field of 5.0 Tesla. Under

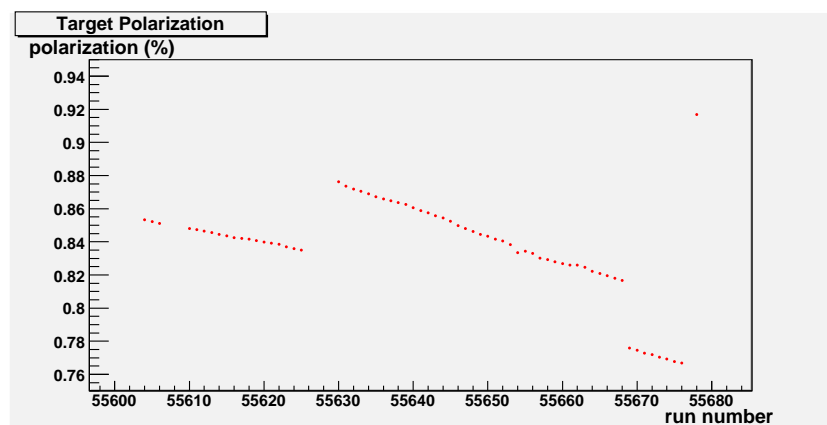
these conditions the electron spins of the paramagnetic radicals are completely polarized. Saturating the target with microwaves near the Electron Spin Resonance (ESR) frequency transfers the electrons' polarization to the nuclear spins. The nuclear spins can be polarized either parallel or anti-parallel to the direction of the magnetic field, depending on whether the microwave frequency is slightly below or above the ESR frequency. When the ultimate target polarization is reached, the microwave generator is switched off. Then, the refrigerator cools the target to a temperature of about 30 mK[71]. The polarization of the protons decays very slowly at such low temperatures, thus the name "frozen-spin target". Moreover, the relaxation time can be significantly improved by applying a week holding field of about 0.5 Tesla. Both the polarizing and holding magnets produce fields along the direction of the photon beam. Unlike the polarizing magnet, the superconducting solenoid for the holding field is thin enough for scattered particles to pass through and be detected by the CLAS spectrometer. However its magnetic field is strong enough to keep the polarization decay at an acceptably low rate (less than 1 % per day). The value of the relaxation time is a strong function of the ratio B/T where B is the value of the magnetic holding field and T the material temperature.

Both the polarizing and solenoid holding magnets produce a field along the direction of the photon beam. The target is in Frozen Spin Mode for a magnetic field of 5 Tesla polarizing magnet. After the target is removed from the polarizing magnet, it is moved into the center of CLAS with a holding field about 0.5 Tesla.

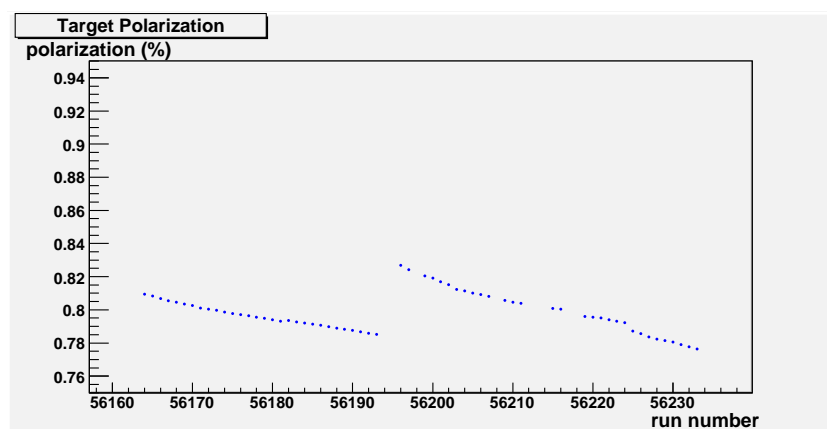
During the FROST experiment, the polarization of the frozen spin target, which was measured using the NMR technique [72], was between 78 % and 92 % with a relaxation time of more than 2,000 hours. Figure 3.3 shows the degree of polarization as a function of the run number. The ranges of target polarization are 78% \sim 92% for $E_\gamma = 1.645$ GeV, and 78 % \sim 88% for $E_\gamma = 2.478$ GeV. Since the target polarization reduced constantly until the target is repolarized during the experiment, a run-by-tun target polarization is used in my analysis.



(a) The run period from 55521 to 55595.



(b) The run period from 55604 to 55678.



(c) The run period from 56164 to 56233.

Figure 3.3: The trend of the polarization of the butanol target during the experiment.

Chapter 4

Experimental Facility

The FROST experiment presented in this thesis was carried out at the Thomas Jefferson National Accelerator Facility (JLab) in Newport News, Virginia, USA. JLab is dedicated to the study of hadronic and nuclear physics. It stages experiments on a variety of targets using both electron- and photon-beams at energies up to 6 GeV. An upgrade of the facility to 12 GeV is expected to be completed in 2012. This chapter focuses on the facility and experimental techniques employed, specifically the production, a description of detectors used to identify the outlying products of the reactions and an outline of the data acquisition process.

4.1 The facility

The continuous electron beam accelerator facility (CEBAF) [73] as shown in Figure 4.1 at JLab is devoted to investigating the electromagnetic structure of mesons, nucleons, and nuclei. CEBAF is a racetrack-electron accelerator consisting of two superconducting radio-frequency linear accelerators. They are connected at each end with recirculation arcs along which the electron beam is directed by fixed steering magnets. The accelerator operates at 100 % duty cycle, delivering a bunched beam of picosecond-wide pulses¹. The electron beam can be circulated around the underground racetrack up to five times. The beam energy of CEBAF can be varied up to 6 GeV and will be upgraded to 12 GeV to expand the nuclear-physics opportunities. The beam is delivered to three experimental halls - A, B, and C for simultaneous electron- and photon-scattering experiments.

¹The beam is termed “continuous” due to its short and frequent pulses since the typical pulse duration of a “pulsed” accelerator is in the order of nanoseconds.

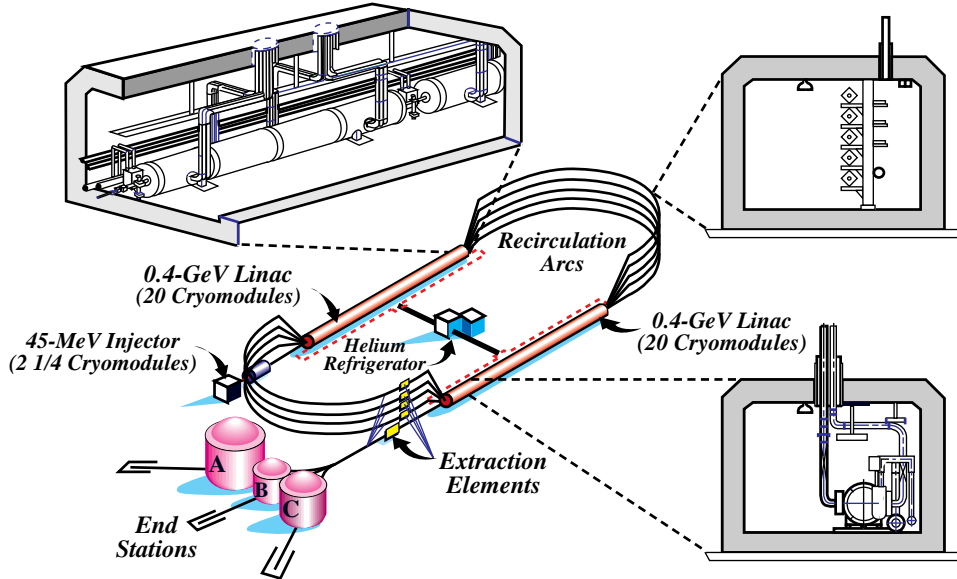


Figure 4.1: Schematic layout of the CEBAF accelerator [74].

Halls A and C operate at high electron-beam luminosities up to $10^{38} \text{ cm}^{-2} \text{ s}^{-1}$ at the target. They are designed for high precision electron scattering experiments. The scattered electron and reaction products are detected in high-resolution magnetic spectrometers. Hall A has two high-resolution magnetic spectrometers to be able to reconstruct the mass of the unobserved hadronic final state precisely [75]. Hall C has two focusing magnetic spectrometers: one offers a larger acceptance for high momentum particles and another has good detection of short-lived particles [76]. Hall B, with the CEBAF Large Acceptance Spectrometer (CLAS), will be discussed in detail in this chapter.

4.2 CLAS

The design of the CEBAF Large Acceptance Spectrometer (CLAS), which has complex structure of layered detectors as seen in Figure 4.2, is based on a toroidal magnetic field. The toroidal magnetic field is produced by six superconducting coils located radially around the beam-line of CLAS. CLAS covers large angles of charged particles, and provides particle identification and momentum determination. The momentum measurement of charged particles is provided by tracking them through three drift chambers, one located inside the

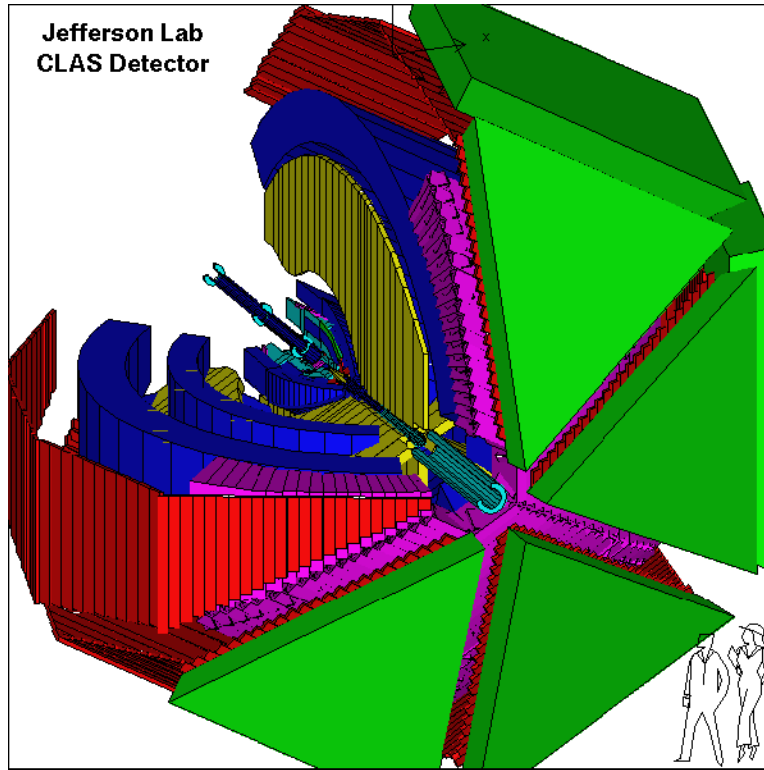


Figure 4.2: CLAS: Showing symmetrically arranged around the beam axis; the superconducting coils (yellow), three regions of drift chambers (blue), the Čerenkov counters (pink), the shell of time-of-flight scintillation counters (red), and the electromagnetic calorimeters covering the forward angles (green) [73].

area of the torus field and the others inside and outside the torus field. The start counter provides information for the timing of particles and for event triggering. A shell of scintillation counters outside the drift chambers allows for a time-of-flight measurement. The Čerenkov counters are used to distinguish between pions and electrons and as electron trigger. Two sets of electromagnetic calorimeters, the forward and large-angle calorimeter, which are located outside of the time-of-flight counters, provide energy measurements and neutral particle identification. The field-free region in the center of CLAS allows for the use of polarized targets, including dynamically polarized target with fields up to 5.0 T. The ranges of coverage and resolutions are listed in Table 4.1.

Table 4.1: Summary of the CLAS detector characteristics [73]

Capability	Quantity	Range
Coverage	Charged-particle angle	$8^\circ \leq \theta \leq 140^\circ$
	Charged-particle momentum	$p \geq 0.2 \text{ GeV}/c$
	Photon angle (4 sectors)	$8^\circ \leq \theta \leq 45^\circ$
	Photon angle (2 sectors)	$8^\circ \leq \theta \leq 75^\circ$
	Photon energy	$E_\gamma \geq 0.1 \text{ GeV}$
Resolution	Momentum ($\theta \lesssim 30^\circ$)	$\sigma_p/p \approx 0.5 \%$
	Momentum ($\theta \gtrsim 30^\circ$)	$\sigma_p/p \approx (1 - 2) \%$
	Polar angle	$\sigma_\theta \approx 1 \text{ mrad}$
	Azimuthal angle	$\sigma_\phi \approx 4 \text{ mrad}$
	Time (charged particles)	$\sigma_t \approx (100 - 250) \text{ ps}$
	Photon energy	$\sigma_E/E \approx 10 \% / \sqrt{E}$

4.2.1 Torus magnet

The CLAS magnetic field, which bends the direction of charged particles, is generated by six superconducting coils. These coils are positioned toroidally around the beam line. The size of the kidney-shaped coils is about 1m in diameter and 5 m in length. The magnitude of the magnetic field is calculated directly from the current in the coils. The magnet produces its main field in azimuthal direction. The coil shape is optimized to reduce deflections in azimuthal directions even for tracks close to the coils.

The highest momentum particles from a fixed target are generally emitted at forward angles. To provide optimum curvature in the tracks of charged particles, the coils are designed to have a high magnetic field at forward angles and a lower field at large angles, where particle momenta are typically smaller. At the maximum current, the field reaches 2.5 T·m in the very forward direction and it drops to 0.6 T·m perpendicular to the beam-line [73]. The center of CLAS remains close to field-free allowing the use of a polarized target and causing negligible deflections to a charged beam. Because of the CLAS toroidal magnet, charged particles are bent toward or away from the axis of the beam. However, their azimuthal angles are unchanged.

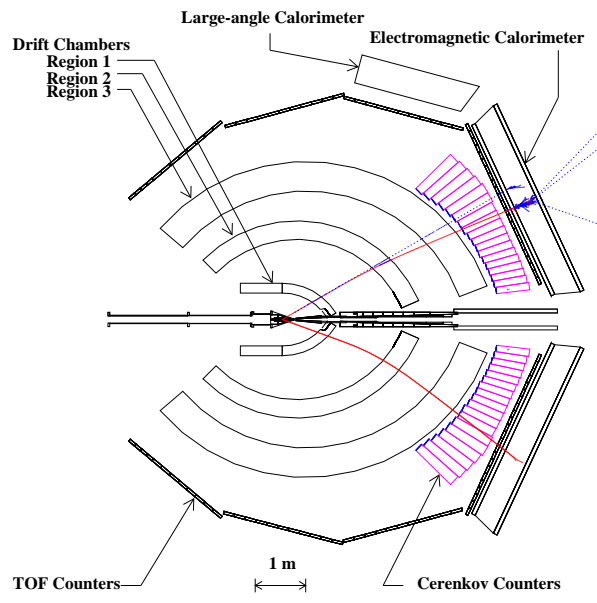
4.2.2 Drift chambers

The drift chambers are located at three radial positions, “Region One” (R1), “Region Two” (R2), and “Region Three” (R3) [77], in each of the six independent tracking areas (sectors). The trajectories with a momentum higher than 100 MeV/c are mapped through these eighteen separate drift chambers. Each region consists of six drift chambers positioned at the same radius in the six sectors of CLAS. R1 is in an area of the low magnetic field just outside the start counter. R2 is situated in the area of highest magnetic field between the magnetic coils. R3 is located outside the torus field. Figure 4.3 shows the locations of R1, R2, and R3 in different cross sections. The wires are stretched between two end-plates, and their direction is almost perpendicular to the bend plane. Thus, it provides maximum sensitivity to the track curvature. The entire drift chamber system covers from 8° to 142° in the polar angle and 80 % of the azimuthal angle.

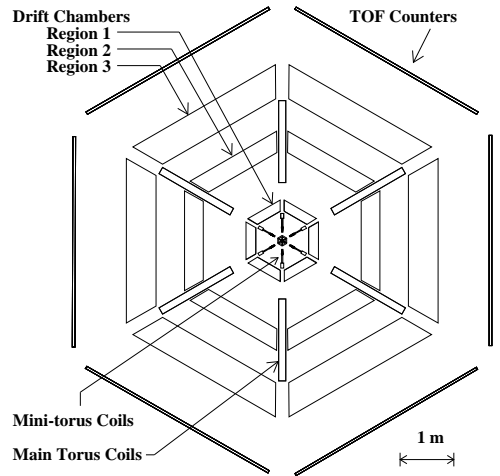
The wire layers in each chamber are grouped into two superlayers of six wire layers as shown in Figure 4.4 and each is for pattern recognition and tracking redundancy. The wires in one superlayer are strung axially to the magnetic field, and the wires in the other superlayer are tilted at a 6° stereo angle to provide azimuthal information. The innermost superlayer is an exception since it consists of only four wire layers due to space limitations. The cell size of a wire chamber increases uniformly with radial distance from the target. A high-voltage system keeps the sense wires at a positive potential and the field wires at a negative potential.

Electrical signals from each sense wire are output to a differential pre-amplifier board attached to each chamber endplate. The resulting digital output pulses are multiplexed and passed to common-stop time-to-digital converters (TDCs). The output signals are recorded by a Data Acquisition (DAQ) system if they fall within a preset time window of $1.6 \mu\text{s}$ from the trigger. The timing signals are subsequently used in calculations of drift time and velocity. They also improve accuracy in the determination of the particle track.

The tracking accuracy is determined by the deviation of the reconstructed momenta and angles of the charged particle comparing to those from their true values at the interaction vertex. Tracking uncertainties arise from the interaction of a several causes, like statistical variations of the ionization processes caused by a traversing particle, multiple scattering in the material along



(a) perpendicular to the beam axis



(b) parallel to the beam axis

Figure 4.3: Drift Chamber: They show the cross sections through CLAS perpendicular to the beam axis (top) and parallel to it (bottom) [78].

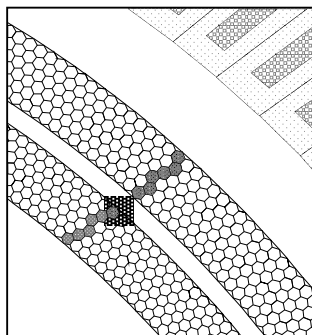


Figure 4.4: A section through Region 3 of the drift chamber: It shows the two superlayers and the hexagonal array of cells formed by the arrangement of field wires. A possible particle track through the regions is shown as shaded cells where a hit is registered in the sense wire at the center of each cell [78].

the particle trajectory, geometrical misalignment of the drift chambers, lack of knowledge of the exact value of the traversed magnetic field, background hits in the chambers, and the resolution of the single drift cells, which depends on the position where the track passed through the cell.

The performance of the drift chambers can be characterized in two ways, by how efficiently the chamber registers tracks and how accurately the tracks are determined. Wire-hit efficiencies are greater than 98 %. The tracking efficiency is greater than 95 % for low hit occupancies. Typical accidental occupancies are well below 5 % at full design luminosity. And it is significantly lower for photon beam experiments. Track resolution varies from region to region.

Statistical variations of the ionization processes inside the drift cells, uncertainties in the magnetic field, and mechanical misalignment of the system

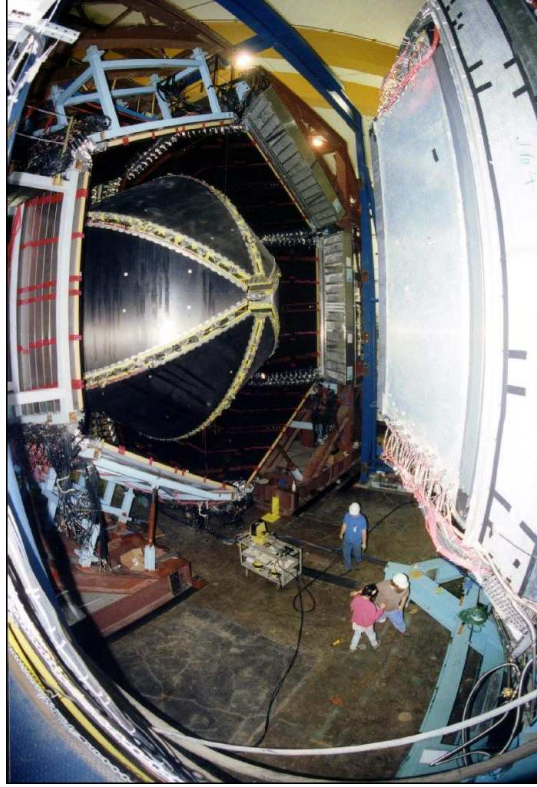


Figure 4.5: Photograph of CLAS opened up, showing the sphere formed by the six sectors of the drift chambers.

result in track resolution range from 300 to 450 μm from R1 to R3. This results in a momentum uncertainty of better than 0.5 % for GeV/c particles and an angular resolution of better than 2 mrad for reconstructed tracks.

Figure 4.5 is a photograph of CLAS showing R3 of the drift chambers.

4.2.3 Trigger

A two-level hierarchical trigger system [79], the Level 1 trigger and the Level 2 trigger, acquires events of interest minimizing the dead-time. The Level 1 trigger is dead-timeless. It processes all prompt photomultiplier tubes (PMTs) signals within 90 ns through a pipe-lined memory. The resultant signals are sent to a trigger supervisor (TS) module. The TS generates reference or stop signals for the TDCs and gate signals for the analogue-to-digital converters (ADCs).

The TS, which is the electronic control center, takes the Level 1 and Level 2 inputs from the trigger system. It produces all common signals, busy gates, and resets required by the detector electronics. It will hold digitization until a pass or a fail signal is received from the Level 2 trigger if it is configured to run with the two level trigger system. The event information is then digitized.

The Level 1 trigger [80, 81] uses any or all available prompt information such as the general location of hits in the time-of-flight (TOF) detector, the signals in the Čerenkov detector for electron identification, and the energy deposited in the calorimeter if a desired event has occurred. This trigger has a three stage process. The first two stages combine prompt hits from different detectors and compare the emerging hit patterns to those stored in look-up tables in the memory. These memory tables are configured for every experiment. They list possible hits associated with chosen particles. The third stage correlates patterns the individual sectors to identify likely events. For example, a likely event of a proton might be a positive track in one sector accompanied by a negative one diametrically opposite. Additional information is included at this stage and the signals are passed to the TS. The Level 2 [82, 83] trigger performs a correction to the Level 1 trigger and generates a fail signal if no correlated hit segments in the drift chambers are found. Due to the slow response of the drift chambers, the processing time takes more than $2 \mu s$ and contributes directly to the dead time of the system.

During the FROST experiment the trigger was configured to require a start counter hit and time-of-flight hit in the same sector (Level 1) as well as correlated hit segments in the same sector (Level 2).

4.2.4 Start counter

In order to determine the particle type of scattered particles, it is necessary to measure the flight time of particles through a known distance. The time of particles at the end of the trajectory in CLAS is measured by the TOF scintillators. The start counter as shown in Figure 4.6 measures a time close to the interaction time in the target since it is the innermost detector in CLAS. The start counter is also used as part of the trigger. 4.6. Since it is the first detector a produced particle encounters on its path into CLAS [84]. The timing information is used for data acquisition and event reconstruction.

The acceptance of the start counter is $7^\circ < \theta < 145^\circ$ and $-29^\circ < \phi < 29^\circ$

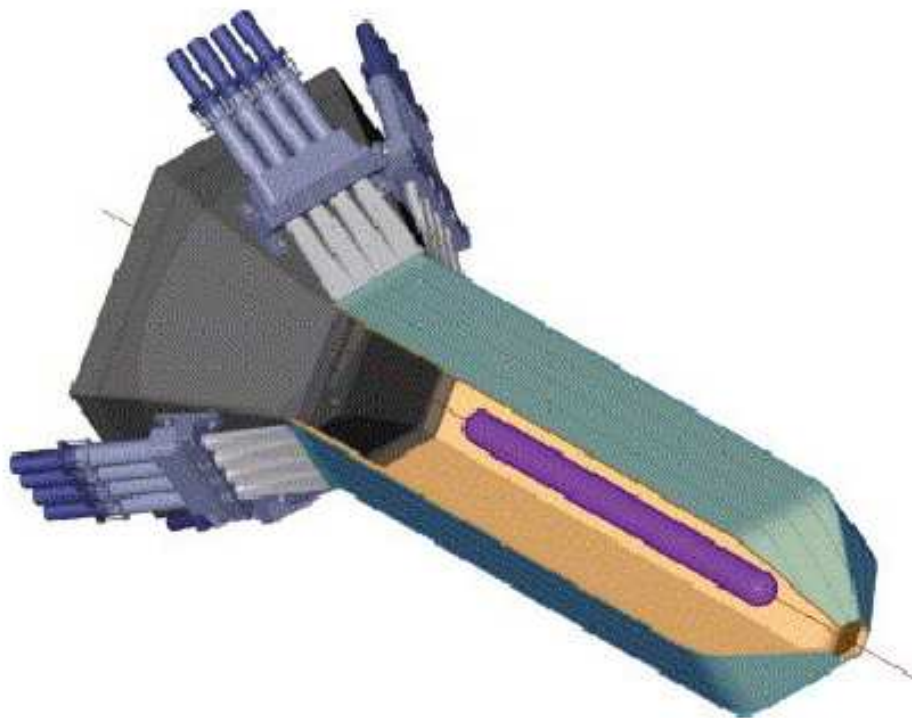


Figure 4.6: The figure shows the start counter.

subtending the same solid angle as the TOF counters for an extended cylindrical target. Here, θ and ϕ are the polar and azimuthal angles relative to the beam direction, respectively. The start counter consists of 24 scintillator paddles, positioned parallel to the beam line at a distance of 10.2 cm, each read out by a PMT, which is placed upstream beyond the maximum angle of acceptance to avoid interfering with charged particle trajectories produced in the target. The start counter scintillators have a thickness of only 2.0 mm to minimize the distortion of the particle trajectory due to multiple scattering.

To provide full coverage of the acceptance for target, each paddle has a straight rectangular section, the “leg”, and either a triangular or a trapezoid “nose” tapered inwards to increase the coverage of the detector at forward angles. The PMTs signals are digitized in TDCs and ADCs before being read out into the data stream [85]. The timing resolution of each start counter paddle varies from 292 to 324 ps.

4.2.5 Time-of-flight system

The flight time of particles crossing CLAS is measured by the TOF scintillation paddles. The TOF system covers the entire active range in azimuthal direction and a polar angle range from 8° to 142° . Each sector contains 57 TOF counters, located outside the tracking system and the Čerenkov counters. The scintillator thickness of 5.0 cm is chosen to provide a large signal for traversing particles. Each scintillator is perpendicular to the average local particle trajectory, and the width of each counter subtends about 1.5° of scattering angle. The paddles are aligned perpendicular to the beam direction in a hexagonal geometry. When a particle interacts in the scintillator, it produces scintillation light. The light is read out by PMTs optically connected to each end of paddles. The PMTs fit into a shadow region of the torus magnet coil to avoid further loss of detector acceptance. The PMT output signals are sent to ADCs, and via discriminator modules to TDCs. The ADCs and TDCs record the size and timing of the pulses, respectively. The scintillator paddles are 5.08 cm thick and vary in length from 32 cm to 445 cm depending on their location in the array. The time resolution of the TOF counters, whose dominant contributor is transit time variation of photon path in the scintillator, is from 150 ps for the shortest to 250 ps for the longest paddles [86].

4.2.6 Čerenkov counters

The Čerenkov Counter serves two dual function: triggering on electrons and separating electrons from pions. It is difficult to separate high energy electrons and pions by track curvature or $\Delta E/E$ techniques. An array of Čerenkov counters is positioned outside the drift chambers and within the TOF counters at forward angles up to $\theta = 45^\circ$ as seen in Figure 4.3a. The Čerenkov counter in each sector of CLAS is split into 18 regions of θ with its own set of mirrors and PMT. In each sector, the Čerenkov counters consist of two modules symmetrical about the central plane of constant ϕ . They are filled with perfluorobutane (C_4F_{10}), which has a high index of refraction (1.00153) corresponding to a pion threshold of 2.5 GeV/c. As a result, pions are discriminated up to this high momentum from electrons. Čerenkov radiation is emitted when a charged particle of very high velocity passes through the gas (perfluorobutane). To produce Čerenkov light in the medium, the minimum particle velocity is required,

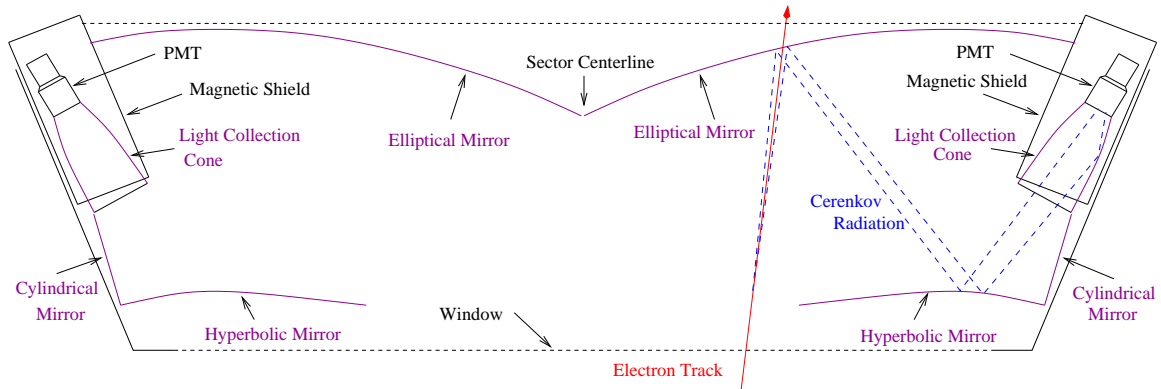


Figure 4.7: Čerenkov counter and an electron track through it [73].

which is called the Čerenkov threshold. Figure 4.7 shows the light-collecting cones and PMTs covering as much of the available space as possible with mirrors. The PMT and light collection cone are surrounded by magnetic shielding and placed in the shadow of the torus magnet coils.

The signal from the PMT is amplified and passed to a discriminator module. The logic output signal of the discriminator is sent to a TDC. It may be also used in the experimental trigger. The overall efficiency of the Čerenkov counters is above 99.5 % over most of the acceptance [87].

4.2.7 Forward electromagnetic calorimeter

The forward electromagnetic calorimeter (EC) is primarily responsible for the detection and event triggering on electrons above 0.5 GeV and neutral particles above 0.2 GeV. The neutral particles might be neutrons or photons from the decay of π^0 or η mesons. As seen in Figure 4.3a, the calorimeter covers the region from 8° to 45° in the polar angle with one module for each sector. It consists of six modules with the cross-section of an equilateral triangle. Figure 4.8 shows the layered structure of the electromagnetic calorimeter module and the arrangement of scintillation bars. Each module has 39 layers and each scintillator layer consists of 36 strips parallel to one side of the triangle. There are three orientations labeled U, V, and W, whose plane strips rotates by 120° in successive layers and each plane contains 13 layers.

The splitting of the EC module into an array of triangular cells is used to locate the area of energy deposition. Each array is further subdivided into an

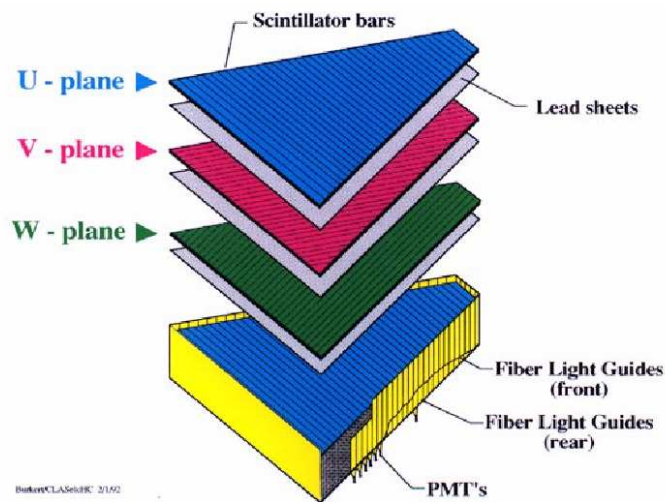


Figure 4.8: EC: The diagram shows the layered structure of the electromagnetic calorimeter and the arrangement of scintillation bars inside. The bars are aligned parallel to one of the three long sides of the module. The alignment is rotated for each consecutive layer, forming a grid [86].

inner and outer stack, to provide longitudinal sampling of the shower for improved electron/hadron separation. The readout is achieved using PMTs. For a typical signal from a 1 GeV electron, the PMT has an amplitude resolution of $\sim 4\%$ and time resolution of $100 \sim 150$ ps. The PMT gain is monitored during data-taking by periodic illumination of the PMT [88].

4.2.8 Large angle calorimeter

The Large Angle Calorimeter (LAC) is complementary to the EC and is used to detect scattered electrons and neutral particles such as neutrons and photons. The LAC covers only two of the six sectors of CLAS (a total of 120° in ϕ) with a range of the scattering angle $45^\circ < \theta < 75^\circ$. Similar in design to the EC, each unit is a sandwich of alternating square sheets forming a total of 33 layers and each layer is rotated at 90° to the previous one as seen in Figure 4.9. To improve discrimination between pions and electrons, LAC modules are divided into 17 inner layers and 16 outer ones. The light produced by the shower is collected at both scintillator ends. For 1 GeV electrons, the energy resolution is around 7.5% and it improves with increasing momentum. Timing

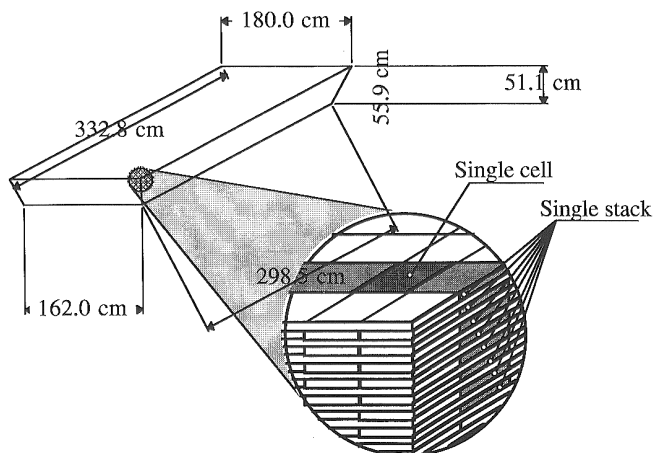


Figure 4.9: LAC: The arrangement of lead, Teflon, and scintillator layers inside a LAC module [89].

information is required to differentiate neutrons and photons. The timing resolution is 260 ps for neutron momenta above 0.5 GeV/c. The efficiency for the neutron detection is around 30 % [73].

4.3 Electron beam

The electron beam passes through a series of monitoring devices placed in the Hall-B extraction beam line and the beam dump tunnels. These devices measure the position and intensity of the electron beam.

Figure 4.10 shows the layout of these devices schematically. The properties of the electron beam are listed in Table 4.2.

4.3.1 Position, intensity and profile

Position and intensity of the electron beam are monitored by two beam position monitors (BPMs), each consisting of three resonant RF cavities. These measurements do not essentially destruct the beam. The BPMs are used to monitor continuously and maintain the position of the beam to be centered on the target. The beam is adjusted through a feedback loop during data-taking.

The electron beam current is measured in the Faraday cup which is only

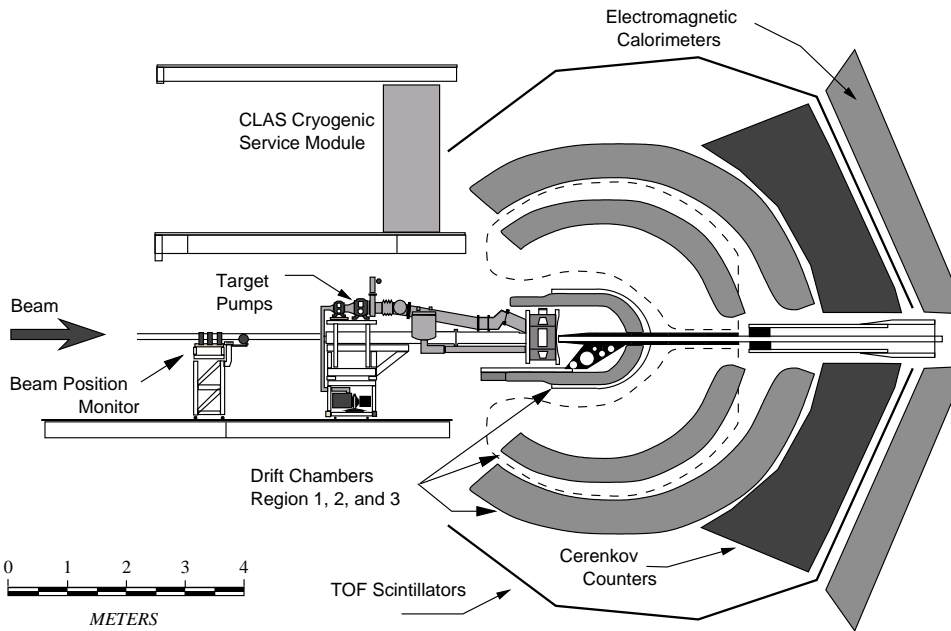


Figure 4.10: Beamline components in Hall B [73].

used in electron runs and is located downstream of the CLAS target. The Faraday cup comprises a 4000 kg block of lead placed on ceramic supports inside a vacuum. This operates by stopping the beam effectively and accumulating its charge. The beam charge is drawn off and measured continuously during operation. During photon experiments the electron beam is dumped after passing through the tagger magnet and traversing a screen used to determine the beam position.

Monitoring the profile of the electron beam is a destructive technique. The device for measuring the beam profile is called a harp. There are three harps along the beam line in the hall. The harp scan procedure intercepts the beam. Thus, it can only be performed when data is not taken. Harp scans are performed after any major changes to the electron beam or if other systems indicate problems. Each harp consists of a set of wires orientated along the two orthogonal directions, which are perpendicular to the beam. The harps are slid into the beam-line and moved at 45° through the beam during monitoring. A small fraction of the electrons is scattered by the wire. The PMTs, which are positioned downstream of the harps, are used to map out the profile of the beam.

Table 4.2: CLAS electron beam properties[73]

Quantity	Range	Precision	Monitor
Energy	0.8 ~ 6.0 GeV	$\delta E/E < 0.1\%$	Beam orbit stability
Polarization	40 ~ 85 %	$\delta P/P < 3\%$	Møller polarimeter
Position	± 3 mm of target center	100 μm	RF cavities
Width	$\sigma < 250\mu\text{m}$	10 μm	Wire scans
Current	1 ~ 30 nA	$< 1\%$	Faraday cup

4.3.2 Polarization

A high-precision measurement of the beam polarization is performed by measurements of the asymmetry in elastic electron-electron (Møller) scattering. When any parameters of the electron beam is changed, the beam polarization is measured. It takes about 10 ~ 15 minutes. This information is also used for the production of circularly polarized photons. This measurement is carried out with the Møller polarimeter, being moved into the beam-line for the duration of the calibration measurement. The polarimeter consists of a Permendur foil, a set of quadrupole magnets, and two detectors. The Permendur foil, which is a cobalt-iron alloy, is magnetized to produce a polarization of surface electrons along the plane of the foil. The magnets are located downstream of the foil. The beam polarization is measured by the asymmetry of the scattered electrons and the degree and direction of polarization of the target foil. The magnets separate the scattered Møller electrons from the unscattered beam and direct them to a pair of lead/scintillator-fiber composite detectors positioned on either side of the beam line. The degree of longitudinal polarization of the beam can be measured with a typical accuracy of better than 2 % [90].

4.4 Photon beam

Jefferson Lab (CLAS) uses the bremsstrahlung technique, which involves firing a relativistic electron beam through a thin radiator just upstream from a magnetic spectrometer. The electrons undergo bremsstrahlung in the field of the nuclei emitting photons in a wide energy range. These photon energies are

given by the difference between the electron beam energy and the energy of the deflected electrons. Hall B has three different photon-beam operation modes: a non-polarized mode, a circularly polarized mode, and a linearly polarized mode. Circular photon polarization results by polarization transfer from the longitudinally polarized electron beam. The linearly polarized photons can be produced by using a highly ordered, high purity crystal as a radiator. CLAS uses a gold foil for the circularly polarized photons and a thin diamond for the linearly polarized photons. The following sections describe the bremsstrahlung process in more detail.

4.4.1 The photon tagging system

The photon-tagging system can tag photons with electron energies up to 6 GeV. An electron that radiates a bremsstrahlung photon has lower momentum. Thus, it has smaller radius of curvature in the tagger dipole field. As a result, it emerges from the magnet along the open edge of the pole gap. Since the incident electron beam energy is well known, this allows the energy of the bremsstrahlung photons to be determined event by event. Figure 4.11 shows the photon-tagging system. The tagger is a C-shaped dipole electromagnet. The field in the tagger is set up such that electrons are directed into a beam dump in the floor of the experimental hall if they do not produce bremsstrahlung in the radiator. The electrons producing bremsstrahlung photons are dispersed in the magnet according to their momentum. Two planes of plastic scintillators positioned along the focal plane in the magnet measure timing and energy of the scattered electrons. The first plane is called the E-plane used to determine an energy information by “tagging” the electron position on the focal plane. It consists of 384 thin plastic-scintillator strips. Each strip covers the same momentum range. Since the counters overlap each other by a third of their width on each side, there is a total of 767 different tagger channels. The energy resolution is $0.001 \times E_{\text{electron}}$, where E_{electron} is energy of the incident electron. The geometry of the magnet and positioning of the hodoscope limits the tagger range to energies from 25 % to 95 % of E_0 [91].

The second plane is T-plane used to obtain timing information about each recorded electron. It is shifted by 20 cm downstream of the E-plane. The T-plane consists of 61 partly overlapping, thick scintillators that are read out by

PMTs on both ends. The scintillation light from the scintillators is recorded in two PMTs. The attainable root-mean-square (rms) timing resolution from the modules is 110 ps. The time difference between a hit in the T-plane and a track in CLAS can be used to identify the electron associated with the bremsstrahlung photon that interacted in the target.

However, the creation time of each photon can be determined to much greater accuracy than the intrinsic timing resolution of the T-counters. The electron beam bunches are delivered at 2.004 ns intervals and the timing is determined accurately from the RF signals. The beam bunches are only a few ps wide, and identifying the closer RF pulse to the measured time from the tagger, provides a more accurate event start time.

4.4.2 Collimation and monitoring

The photon beam downstream of the tagging magnet passes through a collimator. The beam is collimated before reaching the target by selecting photons with the highest degree of polarization. This is achieved by passing them through an aperture whose diameter is chosen to optimize the required polarization while maintaining a high photon flux. The 2.6 and 2.0 mm collimators were used during the FROST experiment. Any secondary electrons produced by the photon beam hitting the collimator material are removed with small sweeping magnets and the pair spectrometer magnet [73].

The precision of the beam flux is crucial for the measurement of a photo-production cross-section. The pair spectrometer, which consists of a thin foil for electron-positron pair production, a strong magnet, and a hodoscope, is positioned upstream from the target. Though it removes approximately 1 % of the photons from the beam, it allows for continuously monitoring the collimated photon flux during data-taking.

4.4.3 Circularly polarized photons

The way how to produce circularly polarized photons from linearly polarized electrons and the estimation of the photon polarization were discussed in section 3.5.2.

4.4.4 Linearly polarized photons

Linearly polarized photons are produced in the bremsstrahlung process using a crystalline radiator. Typically a diamond crystal is held at the desired angle to the beamline with a goniometer [92]. An electron scatters along a reciprocal lattice vector for a particular orientation of the crystal. The degree of linear polarization depends on the position of the coherent peak relative to the electron energy. For example, if the coherent peak is at an energy of about 30 % of the electron beam energy, the degree of polarization can reach up to 90 %. The degree of polarization depends strongly on the degree of collimation. The photon polarization is calculated analytically[93] using the energy of the scattered electron, the orientation of the crystal relative to the electron beam, and the degree of collimation.

4.5 Data acquisition

The data-acquisition (DAQ) system puts the digitized ADC/TDC outputs from the various detectors together and stores the information for later off-line analysis. The arrays of digitized values are assembled into tables and transferred to the main CLAS on-line acquisition computer (CLON) in the control room. The tables are elaborated into “banks” with the addition of headers and data labels. Some are grouped together into larger banks describing extended systems [94]. Three primary processes are the Event Builder (EB), Event Transport (ET), and Event Recorder (ER). The EB combines the corresponding banks into whole events and labels those with a run number, event number, event type, and other information in a header bank. The event having the final format is ready by now for off-line analysis. The EB passes the complete events to shared memory on the online computer, and this shared memory is managed by the ET system. The ET allows access by event producer and consumer. The ER writes the data to magnetic media. The output files are written across the local array of RAID disks. Finally, it is transferred along a fiber link for permanent storage on a tape silo. Some events are also sent for on-line monitoring, reconstruction and analysis on other computers.

The CEBAF On-line Data Acquisition system (CODA) controls the DAQ process and all communication with detectors, starting and ending runs. The first stage is DAQ configuration. During the download procedure the detector

parameters are loaded from a prepared run configuration file, relevant software is downloaded to the detector readout controllers, and the correct EB processes are set up. Next as prestart, loaded run parameters are checked against the original run configuration set, and information about current run conditions is written to the database and parameter files. Then, the run is started. The trigger is enabled and data begins to accumulate in 2 GB files.

Data acquired during the experiment is written into BOS (Bank Object System) files which are kept on the JLab data storage silo. The “raw” data files written during the experiment contain detector-specific information, detector status flags, scalar events, epics events, and helicity events. In the process of calibration the data is “cooked” where raw information is translated into physical quantities using calibration parameters. New banks containing physics observables are also added to the data-stream. The BOS data files are converted into a more compact ROOT DST (Data Summary Tape) format during the cooking process.

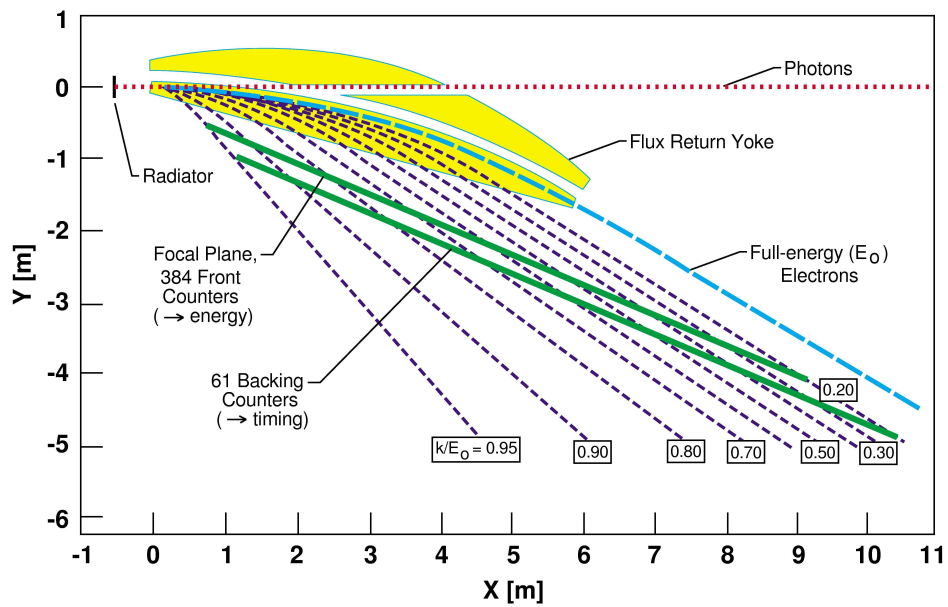


Figure 4.11: The tagging spectrometer in cross-section: The photon beam, the paths of scattered electrons deflected in the tagger magnetic field and the two planes of the scintillator hodoscope [91]. E_0 is energy of the incident electron, E_{electron} .

Chapter 5

Data Analysis 1: Event Selection

Data with circularly polarized photon beam and the longitudinally polarized butanol target were collected during the FROST experiment. The raw data were translated into physical quantities kept in data banks contained in data files. For the $\gamma p \rightarrow p\pi^0$ reaction, EVNT, TAGR, TGBI, SCPB, STPB, MVRT, and HEAD data banks, which are calibrated DST files, were selected. The “ROOTBEER” program package that based on ROOT/C++ was used to analyze data.

Due to the huge amount of data, it was important to eliminate unnecessary events from the analysis as much as possible, so that the final results had less uncertainties.

This chapter discusses the events selection including the target selection.

5.1 Data reduction procedure

The raw data were reduced for the $\gamma p \rightarrow p\pi^0$ channel using the missing-mass technique. The missing-mass technique was used assuming the two-body reaction $\gamma p \rightarrow pX$, where X is the particle hypothesized to be missing. The steps of this analysis are the following:

1. Identifying the recoil protons by their velocity and momentum relation (Section 5.2.1).
2. Reducing the backgrounds by
 - (a) removing inefficient TOF paddles (Section 5.2.2),

- (b) cutting out events reconstructed in inactive regions of CLAS (Section 5.2.3),
 - (c) choosing the correct beam photon for each event (Section 5.2.4),
 - (d) removing the low-momentum protons (Section 5.2.6), and
 - (e) cutting out events with recoil protons at larger scattering angles than the calculated limits for a two-particle reaction (Section 5.2.7).
3. Identifying the π^0 meson by placing a 3σ cut around the π^0 peak in the missing-mass spectrum for each sector (Section 5.3).
 4. Selecting events within the butanol target by choosing the suitable range of the vertex position (Section 5.4).
 5. Determining scale and dilution factors to remove the background of bound nucleon reactions using events from the carbon target (Section 6.3.1 and 6.3.2).
 6. Distributing the events of the resulting missing-mass spectra into the bins defined by incident photon energy, E_γ , and center-of-mass scattering angle of π^0 , $\cos\theta_{\text{c.m.}}^{\pi^0}$, based on the assumption that the reaction observed is $\gamma p \rightarrow p\pi^0$ (Chapter 8).

5.1.1 Charge and momentum

The direction of the charged particles are bent because of the toroidal magnetic field \mathcal{B} in CLAS. Therefore, their charge q is determined by the direction in which the particle goes through the DC. The radius of curvature yields information on their momenta. For constant \mathcal{B} , the momentum p of a particle is given by

$$p = q(r \times \mathcal{B}), \quad (5.1)$$

where r is the curvature radius of the particle's track. The toroidal magnetic field in CLAS is always approximately perpendicular to the momentum of the particles. Thus, it maximizes the sensitivity of the track curvature to small differences in momentum.

5.1.2 Velocity

The velocity or β [= velocity (v) / speed of light (c)] is determined by the path length, Δd and the flight time of a particle, Δt_p ,

$$\beta = \frac{\Delta d}{c\Delta t_p}. \quad (5.2)$$

The path length is the distance between the start counter and the time-of-flight detector for the proton path, and the time difference was determined by the difference between the time recorded by the start counter and the scintillation counter of the time-of-flight detector.

5.1.3 Event vertex

The vertex, the interaction point of the target proton with the beam photon, is given by the beam axis and the extrapolated track of the recoiled proton. The time and vertex position are important in choosing the correct photon corresponding to the detected proton, and also determining the target (butanol, carbon, or polyethylene). However, during this experiment the photon beam was not on the z-axis, and the position of the actual photon beam inside the target was not well known. Thus, the vertex point is an approximation. Moreover, the interaction point was shifted due to the solenoidal holding field.

5.2 Event reconstruction for the $p\pi^0$ final state

5.2.1 Particle ID $\Delta\beta$ cut

The first step to choose events of the reaction $p\gamma \rightarrow \pi^0 p$ is to select events having (1) start counter hit, (2) drift chamber track, and (3) time-of-flight counter hit. After that, events which contain only one positive particle were selected. Only events with one positive particle are retained for further analysis.

Under these conditions, the β vs. momentum distributions of all positive particles are plotted, shown in Figure 5.1. Since $\beta (= p/E = p/\sqrt{m^2 + p^2})$ depends on the mass of the particle, the particle has a specific value of β at its particular momentum. The plots highlight the excellent separation of

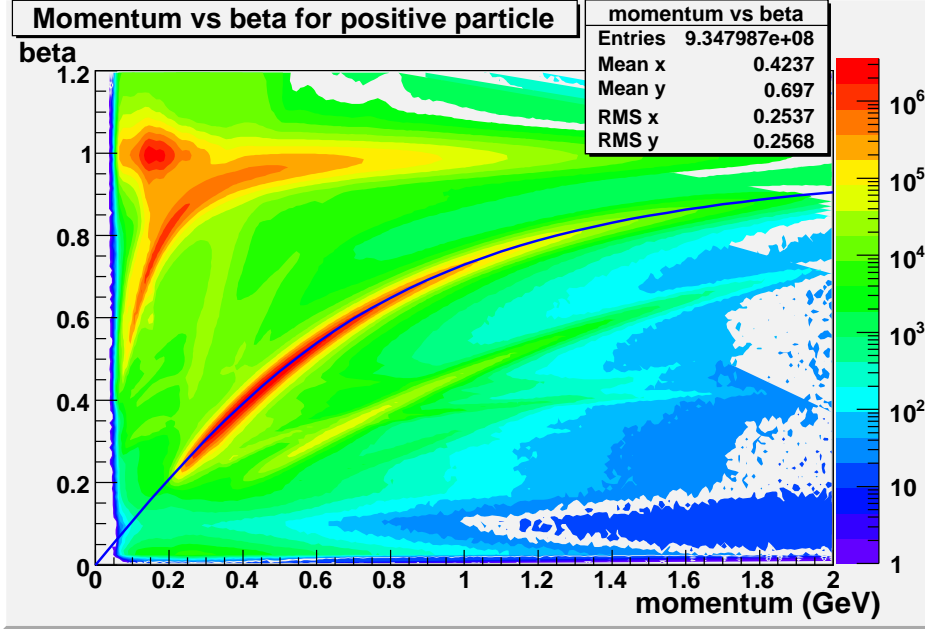


Figure 5.1: Momentum vs. beta for the all positive particles. Blue line is the β_c with the invariant mass of proton, m_p .

the proton and other positive particle events. The next step is to choose proton events from positive particle events. To select a proton from all positive particles, a calculated β ($= \beta_c$) based on the invariant mass of the proton, $m_p = 0.93827/c^2$ GeV was used.

$$\beta_c = \frac{p}{E} = \frac{p}{\sqrt{m_p^2 + p^2}} \quad (5.3)$$

The calculated locus for proton is shown by the blue line (β_c), overlaid on the plot.

A selection of protons is obtained using a momentum-dependent β cut. This is achieved by plotting the difference between the measured β ($= \beta_m$) and the calculated β_c above. To get more precise β_m , STPB and SCPB banks are used.

$$\beta_m = \left(\frac{v}{c}\right)_m = \frac{\text{distance between hit position on ST and hit position on TOF}}{(\text{flight time between ST and TOF}) \times c}, \quad (5.4)$$

where ST, TOF, and c are the start counter, the time of flight, and the speed of light, respectively. Since the proton mass is heavier than other positive

particles and it causes the larger energy losses throughout the detector, β_m was used as a measured β .

$$\Delta\beta = \beta_m - \beta_c = \frac{\text{the distance between SC and TOF}}{(\text{the time between SC and TOF}) \times c} - \sqrt{\frac{p^2}{m_p^2 + p^2}}. \quad (5.5)$$

Figure 5.2 shows the resulting distributions of $\Delta\beta$ versus momentum. The 2-D

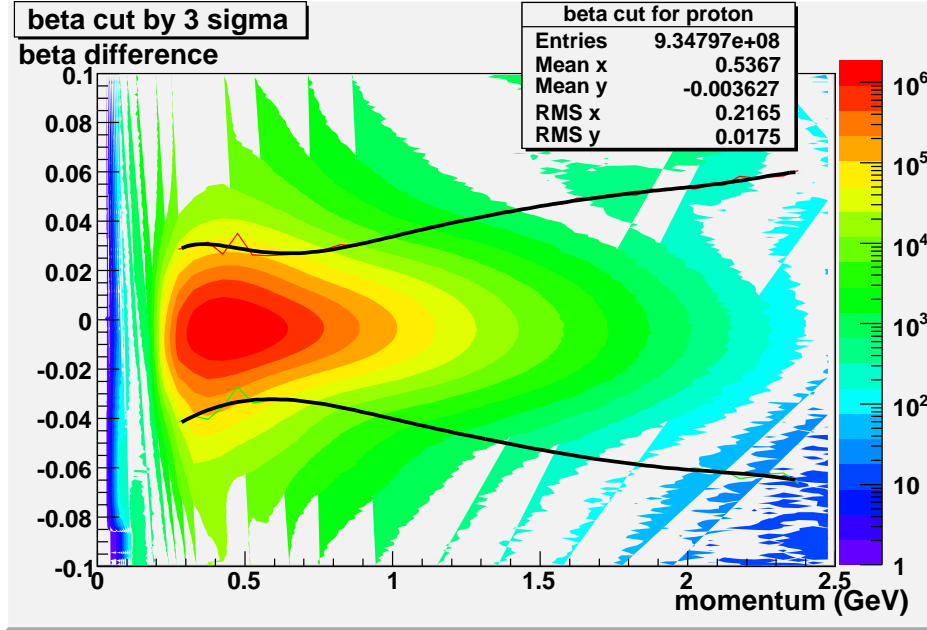
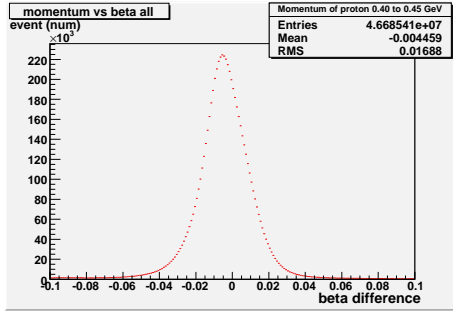


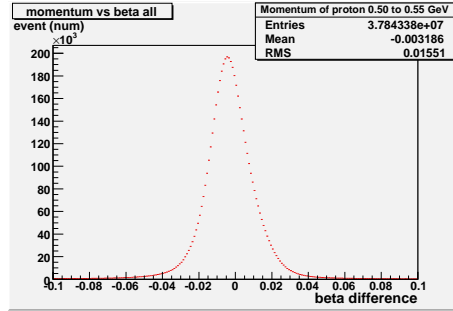
Figure 5.2: Momentum vs. beta difference before the cut by $\Delta\beta = \pm 3\sigma$. The curved lines are the mean of the *peak* $\pm 3\sigma$.

distributions were divided into 1-D projections along the momentum axis in bins of 50 MeV/c. The peaks around $\Delta\beta = 0$ correspond to the particle of interest. Each peak of 1-D histogram in Figure 5.3 was fitted with a Gaussian function. The parameters, peak position x_m and standard deviation σ , were extracted from the fitted Gaussian and used to apply a cut. The cut range, $(x_m \pm 3\sigma)$, as function of the momentum was parametrized by fitting eighth-order polynomials to the extracted positions of the 3σ edges, shown curved black lines in Figure 5.2. All events outside these black lines were discarded. Figure 5.4 shows $\Delta\beta$ and β vs. momentum after applying the $\Delta\beta$ cut.

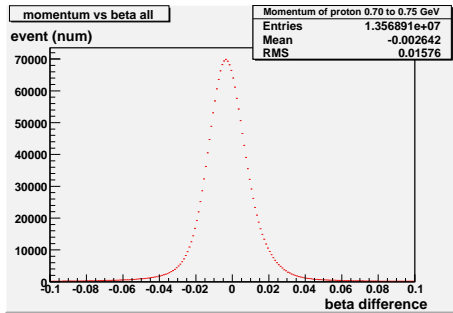
The effect of the cut can be observed in Figure 5.5, the mass of the positively



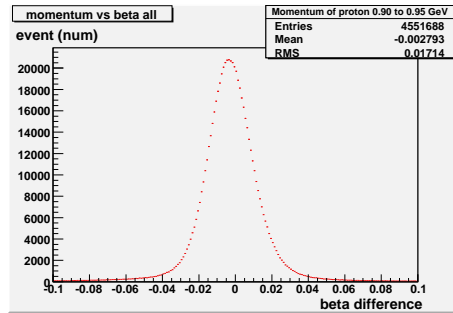
(a) $p_{proton} = 0.40 \text{ GeV to } 0.45 \text{ GeV}$



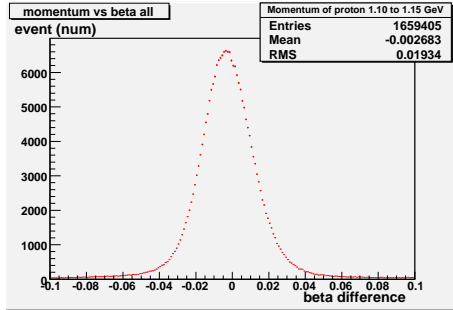
(b) $p_{proton} = 0.50 \text{ GeV to } 0.55 \text{ GeV}$



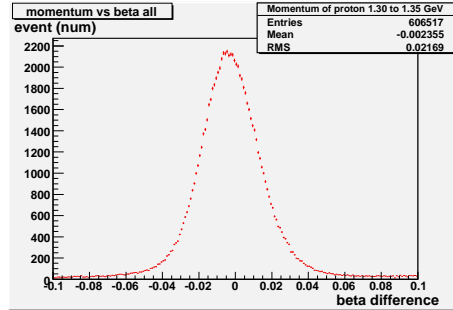
(c) $p_{proton} = 0.70 \text{ GeV to } 0.75 \text{ GeV}$



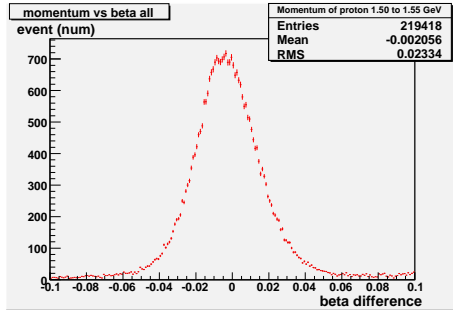
(d) $p_{proton} = 0.90 \text{ GeV to } 0.95 \text{ GeV}$



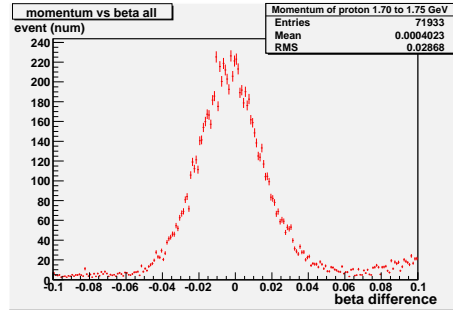
(e) $p_{proton} = 1.10 \text{ GeV to } 1.15 \text{ GeV}$



(f) $p_{proton} = 1.30 \text{ GeV to } 1.35 \text{ GeV}$

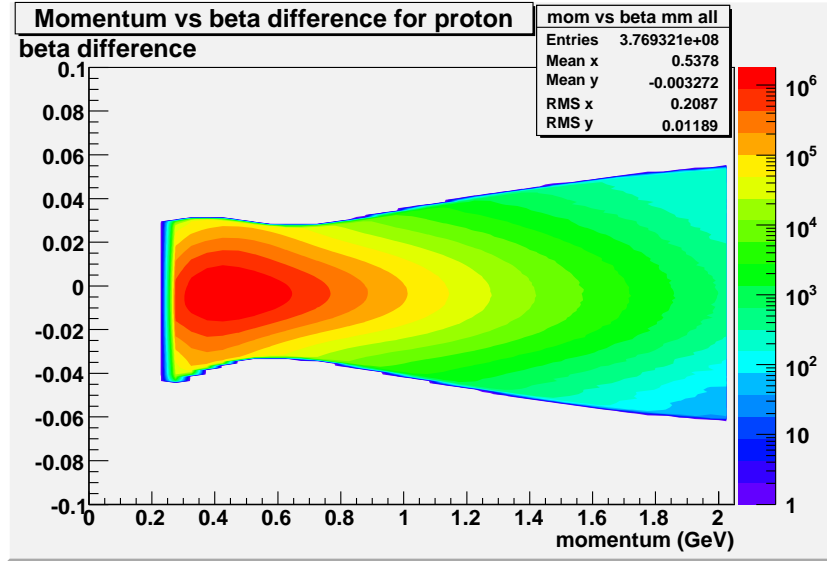


(g) $p_{proton} = 1.50 \text{ GeV to } 1.55 \text{ GeV}$

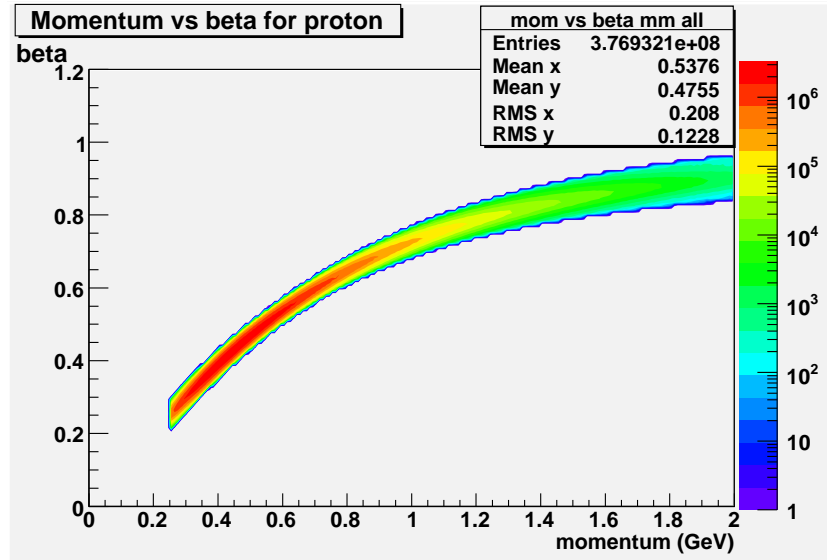


(h) $p_{proton} = 1.70 \text{ GeV to } 1.75 \text{ GeV}$

Figure 5.3: The figures show the beta difference for different momentum intervals.



(a) beta difference vs. momentum



(b) beta vs. momentum

Figure 5.4: (a) beta difference vs. momentum, and (b) beta vs. momentum for proton after the cut by eight-order polynomials based on $\Delta\beta \pm 3\sigma$. Events in which the proton momentum is less than 250 MeV are omitted in these figures.

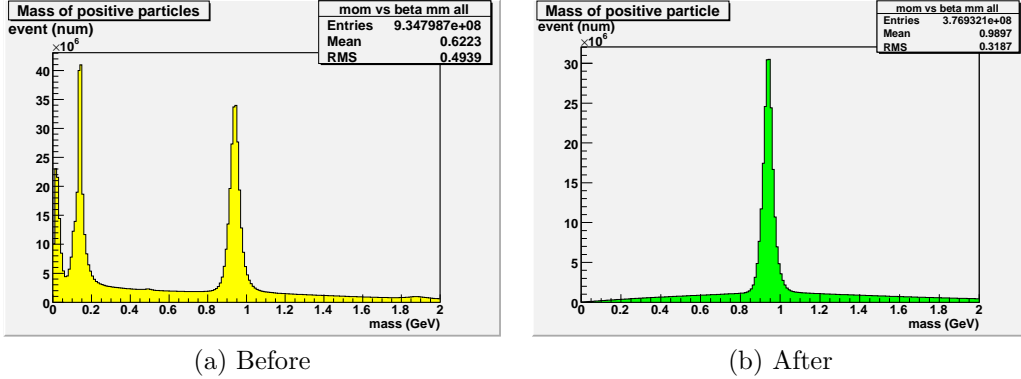


Figure 5.5: Mass of positive particles before (a) and after (b) the cut by eight-order polynomials based on $\Delta\beta \pm 3\sigma$. The events still include other than $\gamma p \rightarrow \pi^0 p$.

charged particles (a) before and (b) after the $\Delta\beta$ cut. The distributions of β_m versus momentum before and after the $\Delta\beta$ cut are in Figure 5.1 and Figure 5.4b . It shows a clean selection of the proton band.

The four-momentum of the proton was constructed from a calculation of the particle's energy, E , based on its known mass, $m_p = 0.93827/c^2$ GeV:

$$E^2 = m_p^2 + p^2. \quad (5.6)$$

5.2.2 Remove inefficient paddles

In order to the study the efficiency of TOF paddles, the number of events and the angular distributions of each paddle were investigated. Since CLAS is symmetric around the azimuthal angle, the number of events and the angular distribution are the same or similar for each sector. It means that paddles with the same paddle number for each sector would have the same number of events and angular distributions. Each group of six paddles for different sectors was compared. The paddles that had huge differences in their number of events and/or angular distributions were identified as inefficient paddles and were removed from this analysis. Below is the list of inefficient paddles.

Sector 1: paddle number 17, 24, and 36,

Sector 2: paddle number 44 and 45,

Sector 3: paddle number 13, 44, and 47,

Sector 4: paddle number 23,

Sector 5: paddle number 23 and 51,
 and Sector 6: paddle number 24, 44, and 46.

5.2.3 Fiducial cuts

The sample of events had to be further refined to ensure accurate four-momentum determination. This was done by removing proton events detected in the inactive regions of CLAS, which is referred to as “non-fiducial regions”, their regions are outside the sensitive volumes of the detectors, e.g. the coils of the torus magnet. Although the coils themselves will block the particles, the magnetic field in the regions immediately changes the particle’s position, therefore it cannot be mapped accurately. Events in those regions have a large systematic uncertainty in their trajectory and momentum.

Figure 5.6, shows the angular distributions of proton tracks. The six active

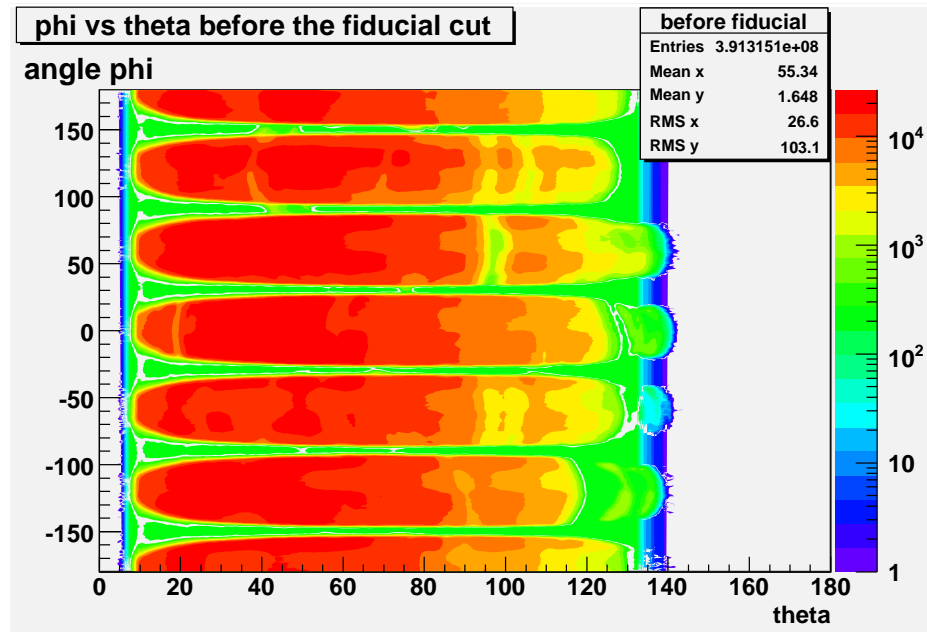


Figure 5.6: The angular distribution of proton hit by sector.

sectors of CLAS are clearly evident as regions with a high yield of particles, while the coils of the torus magnet result in strips of low statistics centered at $\phi = -150^\circ, -90^\circ, -30^\circ, 30^\circ, 90^\circ, 150^\circ$. The very forward polar angles have low

statistics because of the hole for the beam line. Events which came from these inactive regions were removed. The regions are as follows:

- (1) $\theta < 9^\circ$,
- (2) $9^\circ \leq \theta < 40^\circ$ and $\phi \geq 25.0^\circ \times [(\theta - 9.0)/(40.0 - 9.0)]^{0.25}$, and
- (3) $\theta \geq 40^\circ$ and $(-155^\circ < \phi < -145^\circ$ or $-95^\circ < \phi < -85^\circ$ or $-35^\circ < \phi < -25^\circ$ or $25^\circ < \phi < 35^\circ$ or $85^\circ < \phi < 95^\circ$ or $145^\circ < \phi < 155^\circ)$.

Figure 5.7 shows the angular distribution of proton tracks after the fiducial

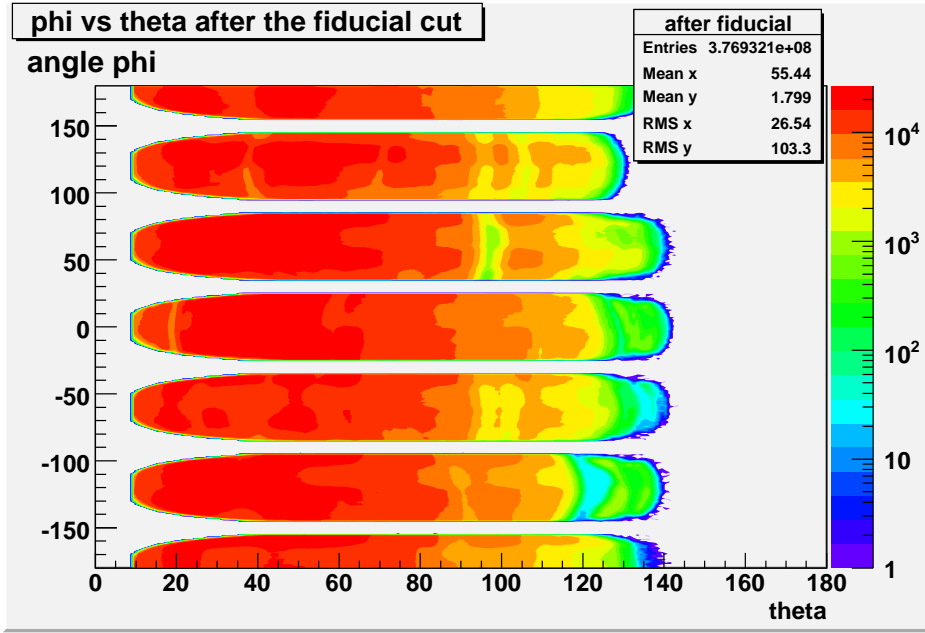


Figure 5.7: The ϕ and θ distribution after the fiducial cuts.

cuts. After applying fiducial cuts the number of events was reduced to 96.4% of its value.

5.2.4 Identify the incident photon

The tagged photon momentum and its interaction time are analyzed in the tagging hodoscope. In order to determine the photon that produced the photo-nuclear reaction observed in CLAS, the correct hit in the tagger focal plane had to be identified.

Timing correlation between the calculated arrival time of the photon at the vertex $t_{\gamma v}$ and the vertex time of the final-state proton t_{pv} was used to identify

the incident correct photon for each event. The average number of photons per event was around $3 \sim 8$ (Figure 5.8) after choosing “good” photons (status =

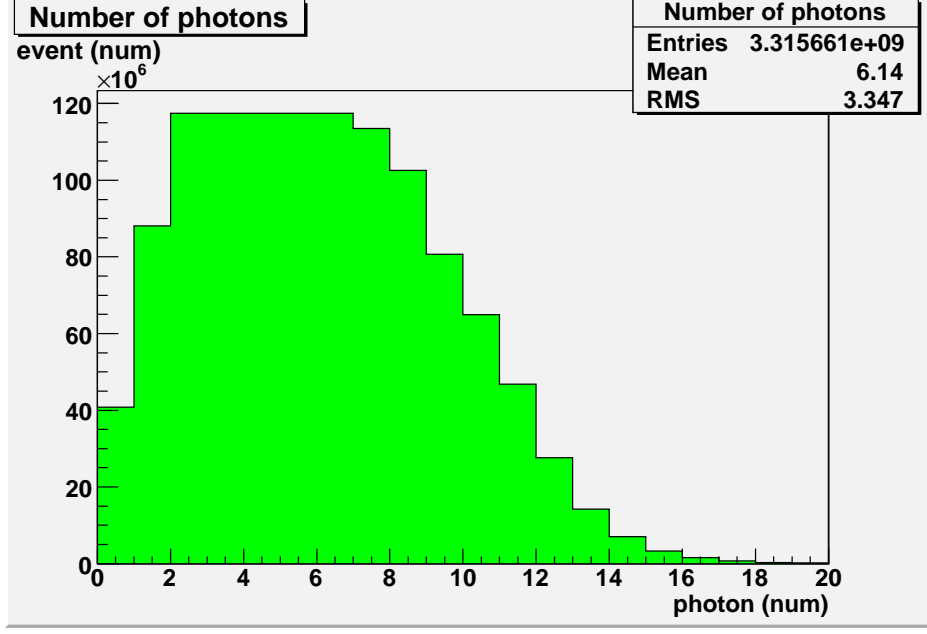


Figure 5.8: The number of photons per event with one proton.

7 or 15 in TAGR bank).

t_{pv} is given by

$$t_{pv} = t_{sc} - \frac{\Delta d}{c\beta_m}, \quad (5.7)$$

where t_{sc} is the time at the TOF counter, Δd is the distance from the beamline (vertex) to the TOF counter, and β_m is determined by Eq. (5.4). On the other hand, $t_{\gamma v}$ takes into account the variations in the position of the reaction vertex with respect to the CLAS center:

$$t_{\gamma v} = t_{\gamma o} + \frac{z_v + d_{\text{off}}}{c}, \quad (5.8)$$

where $t_{\gamma o}$ is the time of photon arrival at the center of CLAS, z_v is the z-component of the vertex, and d_{off} is the offset of the target center from the center of CLAS along the beam axis. During the FROST experiment, the center of butanol target had been the center of CLAS ($d_{\text{off}} = 0$). Since during the FROST experiment, the photon beam had not been centered exactly on

the z-axis, the MVRT bank was used to provide the vertex position of the beam photon. (The x, y offsets of the event vertex were neglected.)

The time difference between the reaction time of the proton t_{pv} and the tagger information $t_{\gamma v}$ is

$$\Delta t = t_{pv} - t_{\gamma v}. \quad (5.9)$$

Figure 5.9a shows this time difference, Δt . The small neighboring peaks at 2 ns

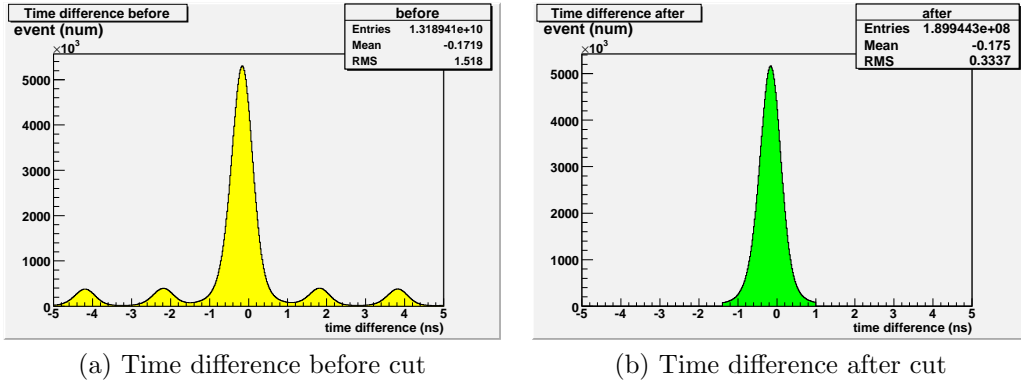


Figure 5.9: (a) Time difference between the reaction time and the tagger information and (b) time difference within the smallest $|\Delta t|$.

intervals arise from photons produced from other electron beam bunches. To discriminate contributions from nearby electron beam bunches, only photons within the smallest $|\Delta t|$ were chosen. The vertex position and the time $t_{\gamma v}$ are approximations because the photon beam position is not well known (Section 5.1.3).

After the correct photons were chosen, the strange tails of the proton mass distribution were removed, which is shown in Figure 5.10.

5.2.5 Energy loss correction

Between the event vertex and the drift chamber, the particles passed through a significant amount of material such as the butanol target, the target cell walls, the heat shields, holding coils, start counter, and vacuum box. These materials result in significant energy loss for the particles. The measured four-momenta of the particles, corrected for energy loss, were used in the subsequent analysis. Figure 5.11 shows the β distribution of proton before and after the energy loss

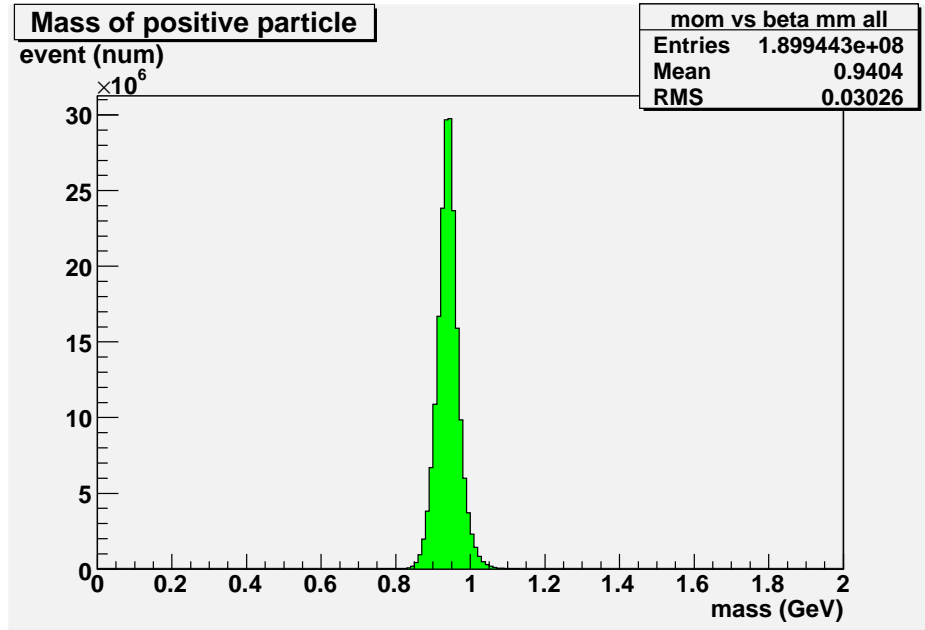
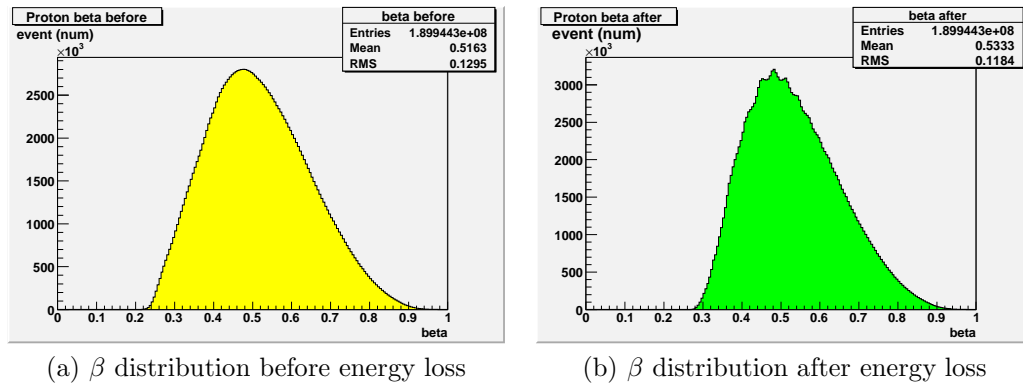


Figure 5.10: Mass of positive particles after selecting only "good" photons.



(a) β distribution before energy loss

(b) β distribution after energy loss

Figure 5.11: β distribution (a) before and (b) after the energy loss correction.

correction. As shown in Figure 5.12a the mean value of difference of β between before and after the energy loss correction is about 0.017. Figure 5.12b shows the energy difference of proton between before and after the energy loss correction is 2 ~ 60 MeV.

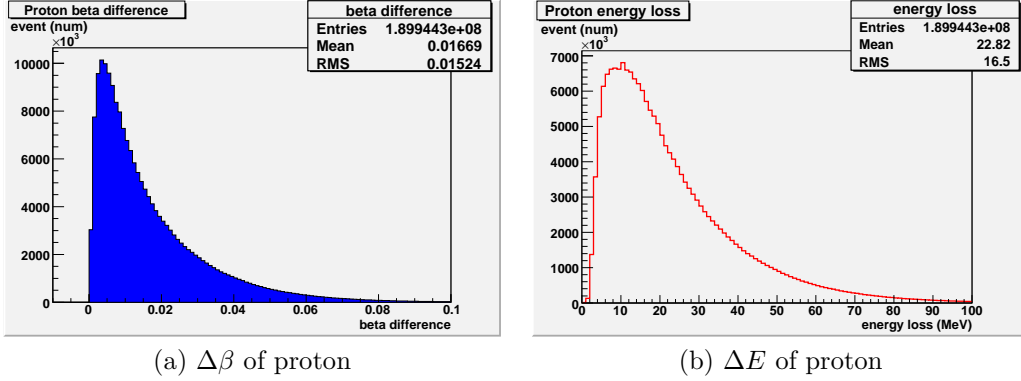


Figure 5.12: (a) $\Delta\beta$ and (b) ΔE distributions of proton between before and after the energy loss correction.

5.2.6 Momentum cut

The proton must have at least a certain momentum to be detected in CLAS. There are at least two reasons for this. (1) If a proton doesn't have enough momentum, it cannot reach the drift chamber. (2) The lower the momentum of a proton, the more energy loses in materials outside of targets. It means that even though the DC resolution results in smaller errors for low-momentum tracks than for high-momentum ones, a proton with low momentum might have big errors. Thus, protons with momenta less than 350 MeV/c were removed from my analysis.

5.2.7 Scattering angle cut

In the kinetic analysis of a two-body nuclear interactions, the four-momentum conservation leads to a relation between the angle and momentum of the interacting particles with given masses and energies. As a result, it imposes a limit on the angle in the laboratory system for the recoiling proton (see Fig. 5.13):

$$\sin^2\theta_{pr}(E_\gamma) \leq \frac{[(E_\gamma + m_p)^2 - E_\gamma^2 + m_p^2 - m_{\pi^0}^2]^2 - 4m_p^2(m_p^2 + 2m_p E_\gamma)}{4m_p^2 E_\gamma^2}, \quad (5.10)$$

where θ_{pr} , E_γ , m_p and m_{π^0} are the scattering angle of a recoil proton in the laboratory system, the incident photon energy, the mass of proton, and the mass of π^0 , respectively.

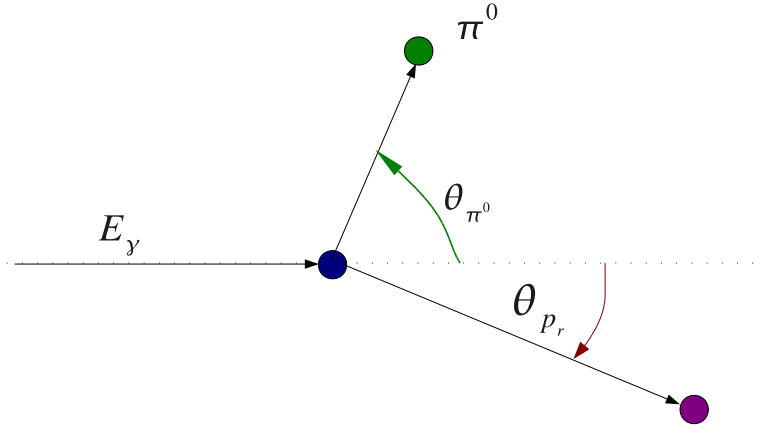


Figure 5.13: The angles of pion and proton in the laboratory system.

The maximum scattering angle θ_{p_r} for recoil protons which only depends on E_γ increases with E_γ . The same scattering angle can be determined from the recoil proton energy, E_p , or its three momentum, p_{p_r} , the scattering angle of π^0 , θ_{π^0} , and the energy of π^0 , E_{π^0} in the laboratory system.

$$\cos \theta_{p_r} = \frac{E_\gamma - (E_{\pi^0}^2 - m_{\pi^0}^2)^{1/2} \cos \theta_{\pi^0}}{p_{p_r}}. \quad (5.11)$$

Since there is no limit of minimum scattering angle θ_{π^0} , $\theta_{\pi^0} = 0$ was put to get the maximum angle of θ_p .

These equations, (5.10) and (5.11), assist to identify the correct interaction, for example, to remove the bound nucleon reaction. Since proton momentum cut had been performed, the maximum scattering angle by E_γ was calculated substituting $p_p = 350$ MeV. The resulting maximum angles are given in Table 5.1. This scattering angle cut was applied only for events from the butanol target.

E_γ (GeV)	W (GeV)	max θ_p (degree)	E_γ (GeV)	W (GeV)	max θ_p (degree)
0.40	1.277	66.28	1.50	1.922	81.67
0.50	1.349	70.51	1.60	1.970	81.03
0.60	1.416	73.29	1.70	2.018	82.36
0.70	1.481	75.26	1.80	2.064	82.65
0.80	1.543	76.74	1.90	2.109	82.91
0.90	1.603	77.90	2.00	2.153	83.15
1.00	1.660	78.83	2.10	2.196	83.36
1.10	1.716	79.59	2.20	2.238	83.56
1.20	1.770	80.23	2.30	2.280	83.75
1.30	1.822	80.78	2.40	2.320	83.91
1.40	1.873	81.25			

Table 5.1: Maximum scattering angles of proton θ_p in the laboratory system when the momentum of proton is more than 350 MeV/c. E_γ and W are the energy of incident photon (in the laboratory system) and total energy in c.m.

5.2.8 ϕ dependence of the missing mass

Figure 5.14 shows that apparently the π^0 mass depends on the sector, or azimuthal angle ϕ at which the proton was detected.

The mass difference between maximum and minimum is about 30 MeV after the energy loss corrections. The reasons might be the following:

(1) The position of the torus coils after cooling to 4 K was different than the position of the warm coils. As a result, the magnetic field was not symmetric for each sector.

(2) If the center of the holding coil was not positioned along the beam line, a charged particle (proton) bends differently in each sector.

(3) If the center of the photon beam was off from the center of the target, the energy loss differs by sector (or ϕ). Since we do not know the exact position of a beam photon inside the target but only the mean position of the beam, this might cause that each sector has different π^0 mass peak.

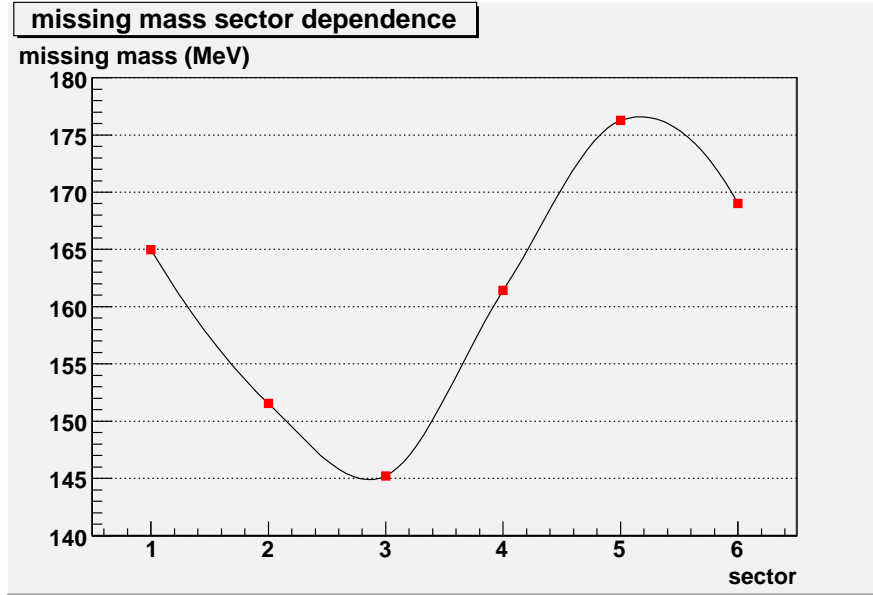


Figure 5.14: The red points are the mean values of missing mass of π^0 by sector. The figure clearly shows the missing mass of π^0 (after the energy loss correction) depends on sector, or azimuthal angle ϕ .

5.3 Missing-mass squared cut

The proton candidates were selected by the particle ID $\Delta\beta$ cut from the raw data. Then events, which were detected in the inefficient TOF paddles, detected in the inactive regions of CLAS, produced by photons of the different electron bunches from those of recoil protons, having larger proton scattering angles than the limits given by four-momentum conservation, were removed. Therefore, these candidates might be protons with higher probability than before.

The steps take the data to a stage that we can now calculate the missing mass of the reaction $\gamma p \rightarrow pX$ using the four-momentum conservation:

$$m_X^2 = (E_\gamma + m_p - E_{p2})^2 - (\vec{p}_\gamma - \vec{p}_{p2})^2, \quad (5.12)$$

where E_γ and \vec{p}_γ are energy and momentum of the incident beam photon, E_{p2} and \vec{p}_{p2} are energy and momentum of the recoiling proton, and $m_p = 0.93827 \text{ GeV}/c^2$ is the proton mass. Figure 5.15 shows a missing-mass squared distribution. The sharp peak corresponds to π^0 . The mean value of the π^0 mass is around $160 \text{ MeV}/c^2$ after the energy loss correction.

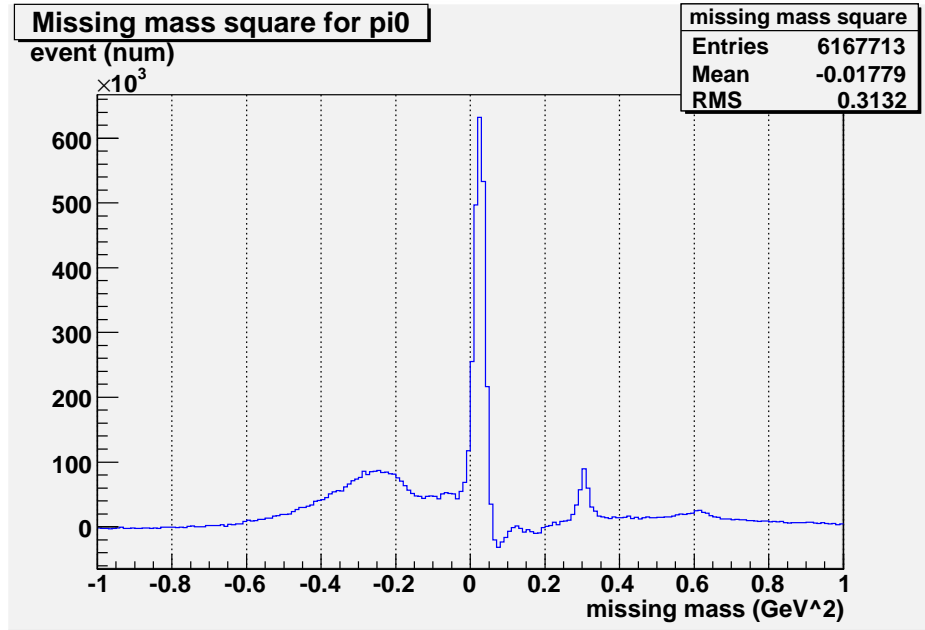
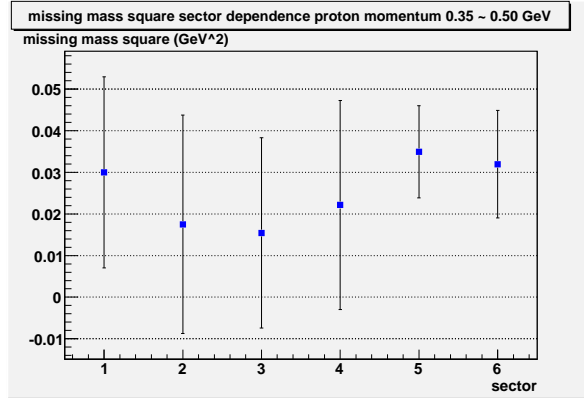


Figure 5.15: Missing-mass squared distribution, here for the reaction $\gamma p \rightarrow pX$ after subtraction of scaled carbon yield and energy loss correction.

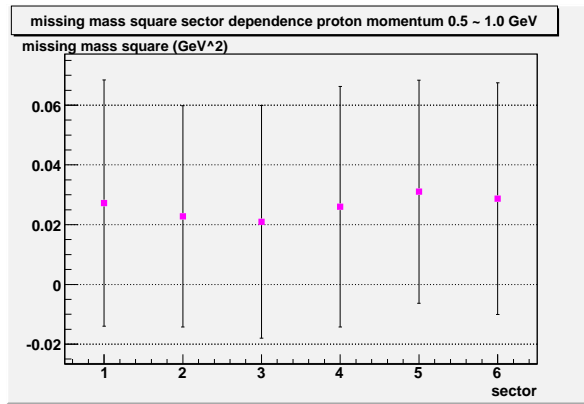
As shown in Figure 5.16 the missing-mass squared depends not only on sector, but also on proton momentum. The events were divided by sectors and by the three ranges of proton momentum (a) $0.35 \text{ GeV}/c \sim 0.5 \text{ GeV}/c$, (b) $0.5 \text{ GeV}/c \sim 1.0 \text{ GeV}/c$, and (c) $p_{p2} > 1.0 \text{ GeV}/c$. A total of 18 different mean values and σ 's were used to identify the π^0 . The missing-mass squared cuts were applied at mean value $\pm 3\sigma$. The lower cut was always limited to $0.0 \text{ GeV}^2/c^4$.

5.4 Event vertex and selection of targets

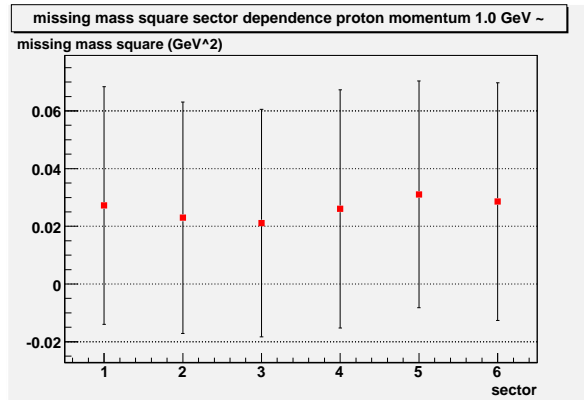
At this stage of analysis, the final state $\pi^0 p$ events have been identified. The last step of the event selection is to choose the vertex location which must be within the targets. Three different targets, butanol (C_4H_9OH), carbon (C), and polyethylene (CH_2) were used during the experiment. The size and location of these targets are in Table 5.2 and Figure 5.17. The butanol target was located at $z = 0$, the CLAS center. The carbon and the polyethylene targets were located downstream of the butanol target. The distribution of



(a) proton momentum 0.35 ~ 0.5 GeV



(b) proton momentum 0.5 ~ 1.0 GeV



(c) proton momentum 1.0 GeV ~

Figure 5.16: The figure shows the mean values of missing-mass squared and mean $\pm 3\sigma$ by sector and by proton momentum (a) 0.35 GeV \sim 0.5 GeV, (b) 0.5 GeV \sim 1.0 GeV, and (c) $p_{p2} > 1.0$ GeV/c. Only positive values of the missing-mass squared are chosen for π^0 candidates.

Table 5.2: The location of three targets, butanol, carbon, and polyethylene.

Target	Size		Location z^1 from CLAS Center (cm)
	length	diameter	
butanol (C_4H_9OH)	5.28 cm	1.5 cm	$-2.64 \leq z \leq +2.64$
carbon (C)	1.2 mm		+ 6.15 cm (downstream)
polyethylene (CH_2)	3.45 mm		+ 15.95 cm (downstream)

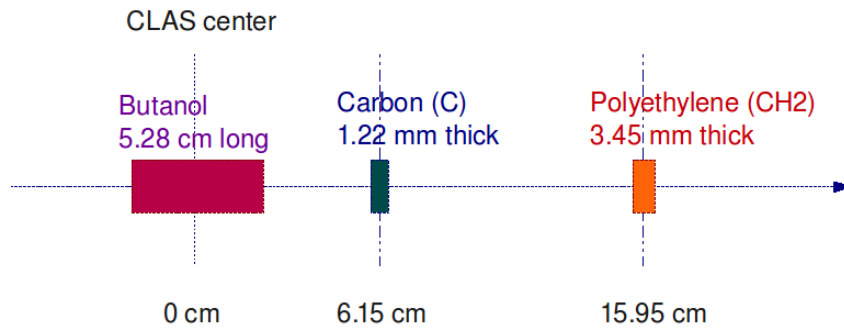


Figure 5.17: The positions of butanol, carbon, and polyethylene.

the vertex positions is shown in Figure 5.18. The size of area of each target depends on the length (or thickness) of the targets. Since the photon beam spread out from the beam line, the vertices are broad.

A cut on the butanol target was applied on events having vertices in the range $-27.5 \text{ mm} < z < +27.5 \text{ mm}$ which includes the butanol cell. A cut on the carbon target was applied in the range $+50 \text{ mm} < z < +80 \text{ mm}$, and on the polyethylene target it was $+140 \text{ mm} < z < +180 \text{ mm}$.

5.5 Missing mass sorted by different helicity states and targets

After the target selection, events for each target were studied. Figure 5.19 shows missing mass vs. E_γ and missing mass vs. proton momentum distributions with different targets before the missing-mass squared cut.

In addition, the missing-mass distributions for different helicity states and

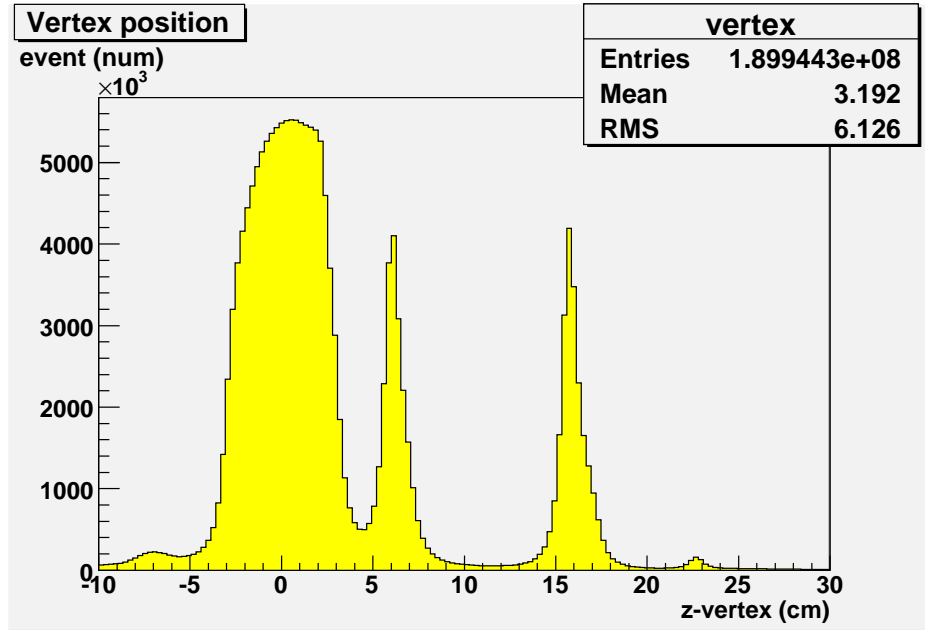
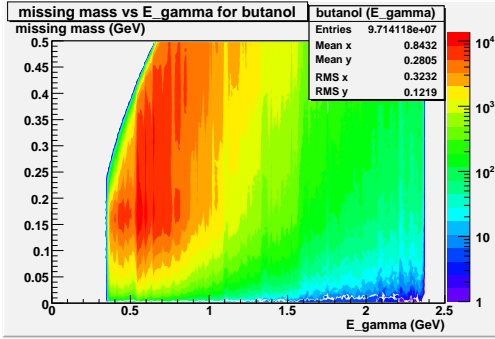
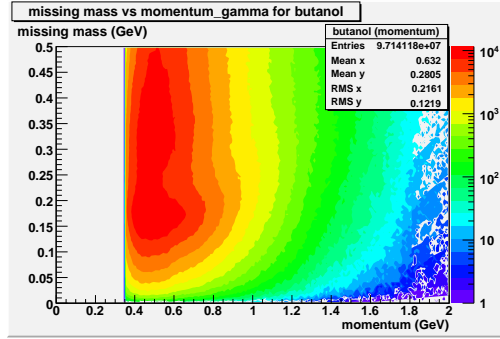


Figure 5.18: The vertices position of three targets, butanol, carbon, and polyethylene.

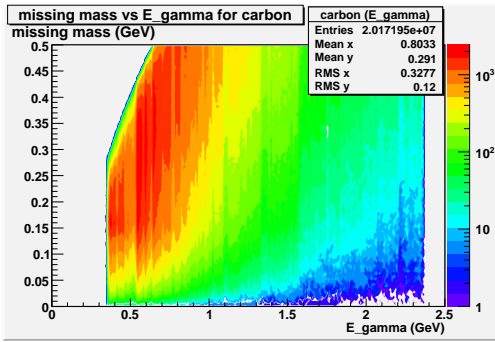
different targets were examined. The cross section depends on the number of the events for all helicity states for each target if the target is polarized. The helicity states $1/2$ and $3/2$, which were used here for all three targets, were those for the events for the butanol target since the carbon and the polyethylene targets were not polarized. Figure 5.20 (a) and (b) show the missing-mass distributions with different helicity states for the butanol target after the missing-mass squared cut. The histograms (c) and (e) show the missing-mass distributions for the carbon and polyethylene targets when the total helicity state for the butanol target is $1/2$, and (d) and (f) are those for the total helicity state $3/2$. To observe the difference between two helicity states clearly, the missing-mass distribution of the helicity state of $1/2$ was subtracted from that of the helicity state of $3/2$ for each target. Figure 5.21a shows the helicity difference (between helicity states $1/2$ and $3/2$ for the butanol target) vs. missing mass. As it was expected the histogram has a clear peak. On the other hand, as shown in Figure 5.21b and 5.21c any peaks are observed in their histograms of subtraction of the two different helicity states with carbon and polyethylene targets. The reasons for the vanishing asymmetry are (a) carbon



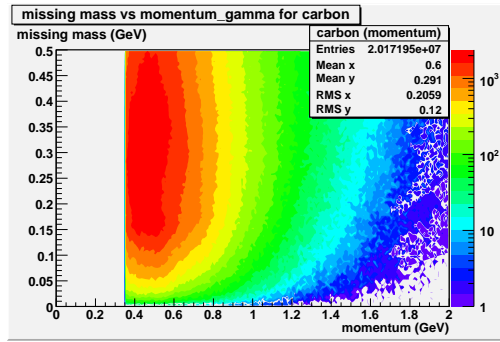
(a) missing mass vs. E_γ ; butanol



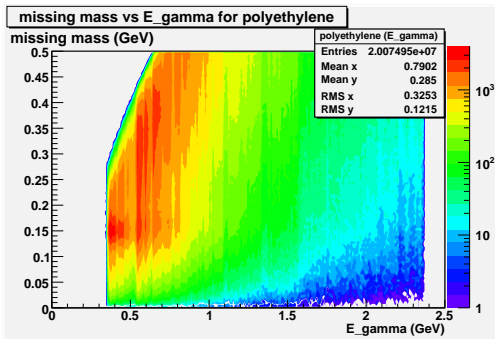
(b) missing mass vs. proton momentum; butanol



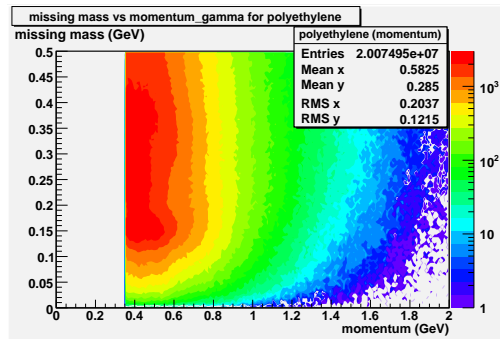
(c) missing mass vs. E_γ ; carbon



(d) missing mass vs. proton momentum; carbon

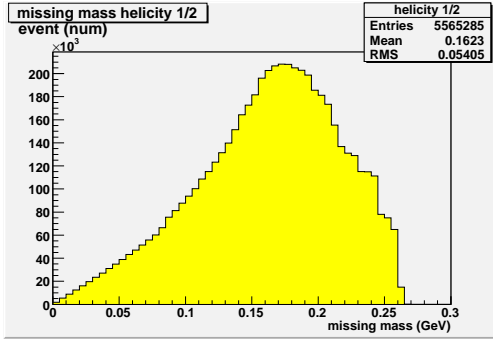


(e) missing mass vs. E_γ ; polyethylene

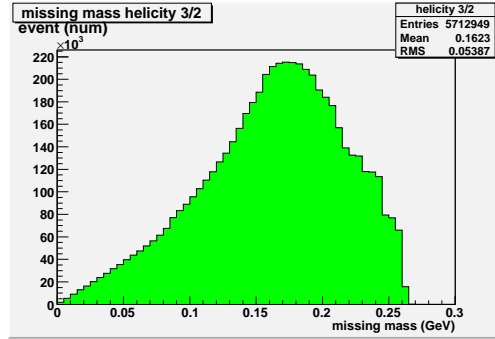


(f) missing mass vs. proton momentum; polyethylene

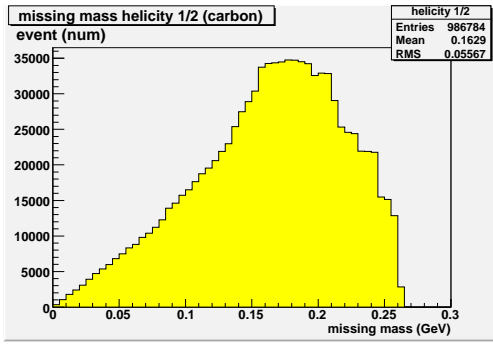
Figure 5.19: The missing-mass distributions by E_γ and by momentum of proton with three different targets, butanol, carbon, and polyethylene before the missing-mass squared cut.



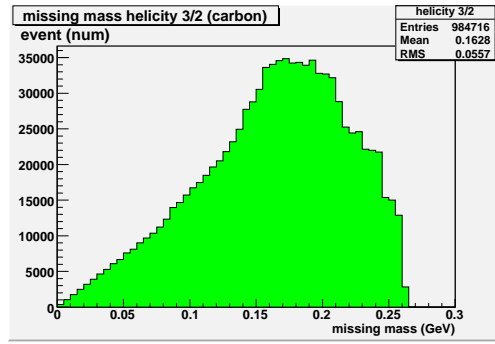
(a) butanol helicity 1/2



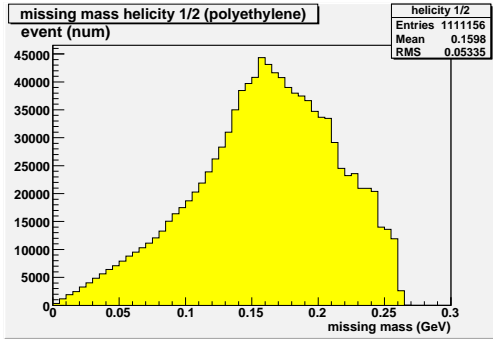
(b) butanol helicity 3/2



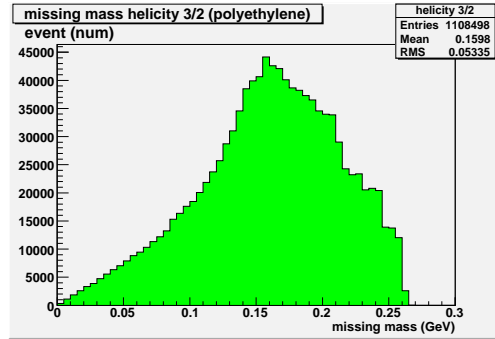
(c) carbon (butanol helicity 1/2)



(d) carbon (butanol helicity 3/2)

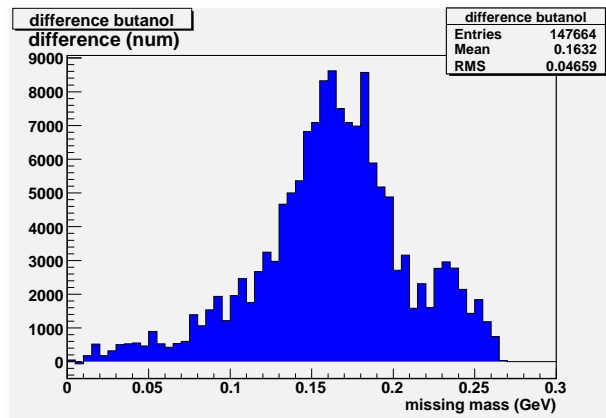


(e) polyethylene (butanol helicity 1/2)

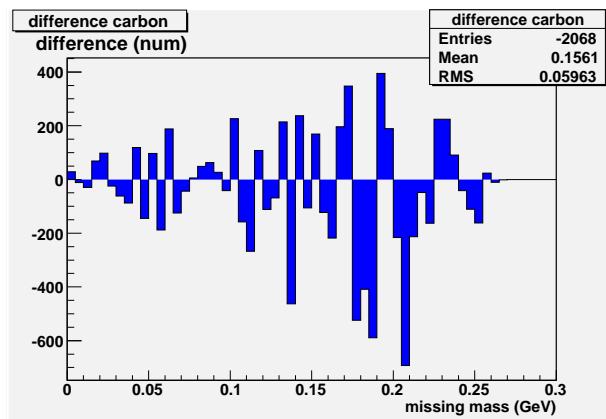


(f) polyethylene (butanol helicity 3/2)

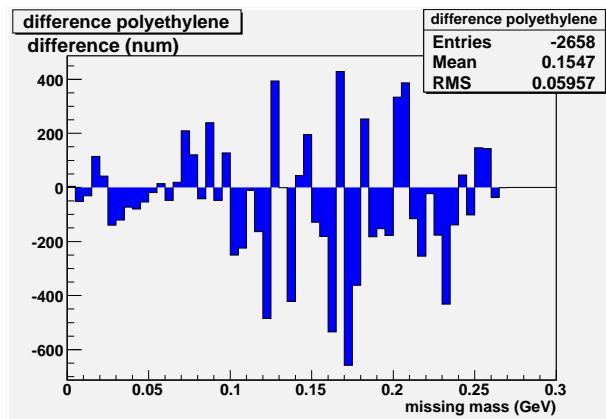
Figure 5.20: The missing-mass distributions different helicity states and different targets after the missing-mass squared cut. Since the carbon and the polyethylene targets were not polarized, (c) and (e) are the situation when total helicity state for the butanol target is 1/2, and (d) and (f) are helicity state 3/2.



(a) butanol difference



(b) carbon difference



(c) polyethylene difference

Figure 5.21: The helicity difference vs. missing mass:(a) butanol, (b) carbon, and (c) polyethylene targets after the missing-mass squared cut. Since carbon and polyethylene are not polarized, no significant differences are observed.

consists only of bound nucleons and (b) the polyethylene target was outside the range of the polarizing and holding magnets.

Chapter 6

Data Analysis 2: Helicity Asymmetry Extraction

In the FROST experiment, the butanol target, which contained carbon and oxygen, was used. As a result, a large number of bound nucleon reactions were observed. Since the free proton reactions can not be separated from the bound nucleon reactions, additionally a carbon target was used to get the event ratio of free protons to the total in the butanol target. The reactions from the carbon target were assumed to have similar distribution patterns with respect to different angles and energies to those of bound nucleons in the butanol target.

The event ratio of the bound nucleon in the butanol target to the carbon target is defined by the “scale” factor (see section 6.3.1). The scale factor was used to obtain the ratio of the free proton events to the total events by the butanol target. This ratio is called “dilution” factor.

In this chapter, the final steps to extract the asymmetries using the scale and dilution factors are discussed.

6.1 Helicity asymmetry E

The helicity asymmetry E is written as

$$E = \frac{\sigma_{3/2} - \sigma_{1/2}}{\sigma_{3/2} + \sigma_{1/2}} = \frac{N_{\frac{3}{2}} - N_{\frac{1}{2}}}{N_{\frac{3}{2}} + N_{\frac{1}{2}}}, \quad (6.1)$$

where $\sigma_{3/2}$ and $\sigma_{1/2}$ are the cross sections for the total helicity states 3/2 and 1/2, respectively. For the observable E, the Eq. (3.13) reduces to:

$$\frac{d\sigma}{d\Omega} = \frac{d\sigma_0}{d\Omega} (1 - P_z P_{\odot} E). \quad (6.2)$$

Since the photon beam and the target were not 100 % polarized and the butanol target does not only contain free protons, Eq. (6.1) has to be modified to

$$E = \frac{1}{D_f \cdot P_\odot \cdot P_T} \left[\frac{\sigma_{3/2} - \sigma_{1/2}}{\sigma_{3/2} + \sigma_{1/2}} \right] = \frac{1}{D_f \cdot P_\odot \cdot P_T} \left[\frac{N_{\frac{3}{2}} - N_{\frac{1}{2}}}{N_{\frac{3}{2}} + N_{\frac{1}{2}}} \right], \quad (6.3)$$

where D_f^1 , P_\odot , and P_T are dilution factor, polarization of the photon and target polarization, respectively.

6.2 Run periods

The data with circularly polarized photon beams from the FROST experiment were divided into seven periods based on their total helicity. Runs within each period have the same conditions of electron beam energy, half-wave plate setting, and polarization direction of the butanol target.

Table 6.1 shows the polarization status of each run period. The direction of the polarization of the photon beam is determined by the polarization direction

¹The number of events of helicity 1/2 ($= N_{1/2}$) includes events of bound proton ($N_{b(1/2)}$) and free proton ($N_{f(1/2)}$):

$$N_{1/2} = N_{b(1/2)} + N_{f(1/2)}. \quad (6.4)$$

Similarly, for helicity 3/2:

$$N_{3/2} = N_{b(3/2)} + N_{f(3/2)}. \quad (6.5)$$

Thus:

$$\begin{aligned} N_{3/2} - N_{1/2} &= (N_{b(3/2)} + N_{f(3/2)}) - (N_{b(1/2)} + N_{f(1/2)}) = (N_{f(3/2)} - N_{f(1/2)}) + (N_{b(3/2)} - N_{b(1/2)}) \\ &\simeq (N_{f(3/2)} - N_{f(1/2)}). \end{aligned} \quad (6.6)$$

Since the direction of the polarization of the electron beam was flipped at 30 Hz, we can assume the number of events of bound nucleon $N_{b(1/2)}$ and $N_{b(3/2)}$ are almost same. Therefore, the asymmetry E becomes:

$$\begin{aligned} E &= \frac{1}{D_f \cdot P_\odot \cdot P_T} \frac{\sigma_{3/2} - \sigma_{1/2}}{\sigma_{3/2} + \sigma_{1/2}} \simeq \left[\frac{1}{D_f} \frac{N_{f(\frac{3}{2})} - N_{f(\frac{1}{2})}}{(N_{f(\frac{3}{2})} + N_{f(\frac{1}{2})}) + (N_{b(\frac{3}{2})} + N_{b(\frac{1}{2})})} \right] \times \frac{1}{P_\odot \cdot P_T} \\ &\simeq \frac{1}{D_f \cdot P_\odot \cdot P_T} \times \frac{N_{f(\frac{3}{2})} - N_{f(\frac{1}{2})}}{N_{f(\frac{3}{2})} + N_{f(\frac{1}{2})}}. \end{aligned} \quad (6.7)$$

To reduce the number of reaction in the denominator to only the free proton reaction, the multiplication by the dilution factor is necessary.

Period	Run number	Beam energy (GeV)	Beam pol. sign	Half-wave plate	Target pol. (%)	overall sign
1	55521-55536	1.645	-	+	$\Leftarrow (+)$	-
2	55537-55555	1.645	-	-	$\Leftarrow (+)$	+
3	55556-55595	1.645	-	+	$\Rightarrow (-)$	+
4	55604-55625	2.478	+	+	$\Leftarrow (+)$	+
5	55630-55678	2.478	+	+	$\Rightarrow (-)$	-
6	56164-56193	2.478	+	+	$\Rightarrow (-)$	-
7	56196-56233	2.478	+	+	$\Leftarrow (+)$	+

Table 6.1: The polarization status of each run period. Beam denotes the the electron beam. The last column shows periods with same overall helicity.

of the linearly polarized electron beam and the half-wave plate (in or out). Periods 1, 5, and 6 have the same overall helicity states, and periods 2, 3, 4, and 7 have the same overall helicity states.

6.3 Extraction of asymmetry E

The two values, P_{\odot} and P_T , out of three in front of the asymmetry equation, Eq. 6.3 were mentioned in the previous sections 3.5.2 and 3.5.3. During the experiment, the average polarization of the primary electron beam was about 83.5 %, and the polarization of the photon beam was determined by the Eq. 3.25. The polarization of the frozen spin target was 78 % \sim 92 %.

In order to extract the asymmetry E for the $\gamma p \rightarrow \pi^0 p$ reaction, it is necessary to determine the effective dilution factor D_f , which is the ratio of the free proton reactions to the bound nucleon reactions in the butanol target. To determine the dilution factor, a scale factor must be known.

The scale factor will be studied in the next section.

6.3.1 Scale factor

We assume that (1) the bound nucleon was not polarized during the polarization process nor inside the holding magnet. It means we assume that only the free protons of the butanol target were polarized. We also think that (2)

the energy dependent yield is the same for the bound nucleons of butanol and that of carbon, so, we multiply the events from the carbon target by a certain number and use those as events from bound nucleons in the butanol target. This number is called a “scale factor”. It is very important to get the correct value of the scale factor because it eventually determines the number of events coming from free protons.

Since the bound nucleon has Fermi motion, the recoil proton from the bound nucleon occasionally has bigger four momentum than that from free proton, which is at rest. This Fermi motion causes the negative missing-mass squared in Figure 6.1. Thus, the events with the negative missing-mass squared are

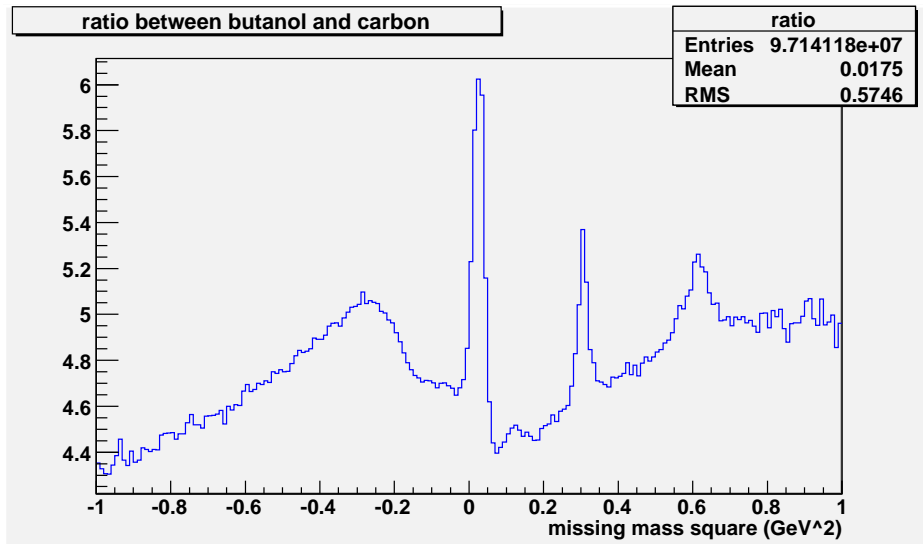
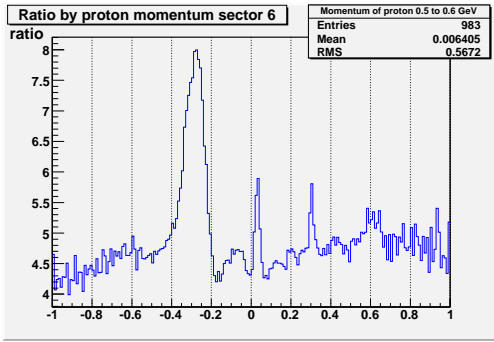
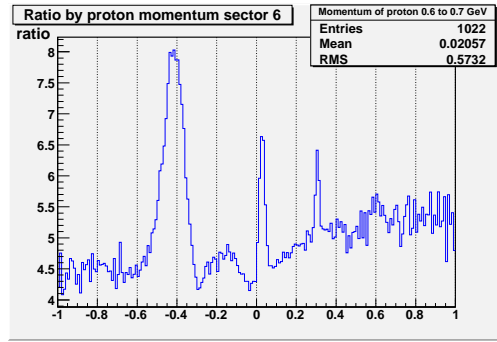


Figure 6.1: The figure shows the ratio of events from butanol and from carbon targets. There is a peak in the negative missing-mass squared around -0.3 GeV^2 .

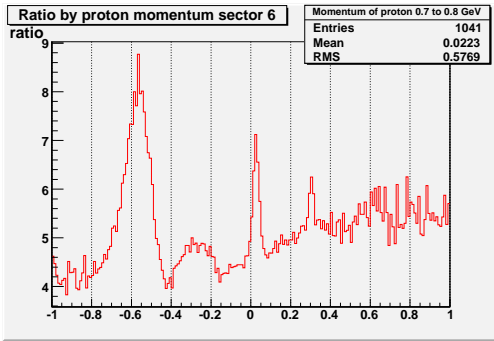
thought to be produced on bound nucleons with Fermi motion. If the ratio of number of events from the butanol target and the carbon target in the region of the negative missing-mass squared were stable, we could use it as a scale factor. Unfortunately, as seen in Figure 6.1 the ratio in the negative missing-mass squared is not stable and there is a bump and non-zero slope. Especially in the region of the negative missing-mass squared for events with protons in sector 6, there is a big peak, which depends on the proton momentum as shown in Figure 6.2. One of the reasons why the ratio is not stable is that there is



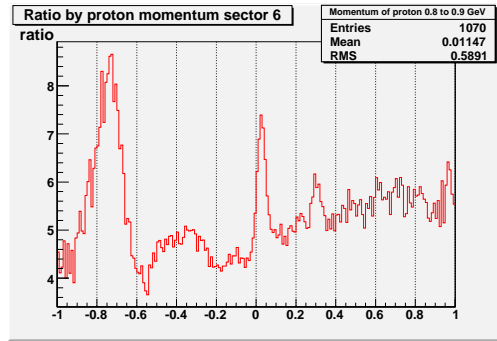
(a) momentum 0.5 ~ 0.6 GeV



(b) momentum 0.6 ~ 0.7 GeV



(c) momentum 0.7 ~ 0.8 GeV



(d) momentum 0.8 ~ 0.9 GeV

Figure 6.2: There is a big peak in the negative missing-mass squared for protons detected in sector 6.

more material between the butanol target and the start counter than between the carbon target and the start counter, and the total thickness of the materials (and also chemical compositions), which the recoil proton traverses differs by vertex position.

Because the scale factor and dilution factors depend on E_γ and proton momentum, two different types of scale and dilution factors, (1) based on E_γ and (2) based on proton momentum were tested (see Section 7.2.5). Since the scale and dilution factors depend on proton momentum more directly than E_γ those based on proton momentum were chosen. Since the ratio of the events from butanol and from carbon targets is not stable in the negative missing-mass squared region, the range between $-0.2 \sim 0.0 \text{ GeV}^2/c^2$ was basically chosen, which is close to the peak of π^0 , to determine the scale factors as seen in Figure 6.3. As a result, eighteen different scale factors [three different scales by proton momentum (a) $0.3 \sim 0.5 \text{ GeV}$, (b) $0.5 \sim 1.0 \text{ GeV}$, and (c) $1.0 \sim 2.0 \text{ GeV}$ for each sector] were used.

6.3.2 Dilution factor

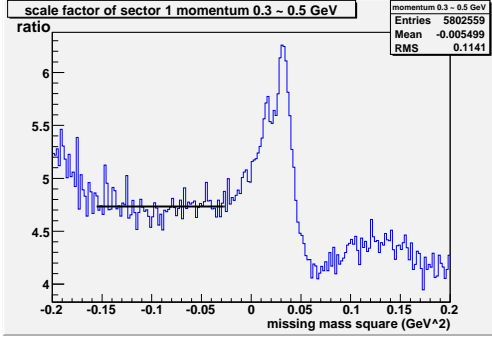
One of the important aspects to consider in the evaluation of the helicity asymmetry is the dilution factor D_f . The background arises mainly from bound nucleon reactions inside the target and from reactions with surrounding material. To determine these conditions, additional measurements on a carbon target were performed. The events from the carbon target were scaled and were used to determine the dilution factor.

The butanol target, which refers to the isometric alcohol of formula C_4H_9OH , does not consist of a pure hydrogen target but includes bound nucleons, C and O . The butanol target has a density of 0.61 g/cm^3 (butanol beads in ${}^3\text{He}/{}^4\text{He}$ bath²). In order to determine the dilution factor D_f , a carbon target ($\rho = 2.26 \text{ g/cm}^3$) of 15 mm length was used and was fixed at 6.15 cm downstream from the butanol target (Table 5.2).

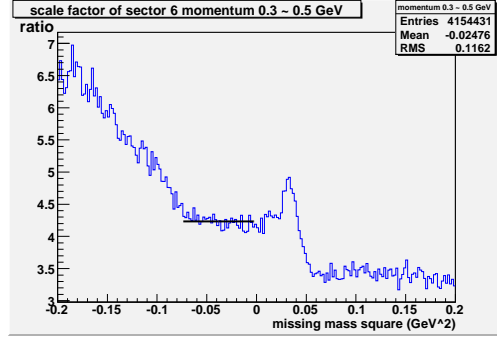
The dilution factor is defined applying the scale factor [95]

$$D_f = \frac{B_f}{B_{tot}} = \frac{B_{tot} - B_{bound}}{B_{tot}} \simeq \frac{B_{tot} - C \times S_f}{B_{tot}}, \quad (6.8)$$

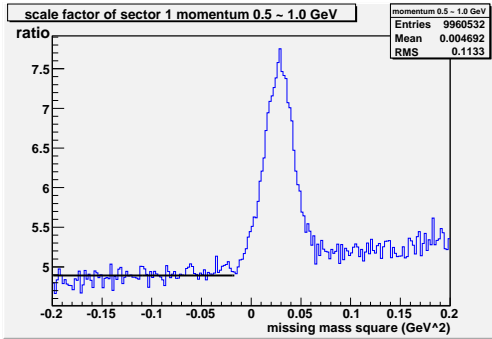
²A solid block of butanol has density 0.985 g/cm^3 .



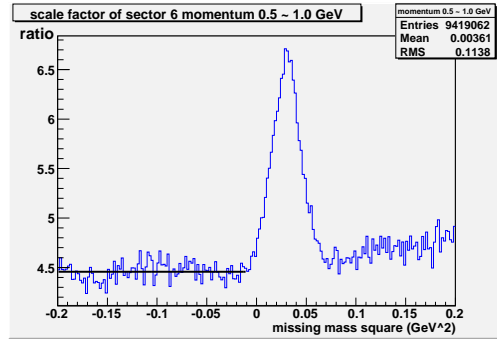
(a) sector 1 momentum 0.3 ~ 0.5 GeV



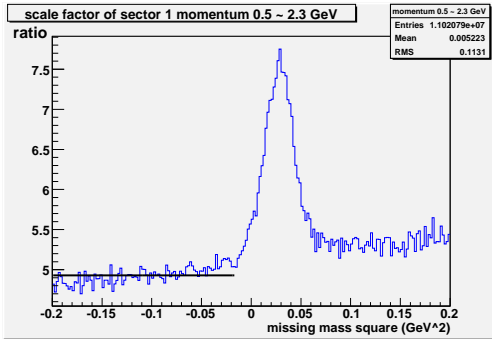
(b) sector 6 momentum 0.3 ~ 0.5 GeV



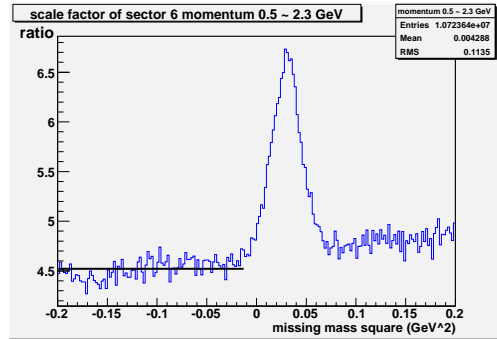
(c) sector 1 momentum 0.5 ~ 1.0 GeV



(d) sector 6 momentum 0.5 ~ 1.0 GeV



(e) sector 1 momentum 0.5 ~ 2.3 GeV



(f) sector 6 momentum 0.5 ~ 2.3 GeV

Figure 6.3: The scale factors were determined by the ratio of butanol and carbon events with the range between $-0.2 \sim 0.0 \text{ GeV}^2$ of the missing-mass squared. They depend on sector (or azimuthal angle ϕ) and proton momentum. The figures show some of the scale factors from sectors 1 and 6.

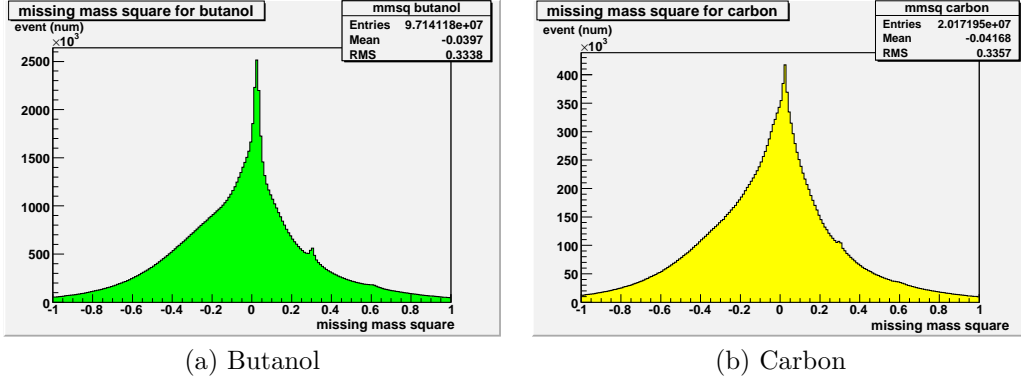


Figure 6.4: The negative missing-mass squared produced on butanol and carbon targets.

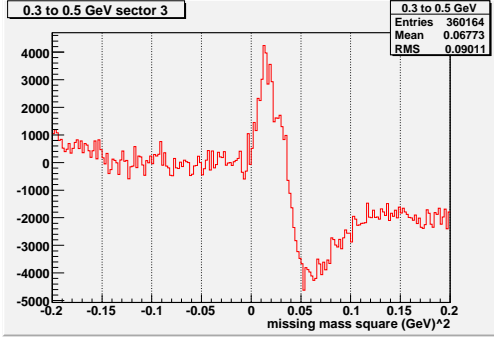
where B_f , B_{tot} , B_{bound} , C , and S_f , are the number of events from free protons in butanol, those from any nucleon in butanol, those from bound nucleons in butanol, those from any nucleon in carbon, and the scale factor, respectively. The low limit of this dilution factor is obtained by a simple calculation:

$$D_f(\text{low limit}) = \frac{(\text{free hydrogen in butanol})}{(\text{total nucleon in butanol})} = \frac{10}{74} \simeq 0.135. \quad (6.9)$$

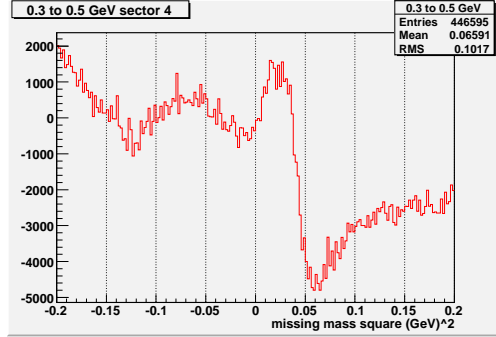
Figure 6.4 shows some of the missing-mass squared distribution obtained from butanol and the carbon targets. The number of events coming from free nucleons in the butanol target corresponds to the subtraction of the scaled carbon events from the butanol events. Figure 6.5 shows the π^0 peaks by sector.

The Figure 6.6 shows the comparison before and after applying the scale factor to the events with the carbon target. In the channel of $\gamma p \rightarrow \pi^0 p$, the value of the dilution factor was obtained by a fifth-order polynomial depending on the proton momentum (Figure 6.7). The statistical error of the dilution factor was calculated by the error propagation equation

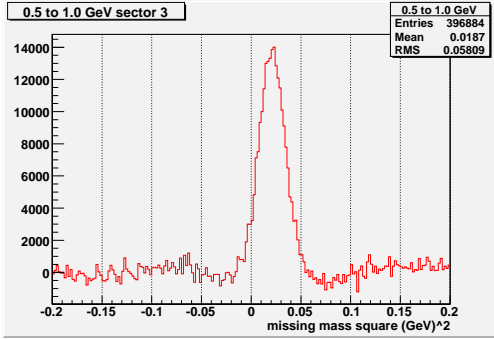
$$\sigma_x^2 \simeq \underbrace{\sigma_u^2 \left(\frac{\partial x}{\partial u}\right)^2 + \sigma_\nu^2 \left(\frac{\partial x}{\partial \nu}\right)^2 + \dots}_{\text{uncorrelated terms}} + \underbrace{2\sigma_{u\nu}^2 \left(\frac{\partial x}{\partial u}\right) \left(\frac{\partial x}{\partial \nu}\right) + \dots}_{\text{correlated terms}} \quad (6.10)$$



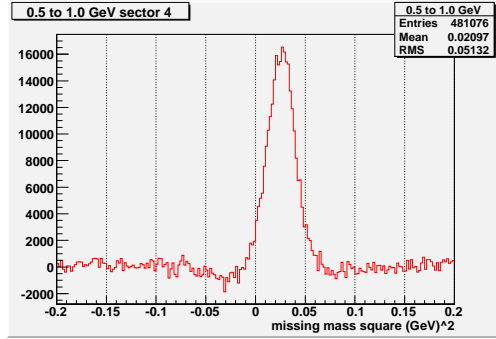
(a) sector 3 momentum 0.3 ~ 0.5 GeV



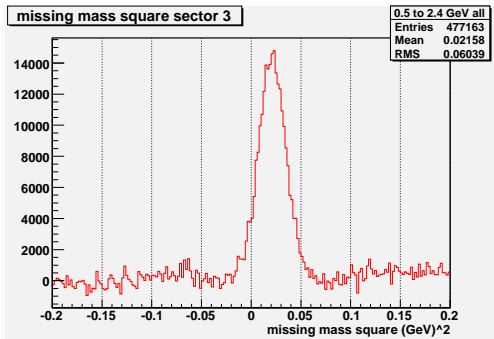
(b) sector 4 momentum 0.3 ~ 0.5 GeV



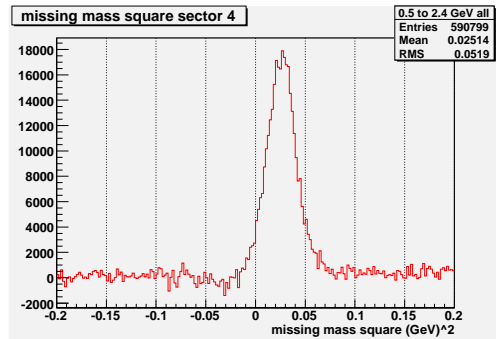
(c) sector 3 momentum 0.5 ~ 1.0 GeV



(d) sector 4 momentum 0.5 ~ 1.0 GeV



(e) sector 3 momentum 1.0 ~ 2.3 GeV



(f) sector 4 momentum 1.0 ~ 2.3 GeV

Figure 6.5: The missing-mass squared for different sectors with different proton momentum.

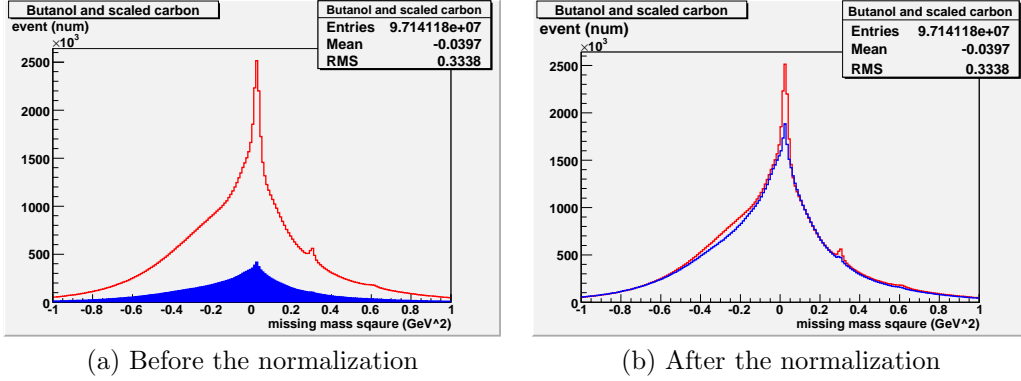


Figure 6.6: Application of norm factor to the number of events with carbon target, (a) before, and (b) after.

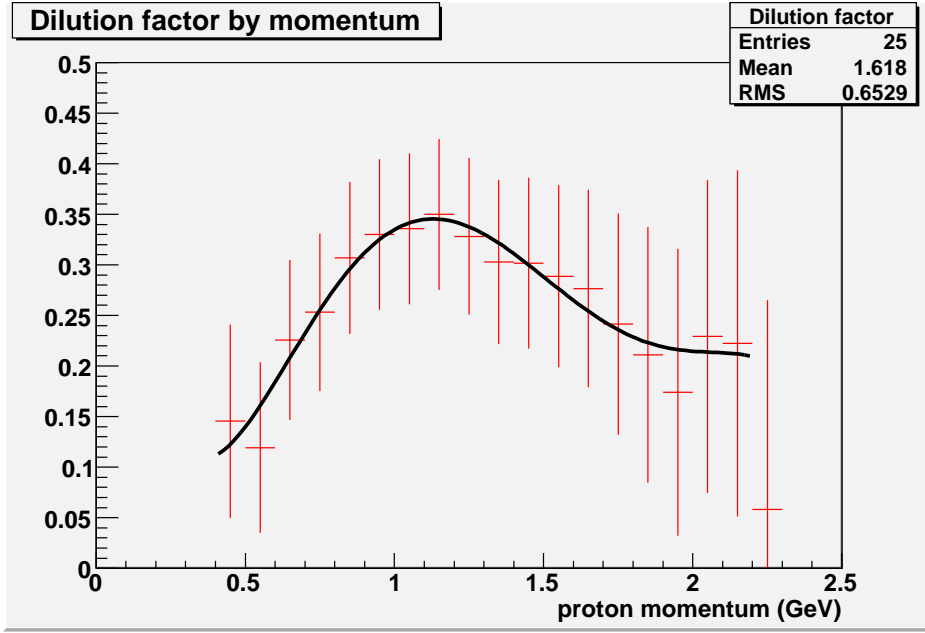


Figure 6.7: The dilution factor (curved line), which depends on proton momentum, is obtained with a fifth-order polynomial.

together with Eq. (6.8):

$$\begin{aligned}
 \sigma_{dilute}^2 &= \sigma_C^2 \left(\frac{\partial D_f}{\partial C} \right)^2 + \sigma_{S_f}^2 \left(\frac{\partial D_f}{\partial S_f} \right)^2 + \sigma_{B_{tot}}^2 \left(\frac{\partial D_f}{\partial B} \right)^2 \\
 &= \frac{C \times S_f^2}{B_{tot}^3} (B_{tot} + C) + \sigma_{S_f}^2 \left(\frac{C}{B_{tot}} \right)^2
 \end{aligned} \tag{6.11}$$

where σ_{dilute} , σ_{S_f} , $\sigma_{B_{tot}} (= \sqrt{B_{tot}})$, and $\sigma_C (= \sqrt{C})$ are statistical errors of dilution factor, scale factor, event number of butanol, and event number of carbon, respectively.

Chapter 7

Statistical and systematic uncertainties

The errors, (1) statistical uncertainties and (2) systematic errors for the $\gamma p \rightarrow \pi^0 p$ channel in this experiment are estimated.

7.1 Statistical uncertainties

For the calculation of the statistical uncertainties, the error propagation equation [Eq. (6.10)] is used [96]:

$$\sigma_x^2 \simeq \underbrace{\sigma_u^2 \left(\frac{\partial x}{\partial u}\right)^2 + \sigma_\nu^2 \left(\frac{\partial x}{\partial \nu}\right)^2 + \dots}_{\text{uncorrelated terms}} + \underbrace{2\sigma_{uv}^2 \left(\frac{\partial x}{\partial u}\right) \left(\frac{\partial x}{\partial \nu}\right) + \dots}_{\text{correlated terms}} \quad (7.1)$$

If the functions in the measured quantities u, ν, \dots are uncorrelated, the correlated terms are expected to vanish. Thus, the reasonable approximation is

$$\sigma_x^2 \simeq \sum \sigma_i^2 \left(\frac{\partial x}{\partial i}\right)^2, \quad (7.2)$$

where i is measured variable of x , such as polarizations of beam and target.

For the helicity asymmetry E ,

$$E = \frac{1}{D_f P_\odot P_T} \frac{N_{3/2} - N_{1/2}}{N_{3/2} + N_{1/2}} \equiv f(D_f, P_\odot, P_T, N_{3/2}, N_{1/2}), \quad (7.3)$$

where $N_{1/2}$ and $N_{3/2}$ are the event numbers for helicity states $\frac{1}{2}$ and $\frac{3}{2}$, respectively, and f is the function whose parameters are $D_f, P_\odot, P_T, N_{1/2}$, and $N_{3/2}$.

Since

$$\begin{aligned}
\frac{\partial f}{\partial D_f} &= \left(\frac{-1}{D_f}\right) \cdot f, & \frac{\partial f}{\partial P_\odot} &= \left(\frac{-1}{P_\odot}\right) \cdot f, & \frac{\partial f}{\partial P_T} &= \left(\frac{-1}{P_T}\right) \cdot f, \\
\frac{\partial f}{\partial N_{1/2}} &= \left[\frac{(-2)N_{3/2}}{N_{tot}^2}\right] \cdot \left(\frac{1}{D_f P_\odot P_T}\right), \\
\frac{\partial f}{\partial N_{3/2}} &= \left(\frac{2N_{1/2}}{N_{tot}^2}\right) \cdot \left(\frac{1}{D_f P_\odot P_T}\right),
\end{aligned} \tag{7.4}$$

where $N_{tot} \equiv N_{1/2} + N_{3/2}$. The square of the standard deviation σ_E for asymmetry E is

$$\begin{aligned}
\sigma_E^2 &= \sigma_{D_f}^2 \left(\frac{\partial f}{\partial D_f}\right)^2 + \sigma_{P_\odot}^2 \left(\frac{\partial f}{\partial P_\odot}\right)^2 + \sigma_{P_T}^2 \left(\frac{\partial f}{\partial P_T}\right)^2 \\
&\quad + \sigma_{N_{1/2}}^2 \left(\frac{\partial f}{\partial N_{1/2}}\right)^2 + \sigma_{N_{3/2}}^2 \left(\frac{\partial f}{\partial N_{3/2}}\right)^2 \\
&= \left[\left(\frac{\sigma_{D_f}}{D_f}\right)^2 + \left(\frac{\sigma_{P_\odot}}{P_\odot}\right)^2 + \left(\frac{\sigma_{P_T}}{P_T}\right)^2 \right] \cdot f^2 + \left(\frac{1}{D_f P_\odot P_T}\right)^2 \frac{4}{N_{tot}^3} N_{1/2} N_{3/2} \\
&= f^2 \cdot \left[\left(\frac{\sigma_{D_f}}{D_f}\right)^2 + \left(\frac{\sigma_{P_\odot}}{P_\odot}\right)^2 + \left(\frac{\sigma_{P_T}}{P_T}\right)^2 + \frac{4N_{1/2}N_{3/2}}{N_{tot}(N_{3/2} - N_{1/2})^2} \right],
\end{aligned} \tag{7.5}$$

where $\sigma_{N_{1/2}} = \sqrt{N_{1/2}}$ and $\sigma_{N_{3/2}} = \sqrt{N_{3/2}}$ are used.

7.1.1 Weighting average of the data

The experiment for the observable E had seven periods (see Section 6.2) which have different. To combine all data or get the most probable value of asymmetry E , the formula of weighted average of the data points [96]

$$\mu' = \frac{\sum(x_i/\sigma_i^2)}{\sum(1/\sigma_i^2)}, \tag{7.6}$$

is used where μ' , x_i , and σ_i are weighted average each data point, and variance of x_i , respectively. Also, error in the weighted mean is

$$\sigma_\mu^2 = \frac{1}{\sum(1/\sigma_i^2)}. \tag{7.7}$$

7.1.2 Electron beam polarization

The polarization of electron beam during the experiment is listed in Table 3.6. The statistical uncertainties of the electron beam polarization was measured by the Møller measurements. The uncertainties was calculated by averaging these values. The statistical uncertainty of the beam polarization is about 1.39 %.

7.1.3 Target polarization

The statistical uncertainty of the target polarization is estimated with the table of target polarization of g9a in Reference [97], which is run-by-run based. It is the average of these run-by-run based values. The statistical uncertainty is 5.4×10^{-1} %.

7.1.4 Result

Table 7.1 shows the statistical uncertainties.

uncertainty	value
Electron beam polarization	1.39 %
Target polarization	5.4×10^{-1} %
Asymmetry	± 0.05

Table 7.1: Statistical uncertainties are shown. The statistical uncertainties of the electron beam and the target polarizations are estimated by averaging run-by-run based values.

7.2 Systematic uncertainties

In addition to the statistical uncertainties, which are rigorously calculated according to the formalism, there are systematic errors resulting from uncertainties in measured quantities. Systematic errors, which make a result different from the final values with reproducible discrepancies, are estimated for (1)

target polarization, (2) fiducial cuts, (3) π^0 mass cut (missing-mass squared cut), (4) z-vertex cut, and (5) scale and dilution factors.

The calculation of the systematic errors requires identifying potential sources of uncertainty. The altered numerical values are applied for each cut or factor to measure the differences of the resultant asymmetries. Thus, the systematic error due to a particular source can be estimated measuring differences between the two asymmetry results.

The asymmetry with $\Delta E_\gamma = 50$ MeV and $\Delta \cos \theta = 0.1$ are used for estimating the systematic uncertainties. Since both lower and higher photon energy bins have large statistical uncertainties, the total number of asymmetry points are limited with the energy range of $550 \text{ MeV} \leq E_\gamma \leq 1600 \text{ MeV}$. About 380 points are used. The distribution of the differences between the measured asymmetries with nominal and altered cut is given in a histogram. The root-mean square (rms) of this distribution is considered as a measure of the systematic uncertainty due to the cut under study. The systematic errors due to above sources are calculated in this manner except for the target and electron beam polarizations. The sources and magnitudes of these systematic uncertainties are given in the following subsections.

7.2.1 Target polarization

The systematic uncertainty due to the target polarization is estimated using a table in Reference[97], which is run by run based. It is the average of these run by run based values. Systematic uncertainty of the target polarization is about $1.6 \times 10^{-1} \%$.

7.2.2 Fiducial cut

As mentioned in Section 5.2.3, the fiducial cuts is applied to remove events coming from the inefficient regions of CLAS. After the nominal fiducial cuts, only the following events are considered for further investigation if

- (1) either $\theta \geq 40^\circ$ and
 $-25^\circ \leq \phi \leq +25^\circ$ (sector 1), $+35^\circ \leq \phi \leq +85^\circ$ (sector 2), $+95^\circ \leq \phi \leq +145^\circ$ (sector 3),
 $+155^\circ \leq \phi \leq +180^\circ$, or $-180^\circ \leq \phi \leq -155^\circ$ (sector 4), $-145^\circ \leq \phi \leq -95^\circ$ (sector 5),

$-85^\circ \leq \phi \leq -35^\circ$ (sector 6),
(2) or $9^\circ \leq \theta \leq 40^\circ$ and

$$\phi \leq 25.0^\circ \times \left[\frac{\theta - 9.0}{40.0 - 9.0} \right]^{0.25}. \quad (7.8)$$

To evaluate the systematic error of the fiducial cuts, the values of both (1) and (2) above were changed. For (1), 0.5 degree a tighter cut for each edges, for example, $-24.5^\circ \leq \phi \leq +24.5^\circ$ (sector 1) is used. For (2), an equation for the tighter cut is used:

$$\phi \leq 25.0^\circ \times \left[\frac{\theta - 9.0}{40.0 - 9.0} \right]^{0.24}. \quad (7.9)$$

The result of distributions is in Figure 7.1 , and the $\sigma \simeq 2.5 \%$.

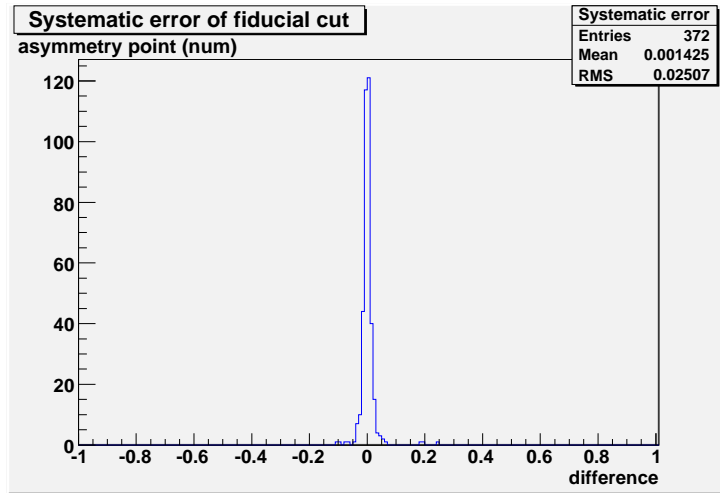


Figure 7.1: The systematic error by the fiducial cut.

7.2.3 Missing-mass squared cut

The nominal missing-mass squared cut was applied by using the mean value of π^0 peak for each sector $\pm 3\sigma$. To estimate the systematic uncertainty of this cut, the value was changed from $\pm 3\sigma$ to $\pm 2\sigma$. The Figure 7.2 shows the uncertainty of the missing mass square cut is 9.6 %.

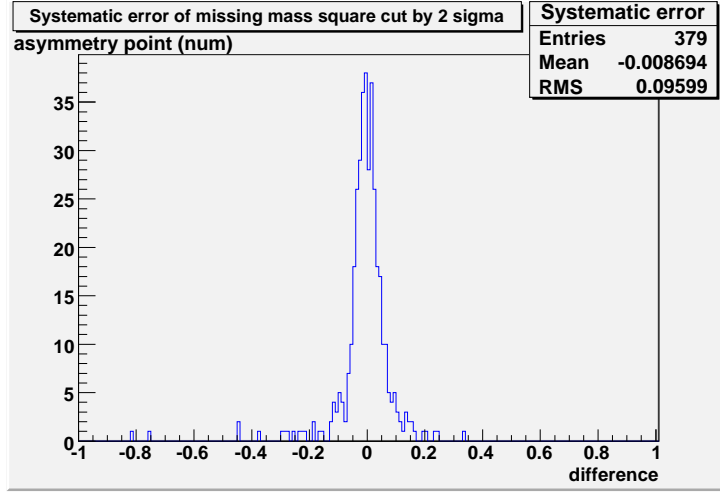


Figure 7.2: The systematic error of missing-mass squared cut. The cut values are changed from (mean value $\pm 3\sigma$) to (mean value $\pm 2.0\sigma$).

7.2.4 z-vertex cut

The nominal z-vertex cut for the butanol target was applied from -2.75 cm to +2.75 cm. To find the systematic uncertainty for the z-vertex cut, the maximum value was changed from +2.75 to +2.00, since the downstream mixing chamber had been filled with $^3\text{He}/^4\text{He}$, but not the upstream part. The results are shown in Figure 7.3. The uncertainty is about 10.9 %.

7.2.5 Scale and dilution factor

The estimated systematic uncertainties of the scale and dilution factors are discussed in this section.

Following conditions are with the nominal values:

(a) the scale factors were determined using the range of $-1.0 \text{ GeV}^2 \sim 0.0 \text{ GeV}^2$ of the negative missing-mass square.

(b) There are eighteen different scale factors and they depend on proton momentum and the sectors.

(c) The dilution factor depends only on proton momentum, but not on the sectors.

The systematic uncertainties are estimated for three different cases in this section. Some or all of the conditions, (a) \sim (c) are changed in the following

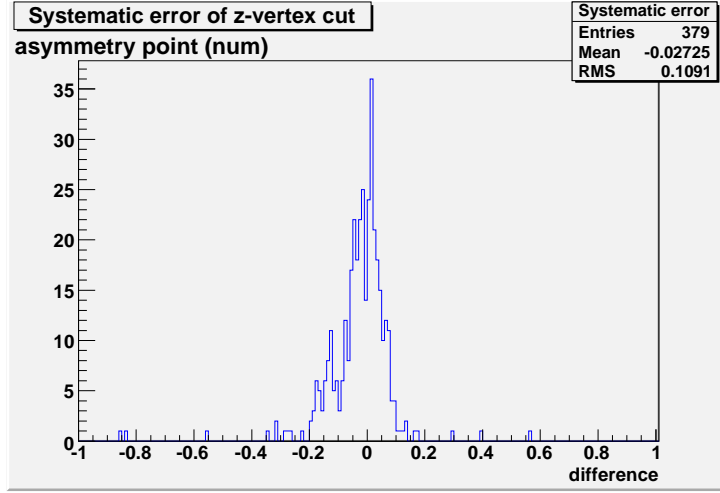


Figure 7.3: The systematic error of z-vertex changing the range of the vertex cut to $-2.75 \text{ cm} \sim +2.00 \text{ cm}$.

case 1 \sim 3.

7.2.5.1 Case 1

The range of the missing-mass square was chosen from -1.0 GeV^2 to 0.0 GeV^2 and the total number of scale factors were increased to more than twenty. The dilution factor, as shown in Figure 7.4, depends on proton momentum, which is the same as the nominal case. Other conditions are the same as the nominal case. As seen in Figure 7.5, some values of asymmetry E are out of range, ± 1 , especially at lower E_γ and forward angles. They also have bigger sizes of statistical uncertainties compared with those of nominal values. The majority of the values, that are different from the nominal value by 20 %, are at low E_γ and forward angles. Figure 7.6 shows the statistical uncertainty is about 17.8 %.

7.2.5.2 Case 2

In the case 2, the scale and dilution factors depend on E_γ , but not proton momentum. The range of the negative missing-mass square was chosen between -1.0 and -0.6 GeV^2 , omitting a peak around -0.3 GeV^2 as seen in Figure 7.7.

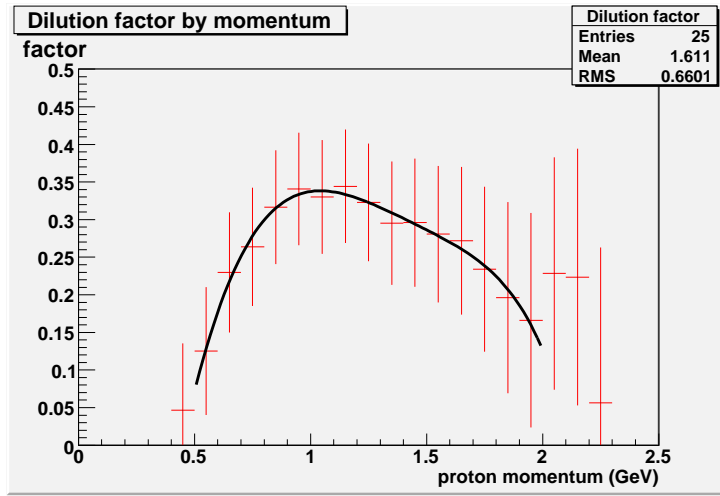


Figure 7.4: The dilution factor. Only one dilution factor with 30 different scale factors was used.

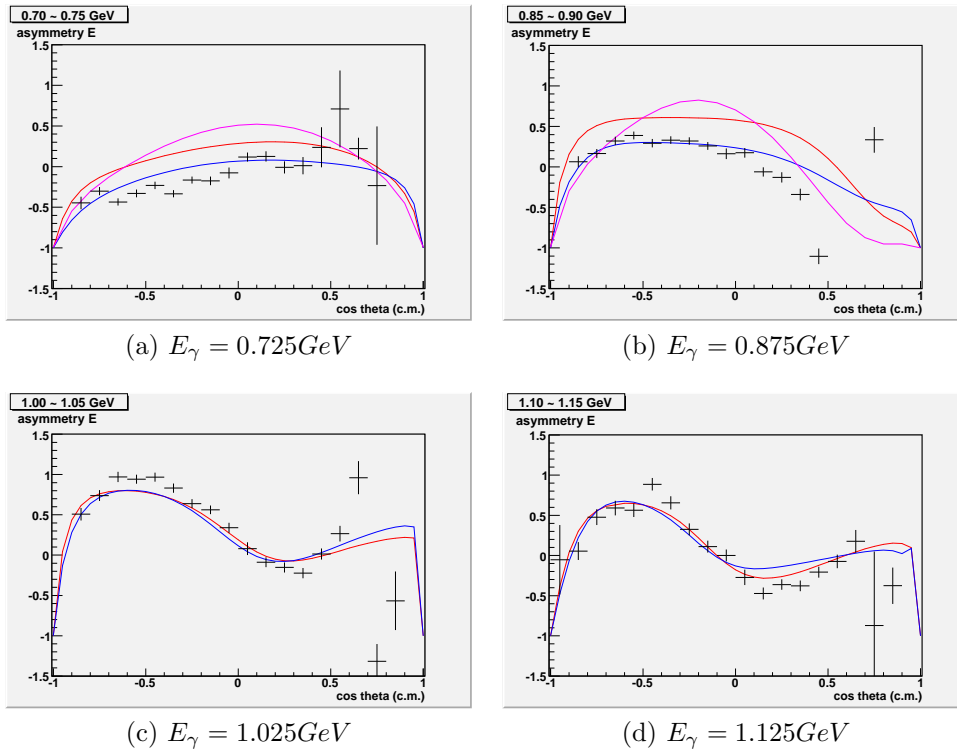


Figure 7.5: Some of the points of asymmetry E are missing in the forward angles.

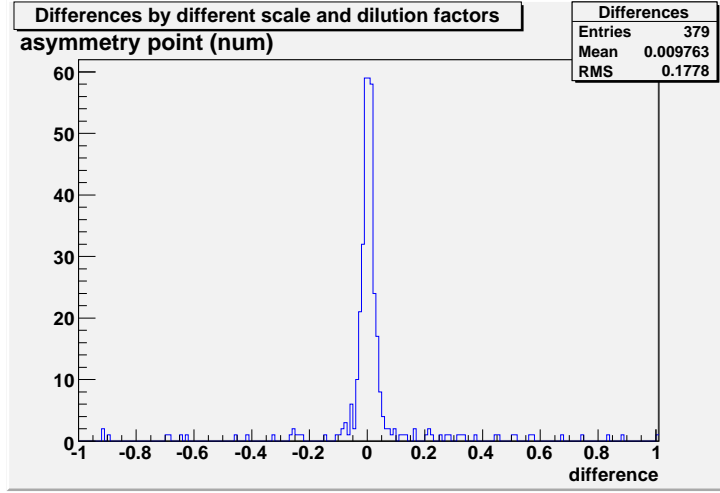


Figure 7.6: The difference using 24 different scale factors, which depends on the proton momentum and sector (angle ϕ), and one dilution factor, which depends on the proton momentum.

This is the simplest case of all since only 6 different scale factors, one for each sector, and only one dilution factor are used. Figure 7.8 shows a dilution factor, which is used to get asymmetry points of E . The dilution factor based on E_γ does not look smooth compared with the one that is based on proton momentum. As shown in Figure 7.9 the difference is around 13.6 %.

7.2.5.3 Case 3

The scale factors were basically determined for the range of $-0.2 \sim 0.0$ GeV^2 of the negative missing-mass square, and depend on E_γ and the sectors, but not on proton momentum. The dilution factors depend on both E_γ and the sectors. The case 3 is similar to case 2, but the number of scale and dilution factors are increased. Figure 7.10 shows six different dilution factors, which are used. The uncertainty in the case 3 is about 17.1 % as seen in Figure 7.11.

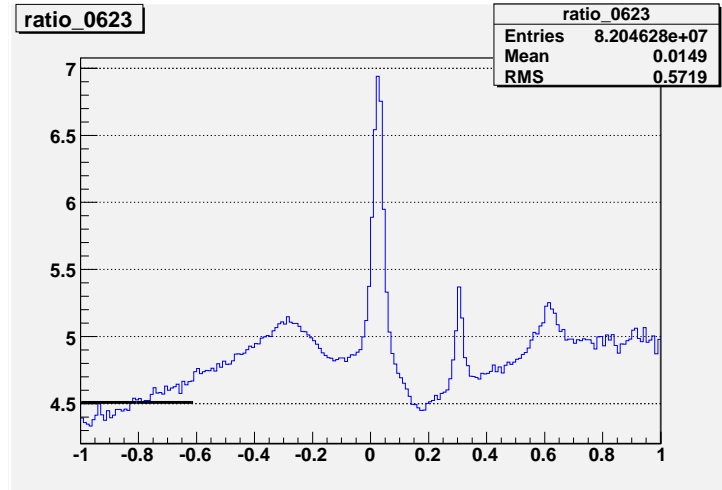


Figure 7.7: The range between -1.0 and -0.6 GeV^2 , where the effect of the peak around -0.3 GeV^2 was smaller, was chosen to get a scale factor.

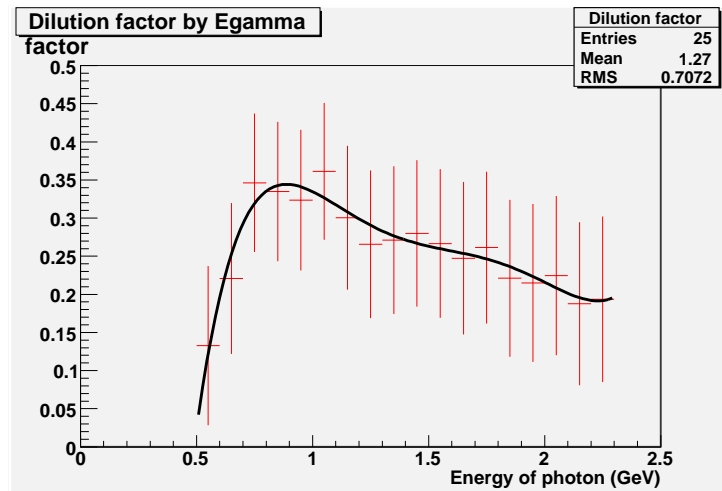


Figure 7.8: The dilution factor which is based on E_γ and is used in case 2.

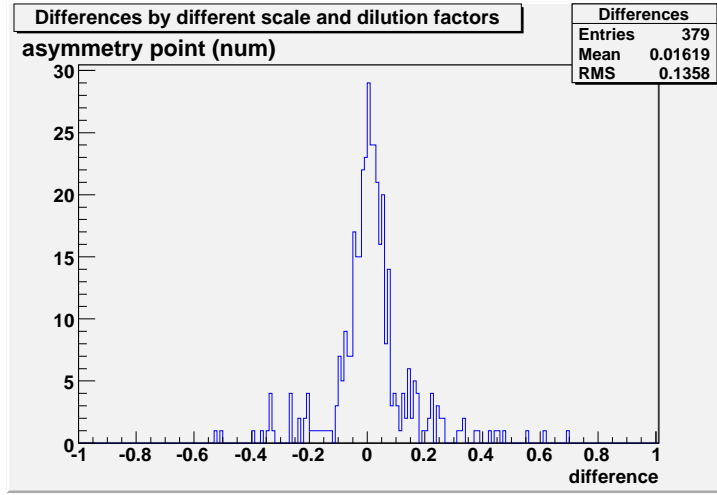
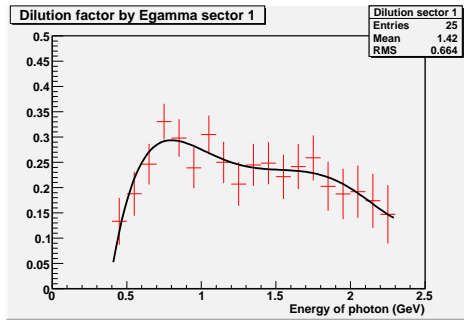


Figure 7.9: The figure shows the difference using one scale and one dilution factors, which depends on E_γ .

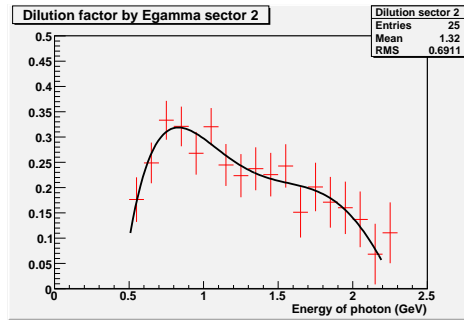
7.2.6 Result

The biggest systematic uncertainty is the scale and dilution factors, which are more than 13 %. Since these scale and dilution factors have large uncertainties, it is very important to get correct values for the final result, asymmetry E. The smallest value except the electron beam charge asymmetry is the target polarization, about 8.4×10^{-2} %.

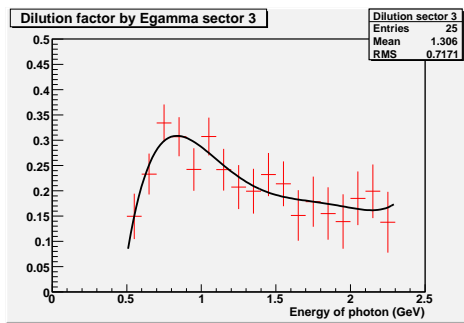
All systematic errors being estimated in this section are listed in Table 7.2.



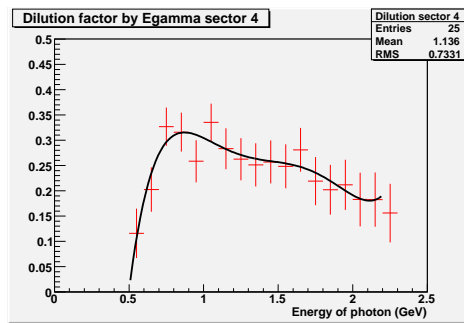
(a) sector 1



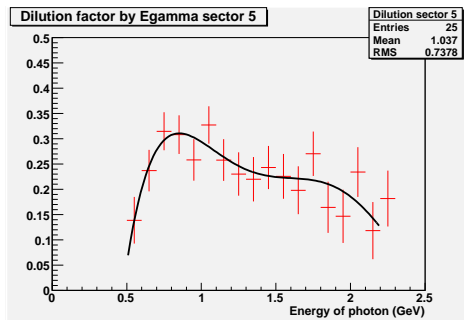
(b) sector 2



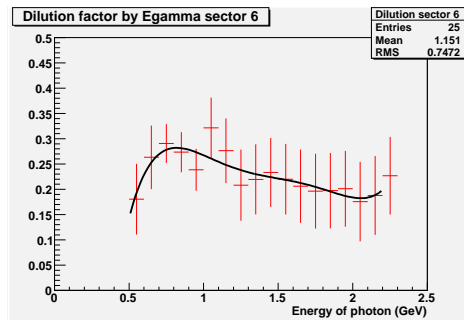
(c) sector 3



(d) sector 4



(e) sector 5



(f) sector 6

Figure 7.10: The dilution factors by sector.

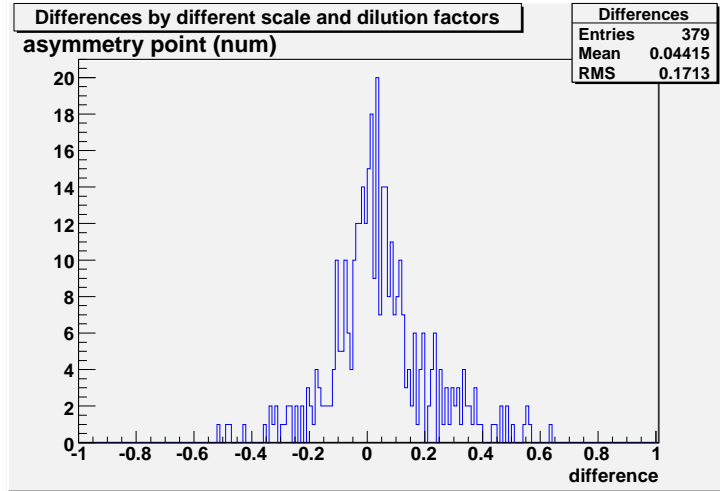


Figure 7.11: The difference using 18 different scale factors, which depends on E_γ and sector (angle ϕ), and 6 different dilution factors for each sector.

Table 7.2: Systematic errors

uncertainty	value
Electron beam conditions:	
Energy of beam	$\approx 0.1 \%$
Tagger resolution	$> 0.1 \%$
Beam polarization	$\approx 2 \%$
Beam charge asymmetry (positive helicity vs negative helicity)	$6 \times 10^{-2} \%$
Target polarization	$1.6 \times 10^{-1} \%$
Fiducial cut	2.5%
Missing-mass squared cut	9.6%
Scale and dilution factor	
case (1)	17.8%
case (2)	13.6%
case (3)	17.1%

Chapter 8

Result/Discussion

First, the quantity and quality of events will be discussed in this section. Events for the analysis are chosen with some cuts (Chapter 5) and are used for the final results, asymmetry E . Next, these results are compared with the three theoretical predictions and other experimental data. Finally, the result of the analysis is discussed.

8.1 Events and polarizations for $\pi^0 p$ channel

The peak of the cross section of $p\gamma \rightarrow \pi N$ production is at $E_\gamma \simeq 360$ MeV, which is equivalent to $W \simeq 1250$ MeV (See Figure 1.3).

Period	Event number	(%)	E_γ	Subtotal	(%)
1	$15,499 \times 10^3$	(9.2)	1.645 GeV		
2	$19,084 \times 10^3$	(11.3)	1.645 GeV		
3	$39,660 \times 10^3$	(23.6)	1.645 GeV	$74,243 \times 10^3$	(44.1)
4	$13,389 \times 10^3$	(8.0)	2.478 GeV		
5	$35,180 \times 10^3$	(20.9)	2.478 GeV		
6	$23,548 \times 10^3$	(14.0)	2.478 GeV		
7	$21,862 \times 10^3$	(13.0)	2.478 GeV	$93,979 \times 10^3$	(55.9)
Total	$168,223 \times 10^3$	(100.0)		$168,223 \times 10^3$	(100.0)

Table 8.1: The number of events in each period after one proton per event is chosen.

Table 8.1 shows the number of events of each period after one proton per event was chosen. The ratio of events with $E_{\text{electron}} = 1.645$ GeV to those with $E_{\text{electron}} = 2.478$ GeV is about 4:5. But, after choosing π^0 as a missing particle

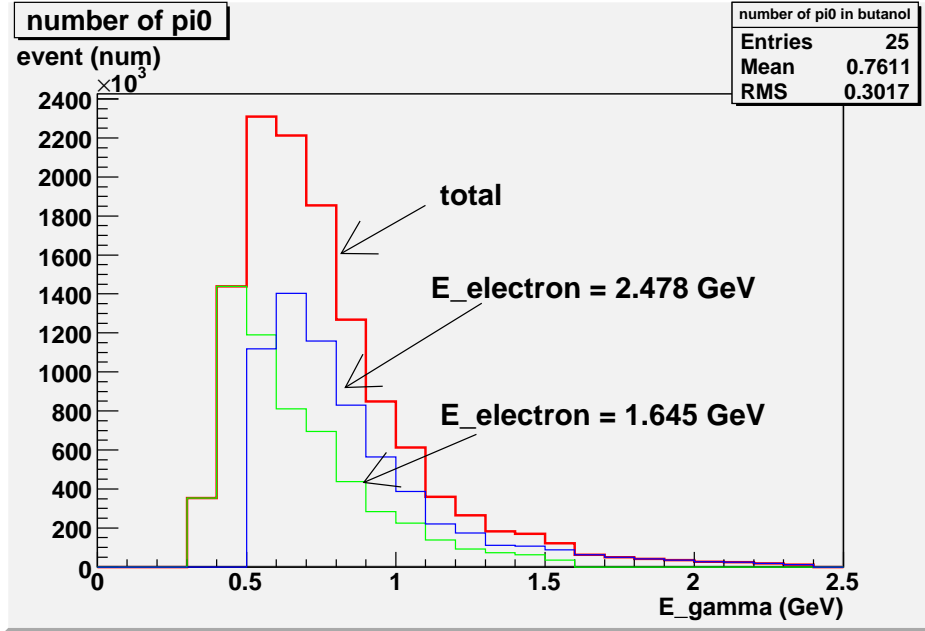


Figure 8.1: The number of events (a) group 1 ~ 3 (green line), (b) group 4 ~ 7 (blue line), and (c) All groups (red line) with different E_γ .

scattered from the butanol target, this ratio changes to 1:1 (Table 8.2). The reason is that energies multi-pion and other particle reactions become more likely at higher.

Figure 8.1 shows the number of events with butanol target by different E_γ ; (a) the green line denotes group 1 ~ 3 ($E_\gamma = 1.645$ GeV), (b) the blue line denotes group 4 ~ 7 ($E_\gamma = 2.478$ GeV), and (c) the red line the total. It is clearly seen that the majority of the events are around $E_\gamma = 0.40 \sim 1.10$ GeV.

Table 8.2 and Table 8.3 also show the distribution of events for the channel $p\gamma \rightarrow \pi^0 p$ by photon energy. Events at $0.50 \text{ GeV} \leq E_\gamma \leq 1.10 \text{ GeV}$ are about 76 % of the total. During the FROST experiment, we used two different energies of electron beams, $E_{\text{electron}} = 1.645$ GeV and $E_{\text{electron}} = 2.478$ GeV. They were too high to produce the high polarizations of the photon beam for the single pion photoproduction because the polarization of photon depends on the ratio $E_\gamma/E_{\text{electron}}$ as seen in Figure 3.1.

The polarization of the photon beams for these events at $0.50 \text{ GeV} \leq E_\gamma \leq 0.9 \text{ GeV}$ are $34.8\% \leq P_\odot \leq 68.3\%$ for group 1 ~ 3 ($E_{\text{electron}} = 1.645$ GeV) and

$21.9\% \leq P_{\odot} \leq 45.3\%$ for group 4 \sim 7 ($E_{\text{electron}} = 2.478$ GeV).

The beam polarization of the majority of events is less than 68 %. And there are less events with high photon polarization. Since the factor of the asymmetry E is $1/(D_f \cdot P_{\odot} \cdot P_{\gamma})$, this low polarization of the photon beam affects the size of the statistical error dramatically.

8.2 Result of measured asymmetry E

Each event has different energy of E_{γ} , different polarizations of beam and target, and different dilution factor. Thus, the asymmetry E is calculated with run-by-run based polarizations of beam and target, and with the fifth-order polynomial for the dilution factor depending on proton momentum. These events are distributed into bins of the different photon energy E_{γ} and $\cos \theta_{\text{c.m.}}^{\pi^0}$.

Since the number of events drops dramatically by E_{γ} , different bin sizes are used.

(1) For $550 \leq E_{\gamma} \leq 1600$ MeV

The bin size of E_{γ} is 50 MeV and that of $\cos \theta_{\text{c.m.}}^{\pi^0}$ is 0.1. [$\Delta E_{\gamma} = 50$ MeV and $\Delta \cos \theta_{\text{c.m.}}^{\pi^0} = 0.1$] (Figure 8.2 \sim Figure 8.5(c)).

(2) For $1600 \leq E_{\gamma} \leq 2300$ MeV

The bin size of E_{γ} is 100 MeV and that of $\cos \theta_{\text{c.m.}}^{\pi^0}$ is 0.1. [$\Delta E_{\gamma} = 100$ MeV and $\Delta \cos \theta_{\text{c.m.}}^{\pi^0} = 0.1$] (Figure 8.5(d) \sim 8.6).

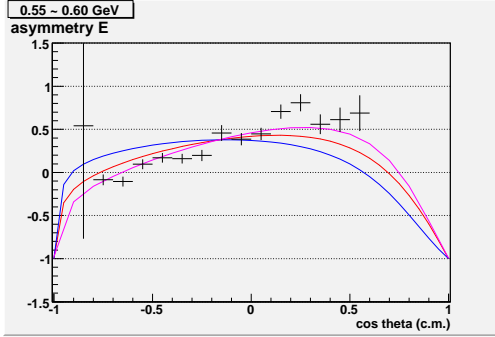
Measured asymmetry E are compared with three different theoretical predictions, SAID(blue line), MAID(red line), and EBAC(pink line).

Additionally, asymmetry histograms are produced:

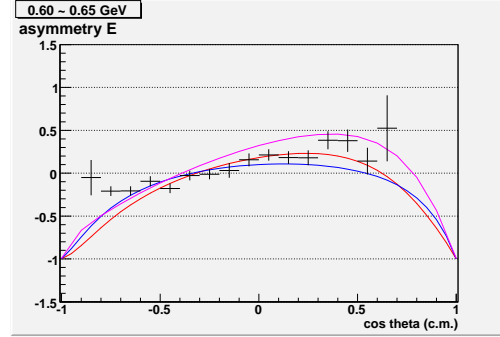
(a) for different center of energies W and bins in $\cos \theta_{\text{c.m.}}^{\pi}$, whose bin size of W is 20 MeV and those of $\cos \theta_{\text{c.m.}}^{\pi^0}$ is 0.1 [(Figure 8.7 \sim Figure 8.11, $\Delta W = 20$ MeV, 1.42 GeV $\leq W \leq 2.0$ GeV, $\cos \theta_{\text{c.m.}}^{\pi^0} = 0.1$)],

(b) for comparison between $E_{\text{electron}} = 1.645$ GeV and $E_{\text{electron}} = 2.478$ GeV [(Figure 8.13 \sim Figure 8.16, $\Delta E_{\gamma} = 100$ MeV, 500 MeV $\leq E_{\gamma} \leq 1600$ MeV, $\cos \theta_{\text{c.m.}}^{\pi} = 0.1$)].

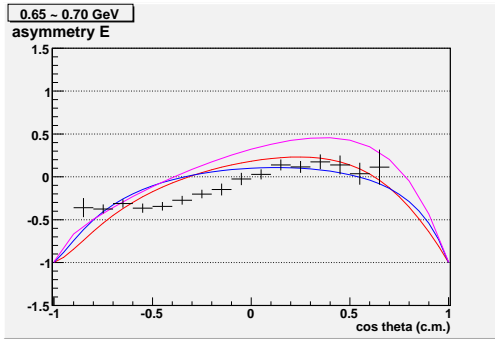
The variation of the asymmetry E with photon energy E_{γ} (Figure 8.17 \sim 8.23) for different $\cos \theta_{\text{c.m.}}^{\pi^0}$ bins ($\Delta \cos \theta_{\text{c.m.}}^{\pi^0} = 0.1$) are also shown.



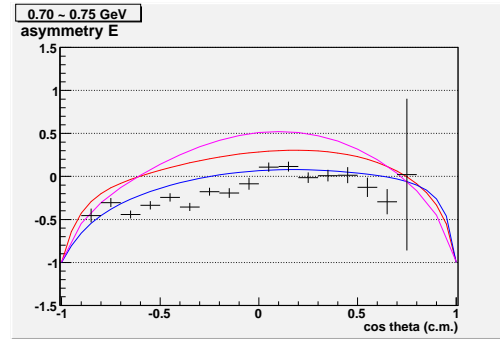
(a) $E_\gamma = 575$ MeV



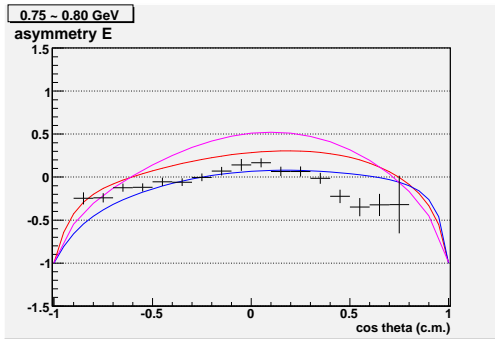
(b) $E_\gamma = 625$ MeV



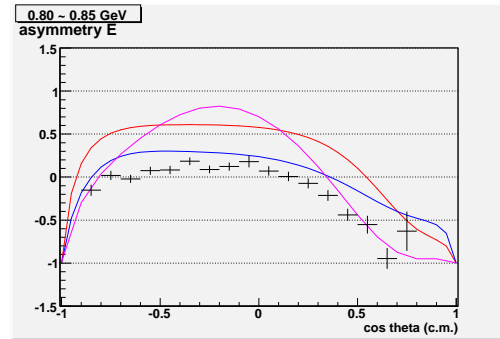
(c) $E_\gamma = 675$ MeV



(d) $E_\gamma = 725$ MeV

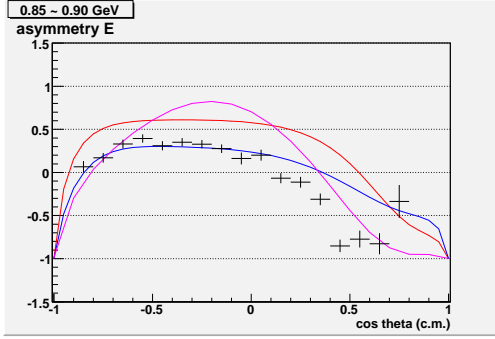


(e) $E_\gamma = 775$ MeV

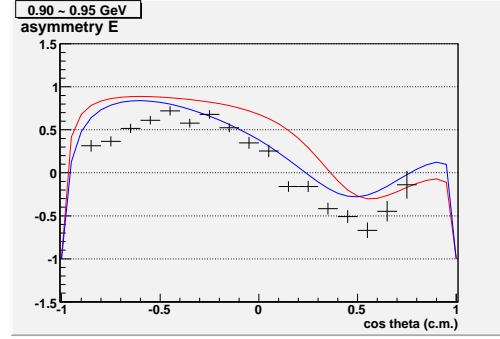


(f) $E_\gamma = 825$ MeV

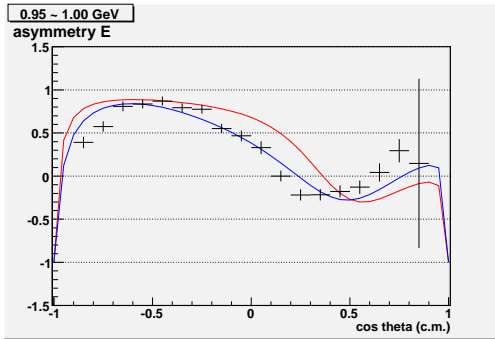
Figure 8.2: The figures show asymmetry E for all groups ($E_{\text{electron}} = 1.645$ GeV and 2.478 GeV) in the different E_γ comparing with the three theoretical predictions, SAID2009 (blue line), MAID2007 (red line), and EBAC (pink line).



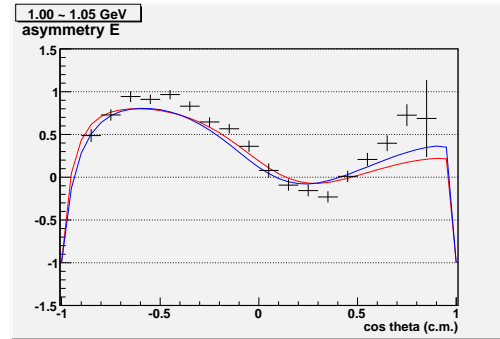
(a) $E_\gamma = 875$ MeV



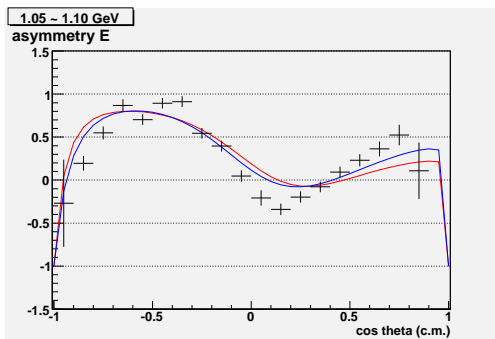
(b) $E_\gamma = 925$ MeV



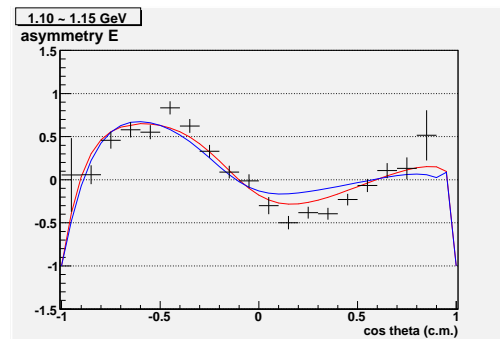
(c) $E_\gamma = 975$ MeV



(d) $E_\gamma = 1025$ MeV

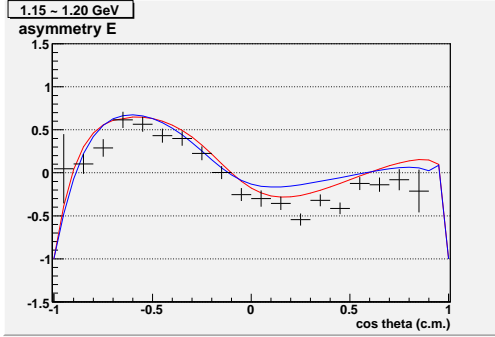


(e) $E_\gamma = 1075$ MeV

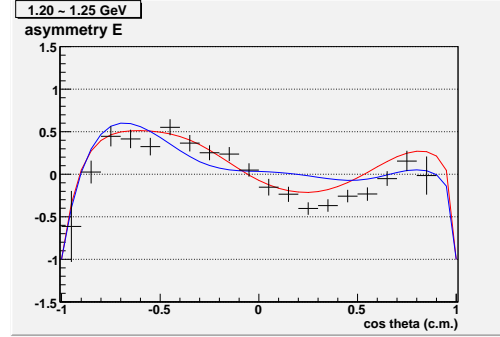


(f) $E_\gamma = 1125$ MeV

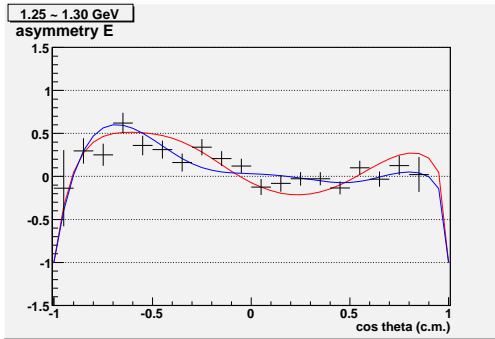
Figure 8.3: The figures show asymmetry E for all groups ($E_{\text{electron}} = 1.645$ GeV and 2.478 GeV) in the different E_γ comparing with the two theoretical predictions, SAID2009 (blue line), MAID2007 (red line), and EBAC (pink line).



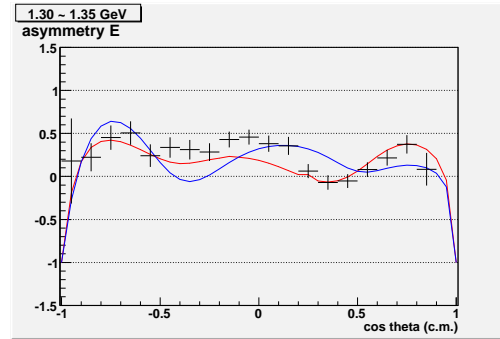
(a) $E_\gamma = 1175$ MeV



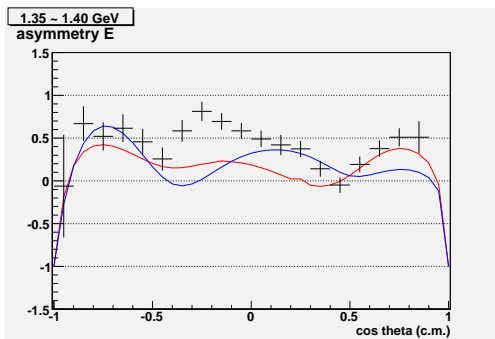
(b) $E_\gamma = 1225$ MeV



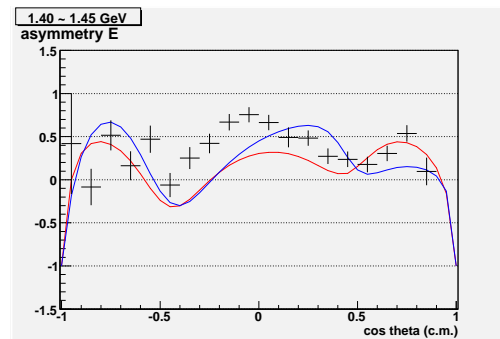
(c) $E_\gamma = 1275$ MeV



(d) $E_\gamma = 1325$ MeV



(e) $E_\gamma = 1375$ MeV



(f) $E_\gamma = 1425$ MeV

Figure 8.4: The figures show asymmetry E for all groups ($E_{\text{electron}} = 1.645$ GeV and 2.478 GeV) in the different E_γ comparing with the two theoretical predictions, SAID2009 (blue line) and MAID2007 (red line).

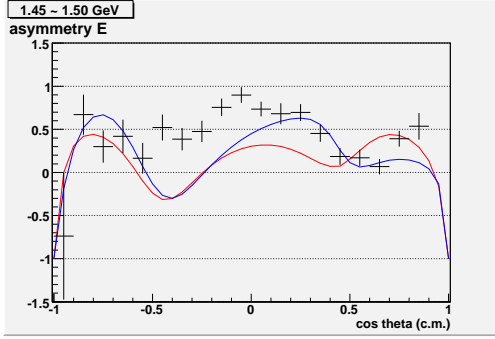
8.2.1 Comparison with the theoretical predictions

The helicity asymmetry E for $\gamma p \rightarrow \pi^0 p$ channel is measured as a function of pion scattering angle in the center-of-mass system, $\theta_{\text{c.m.}}^{\pi^0}$, in the photon energy region from 550 to 2400 MeV. The error bars shown in the figures represent only statistical uncertainties of asymmetry.

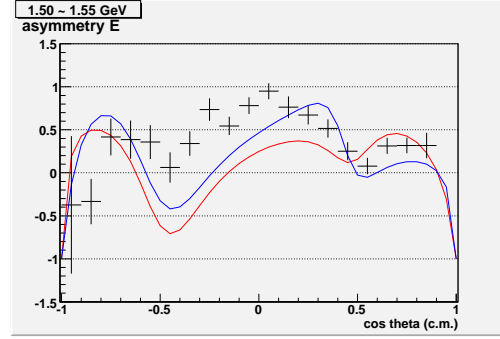
The results are compared to the available model calculations from SAID, MAID2007, and EBAC group (see chapter 2.4). SAID uses a parametrization method using huge data sets including single pion photoproduction data. Each partial wave is determined through PWA from these data. The MAID2007 model takes parameters from SAID. Therefore, their predictions of SAID and MAID2007 are similar at low W or E_γ . The EBAC group calculates self-energies without parametrization, and finds the location of the poles corresponding to the resonance masses. However, due to the difficulty of the calculations at higher resonances, their prediction is limited to the low photon energy region, up to $E_\gamma = 900$ MeV.

Even though the SAID calculations predict at higher photon energy region, it does not include double polarization data yet. More detailed information about partial waves or resonances can be obtained by including the recent double polarization data, which is very sensitive to various dynamical reaction effects. The $\pi^0 p$ channel, which is analyzed in this thesis, is one of the dominant channels for the partial waves of low energies. Thus, the SAID calculations incorporating this new information of helicity asymmetry will change significantly.

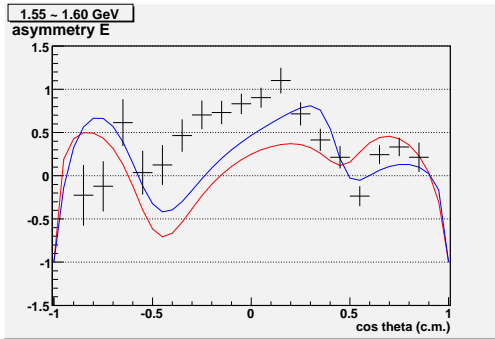
The result of asymmetry E has relatively large magnitude of error bars since the dilution factor is overall small especially at low proton momentum. As seen in Figure 6.6b the small value of the dilution factor comes from the fact that the π^0 peak is broad and the background (from bound proton reaction) is huge. Referring to Eq. (7.4) not only the small dilution factor, but also the low polarization of the photon beam contributes to the size of the uncertainties. Since the electron beams energy of $E_{\text{electron}} = 1.645$ and 2.478 GeV were used in the FROST experiment and the peak of the cross section for a single pion photoproduction is around 360 MeV of the photon beam energy, the polarization of the photon beam, which depends on the ratio (energy of photon / energy of electron), was not high for the majority of final events. For example, the polarization of the photon beam is $< 56\%$ at $E_\gamma = 900$ MeV, as



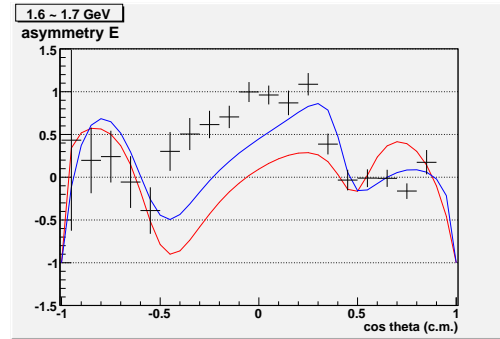
(a) $E_\gamma = 1475$ MeV



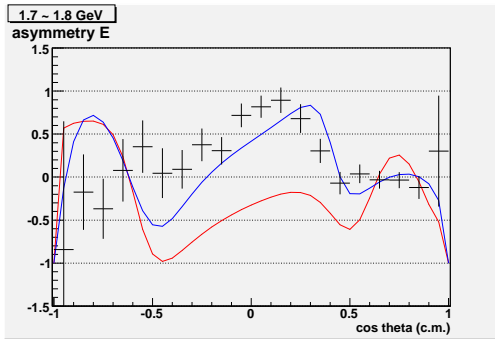
(b) $E_\gamma = 1525$ MeV



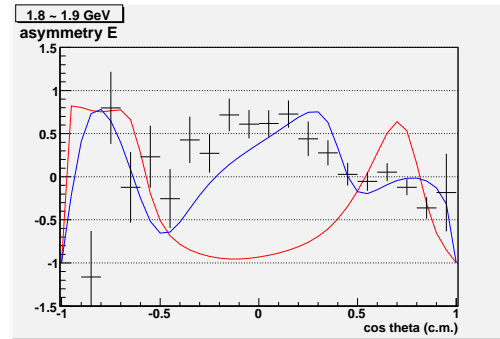
(c) $E_\gamma = 1575$ MeV



(d) $E_\gamma = 1650$ MeV

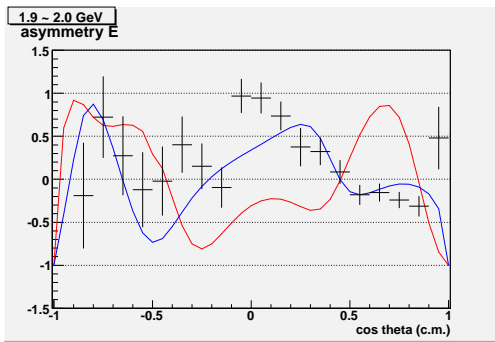


(e) $E_\gamma = 1750$ MeV

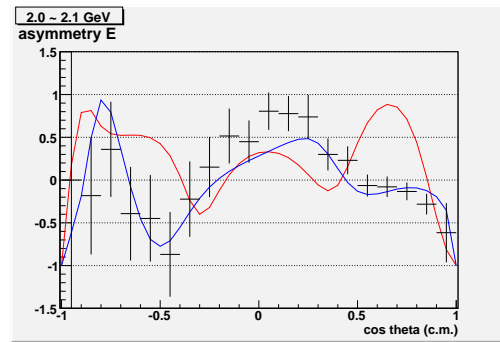


(f) $E_\gamma = 1850$ MeV

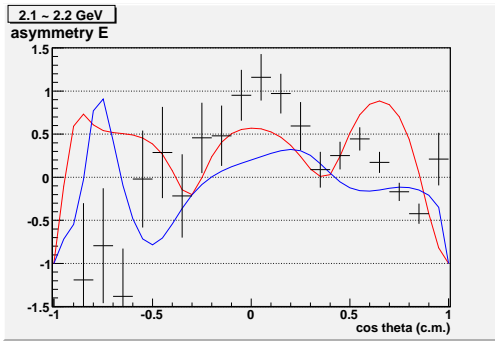
Figure 8.5: The figures show asymmetry E for all groups ($E_{\text{electron}} = 1.645$ GeV and 2.478 GeV) in the different E_γ comparing with the two theoretical predictions, SAID2009 (blue line) and MAID2007 (red line).



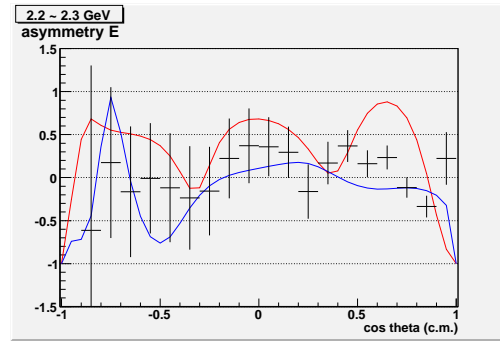
(a) $E_\gamma = 1950$ MeV



(b) $E_\gamma = 2050$ MeV

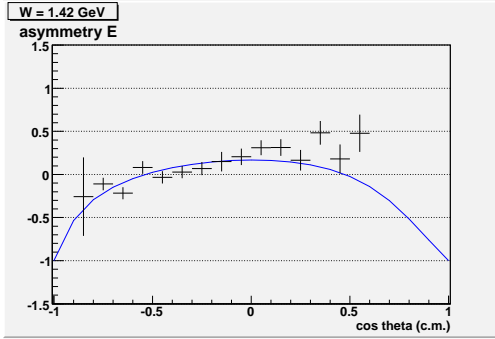


(c) $E_\gamma = 2150$ MeV

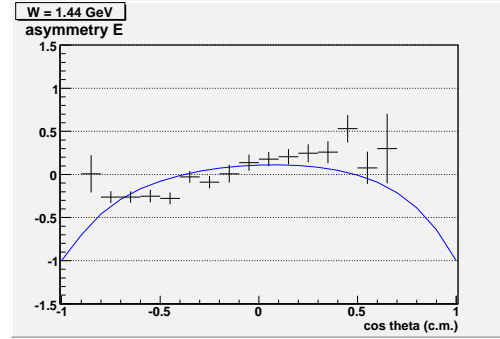


(d) $E_\gamma = 2250$ MeV

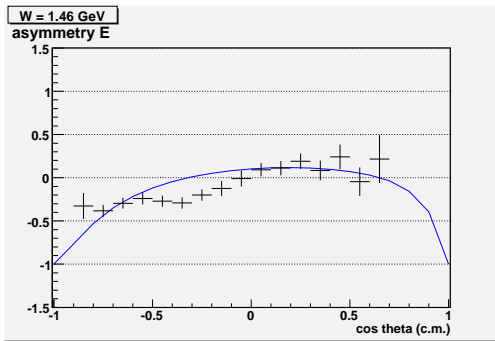
Figure 8.6: The figures show asymmetry E for all groups ($E_{\text{electron}} = 1.645$ GeV and 2.478 GeV) in the different E_γ comparing with the two theoretical predictions, SAID2009 (blue line) and MAID2007 (red line).



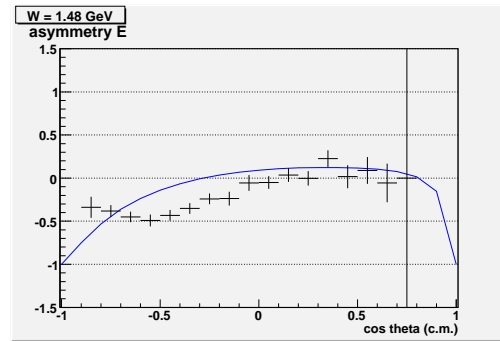
(a) $W = 1.42$ GeV



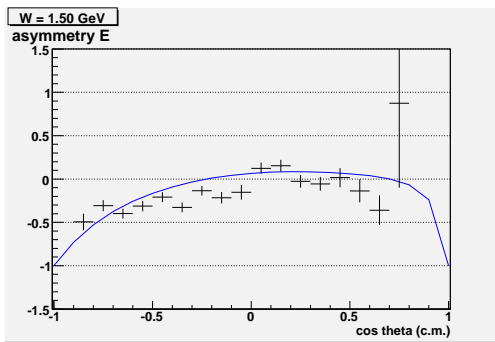
(b) $W = 1.44$ GeV



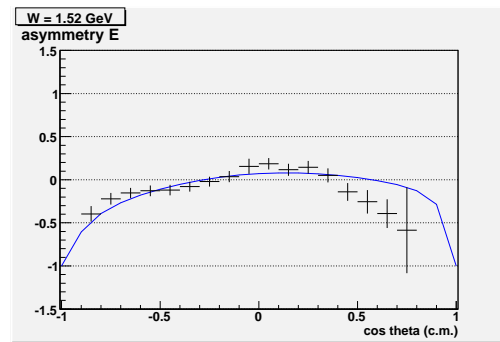
(c) $W = 1.46$ GeV



(d) $W = 1.48$ GeV

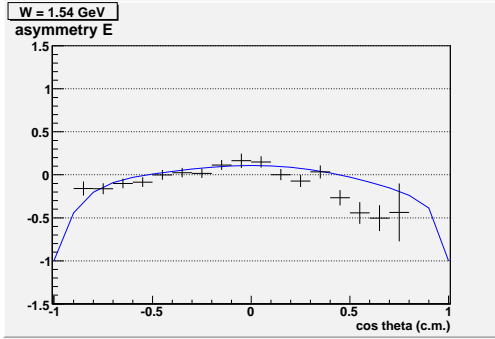


(e) $W = 1.50$ GeV

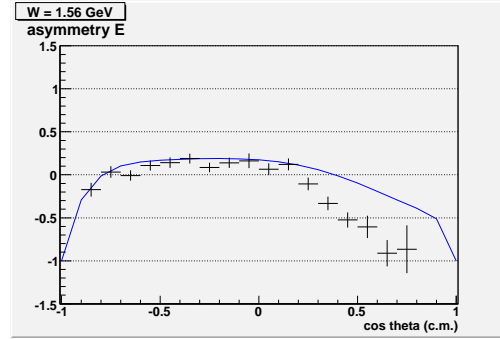


(f) $W = 1.52$ GeV

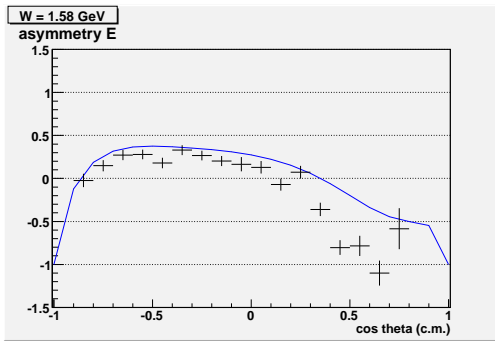
Figure 8.7: The figures show asymmetry E for all groups in the different W comparing with the three theoretical predictions, SAID2009 (blue line), MAID2007 (red line), and EBAC (pink line).



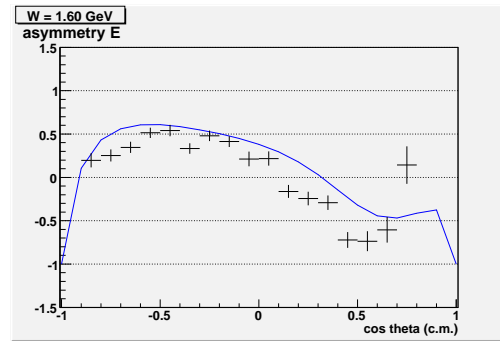
(a) $W = 1.54$ GeV



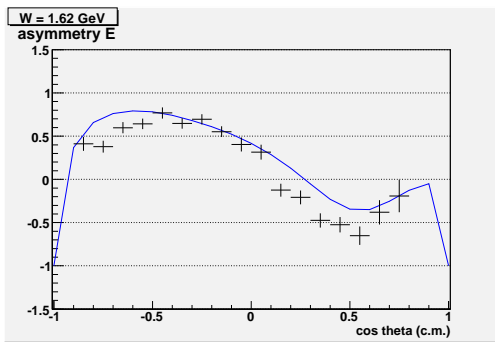
(b) $W = 1.56$ GeV



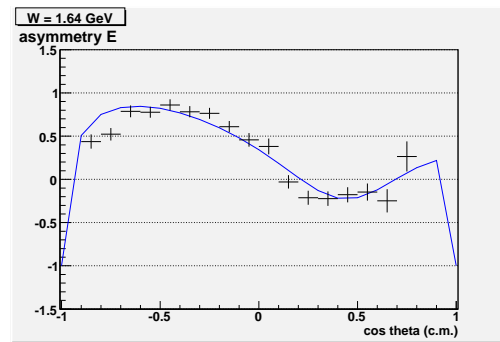
(c) $W = 1.58$ GeV



(d) $W = 1.60$ GeV

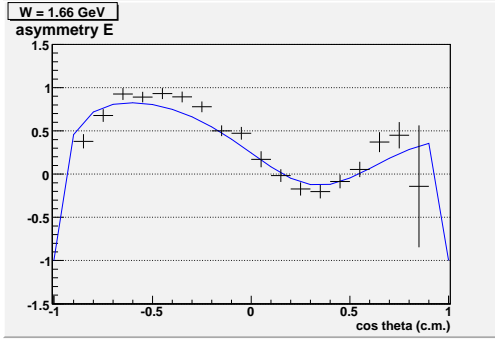


(e) $W = 1.62$ GeV

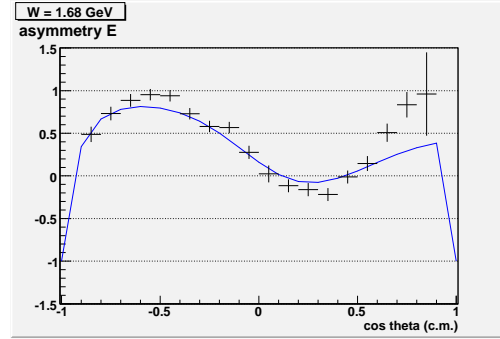


(f) $W = 1.64$ GeV

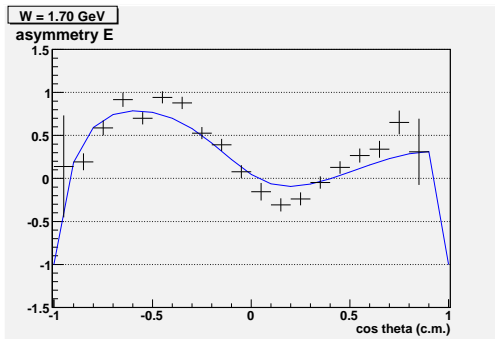
Figure 8.8: The figures show asymmetry E for all groups in the different W comparing with the two theoretical predictions, SAID2009 (blue line) and MAID2007 (red line).



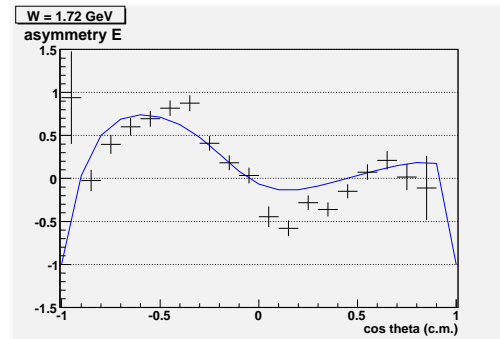
(a) $W = 1.66$ GeV



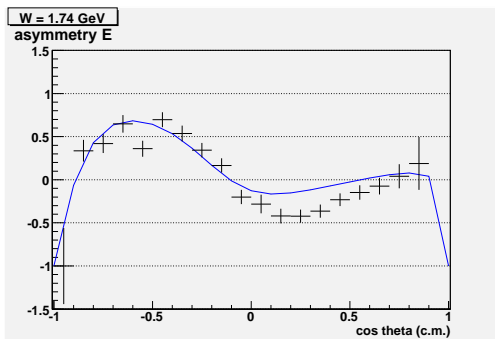
(b) $W = 1.68$ GeV



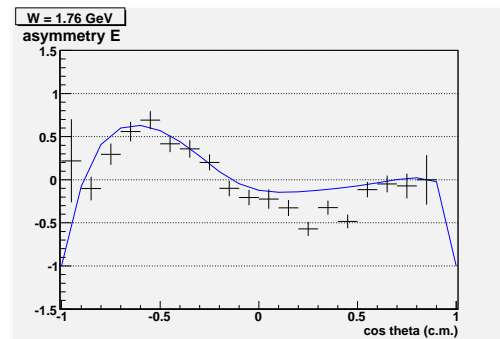
(c) $W = 1.70$ GeV



(d) $W = 1.72$ GeV

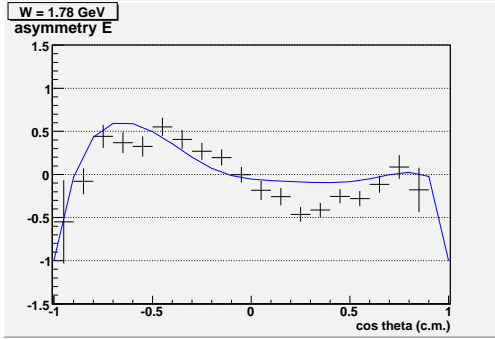


(e) $W = 1.74$ GeV

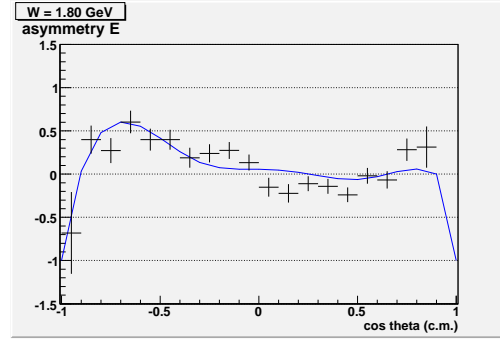


(f) $W = 1.76$ GeV

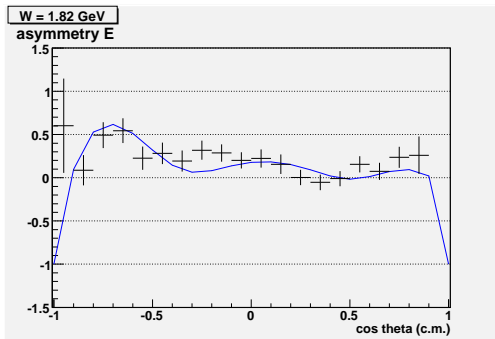
Figure 8.9: The figures show asymmetry E for all groups in the different W comparing with the two theoretical predictions, SAID2009 (blue line) and MAID2007 (red line).



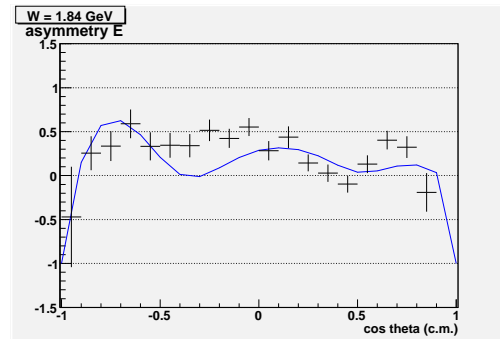
(a) $W = 1.78$ GeV



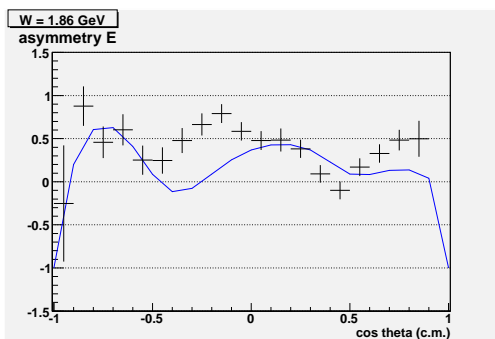
(b) $W = 1.80$ GeV



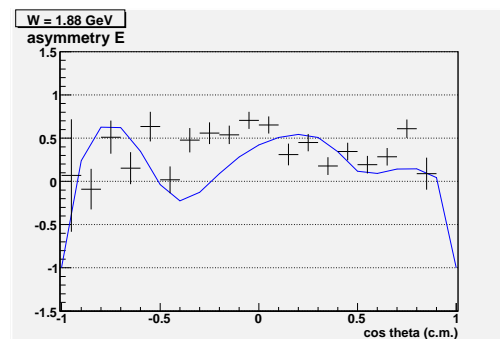
(c) $W = 1.82$ GeV



(d) $W = 1.84$ GeV

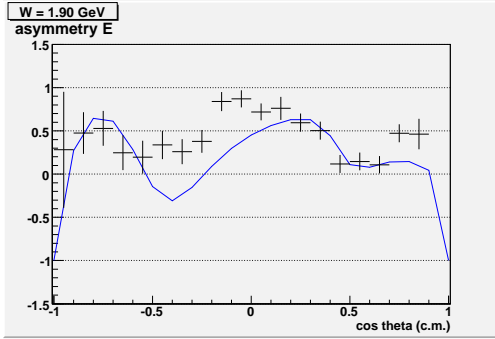


(e) $W = 1.86$ GeV

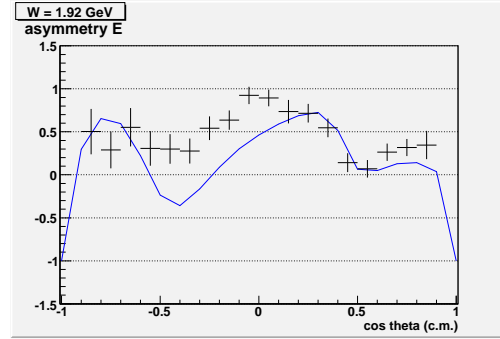


(f) $W = 1.88$ GeV

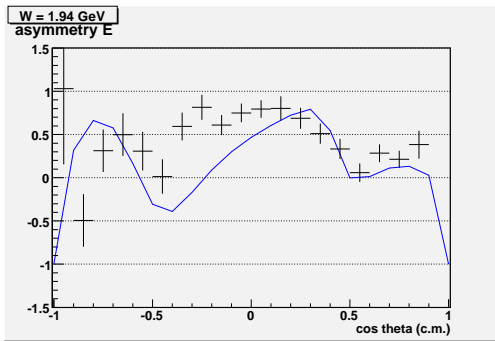
Figure 8.10: The figures show asymmetry E for all groups in the different W comparing with the two theoretical predictions, SAID2009 (blue line) and MAID2007 (red line).



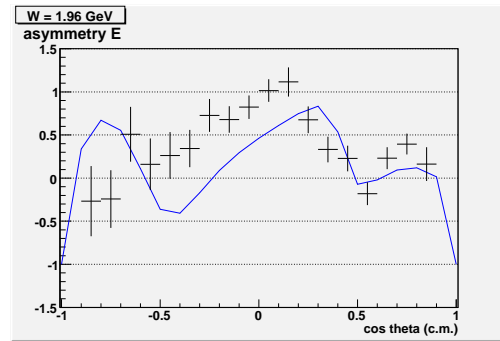
(a) $W = 1.90$ GeV



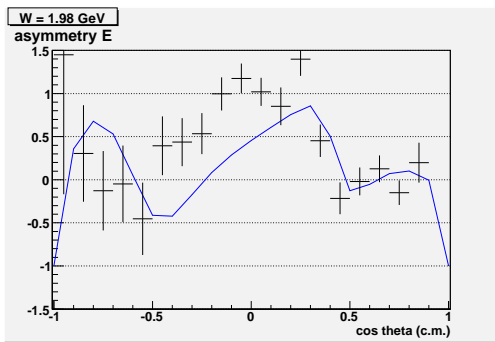
(b) $W = 1.92$ GeV



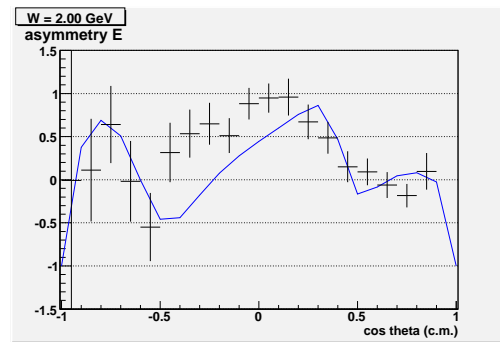
(c) $W = 1.94$ GeV



(d) $W = 1.96$ GeV



(e) $W = 1.98$ GeV



(f) $W = 2.00$ GeV

Figure 8.11: The figures show asymmetry E for all groups in the different W comparing with the two theoretical predictions, SAID2009 (blue line) and MAID2007 (red line).

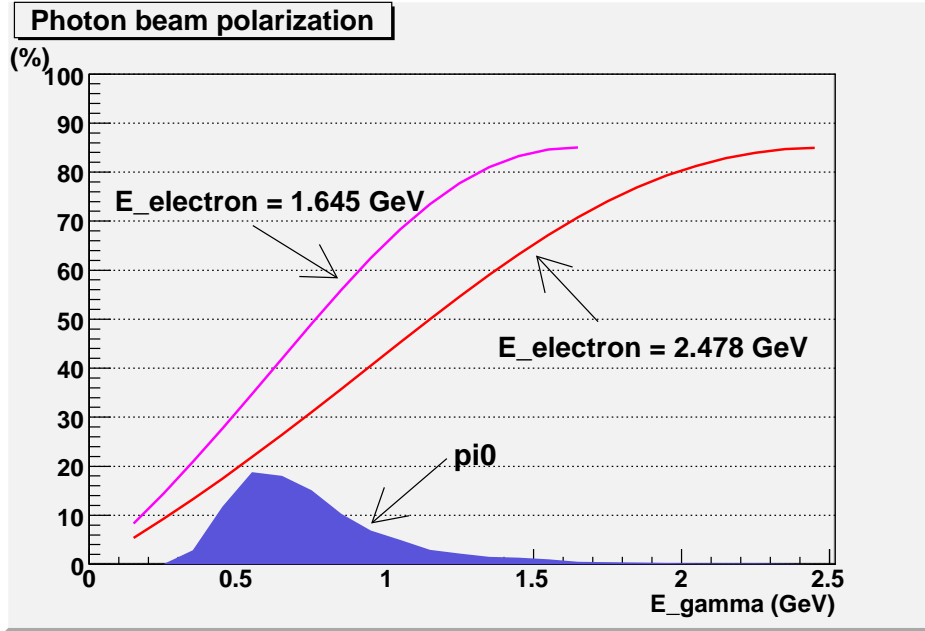


Figure 8.12: The polarization of the photon beams at (1) $E_{\text{electron}} = 1.645$ GeV (pink line) and (2) $E_{\text{electron}} = 2.478$ GeV (red line). The blue figure shows the percentage of the events of π^0 at different E_γ .

mentioned in section 8.1 (see Figure 8.12 and Table 8.2). If the electron beam energy were lower in our experiment, the results would have been more precise.

The missing mass of π^0 is ϕ - or sector-dependent (see section 5.2.8), and it is likely that the off-axis photon-beam position caused ϕ -dependent energy loss especially of low-momentum protons. Therefore, the energy loss corrections, that assumes that the photon beam is going along the z-axis, does not work properly. As a result, the π^0 mass not only depends on the sector (or ϕ), but also deviates from the value of 135 MeV (see Figure 5.14). Figure 5.19 shows the distribution of the detected proton momentum has a peak at $p_{\text{proton}} = 400\text{--}600$ MeV, thus events with proton momentum range from 350 to 600 MeV were not cut out. Therefore, this affects the results for forward angles especially at low E_γ , where protons highly depend on energy loss corrections, because of their high yields and are very sensitive to the value of the dilution factor.

The three theoretical predictions are in close agreement with our data below $E_\gamma \simeq 1.35$ GeV. As seen in Figures 8.2 ~ 8.4, above $E_\gamma = 1.35$ GeV, the predictions of both SAID and MAID models deviate from our results, espe-

cially at intermediate and backward angles ($\cos \theta \leq 0.0$, see Figure 8.4 ~ 8.5). The comparison of the results for $E_{\text{electron}} = 1.645$ GeV and $E_{\text{electron}} = 2.478$ GeV data sets (Figure 8.13 ~ 8.15) shows only small differences except for $\cos \theta_{\text{c.m.}}^{\pi^0} = -0.95$.

As shown in Figure 8.17 ~ 8.21, the asymmetry E for fixed $\cos \theta_{\text{c.m.}}^{\pi^0}$ as a function of W shows good agreement with the prediction by SAID, for $0.0 \leq \cos \theta_{\text{c.m.}}^{\pi^0} \leq 0.3$. However when $\cos \theta_{\text{c.m.}}^{\pi^0}$ has negative values ($\cos \theta_{\text{c.m.}}^{\pi^0} \leq 0.0$), our results show peaks around $W \simeq 1.50$ GeV and $W \simeq 1.65$ GeV (also around $W \simeq 1.75$ GeV), but the SAID predictions often do not show these peaks. Especially around the peak at $W \simeq 1.50$ GeV, the values of our asymmetries are negative, but SAID predictions are positive. Above $W = 1.50$ GeV and $-0.35 \leq \cos \theta_{\text{c.m.}}^{\pi^0} \leq -0.05$, the prediction by SAID always deviates from the experimental result. And for $\cos \theta_{\text{c.m.}}^{\pi^0} \geq 0.45$, the results show more variations than the SAID predictions.

The measured helicity asymmetries E , that are extracted from the double polarization data, contain fruitful information. The deviation between the model predictions and these results shows that the models need to further constrain their parameters, such as coupling constants.

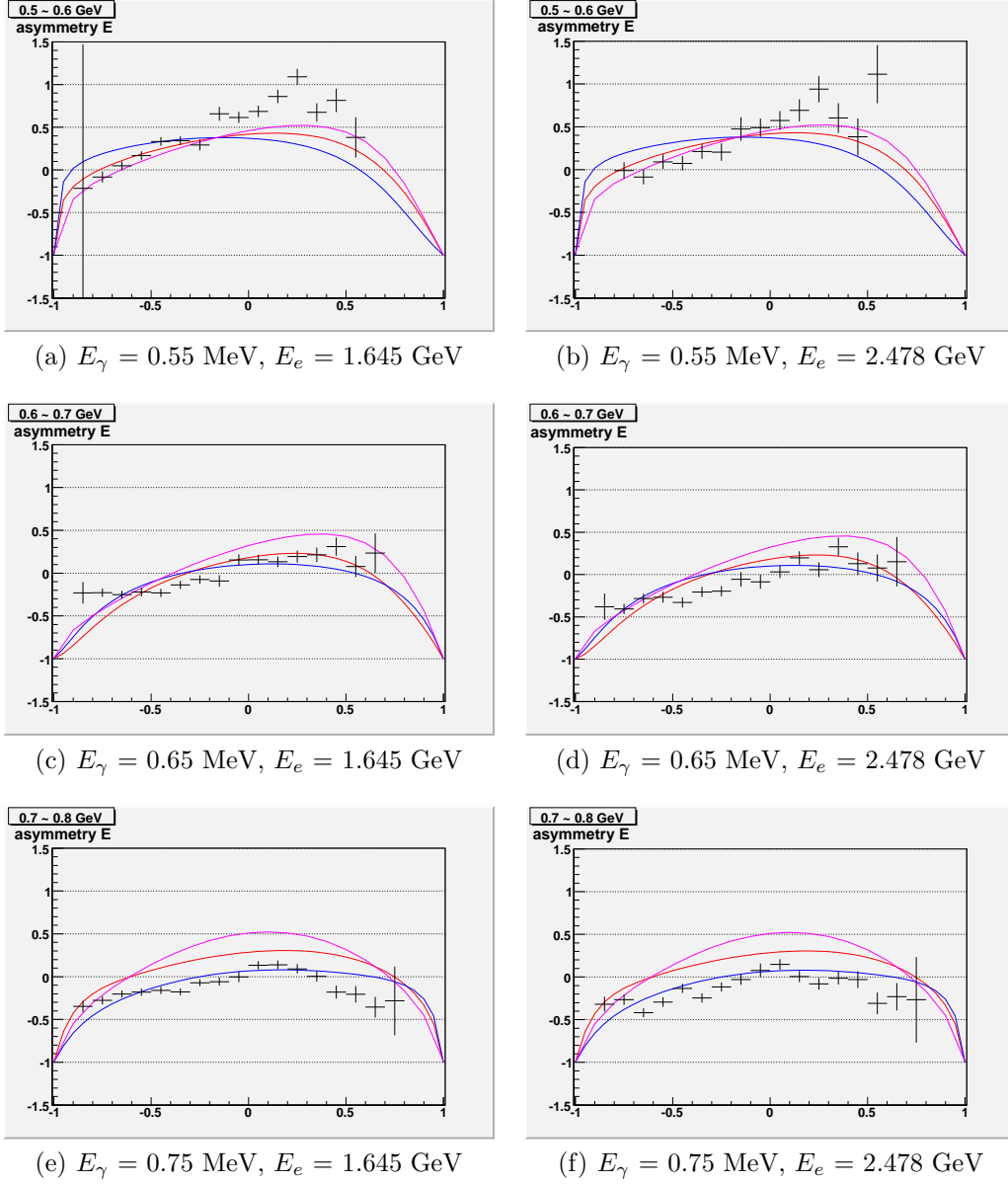


Figure 8.13: The figures show the comparison between group 1 \sim 3 ($E_{\text{electron}} = 1.645$ GeV) and group 4 \sim 7 ($E_{\text{electron}} = 2.478$ GeV) with different E_γ . $\Delta E_\gamma = 100$ MeV bins.

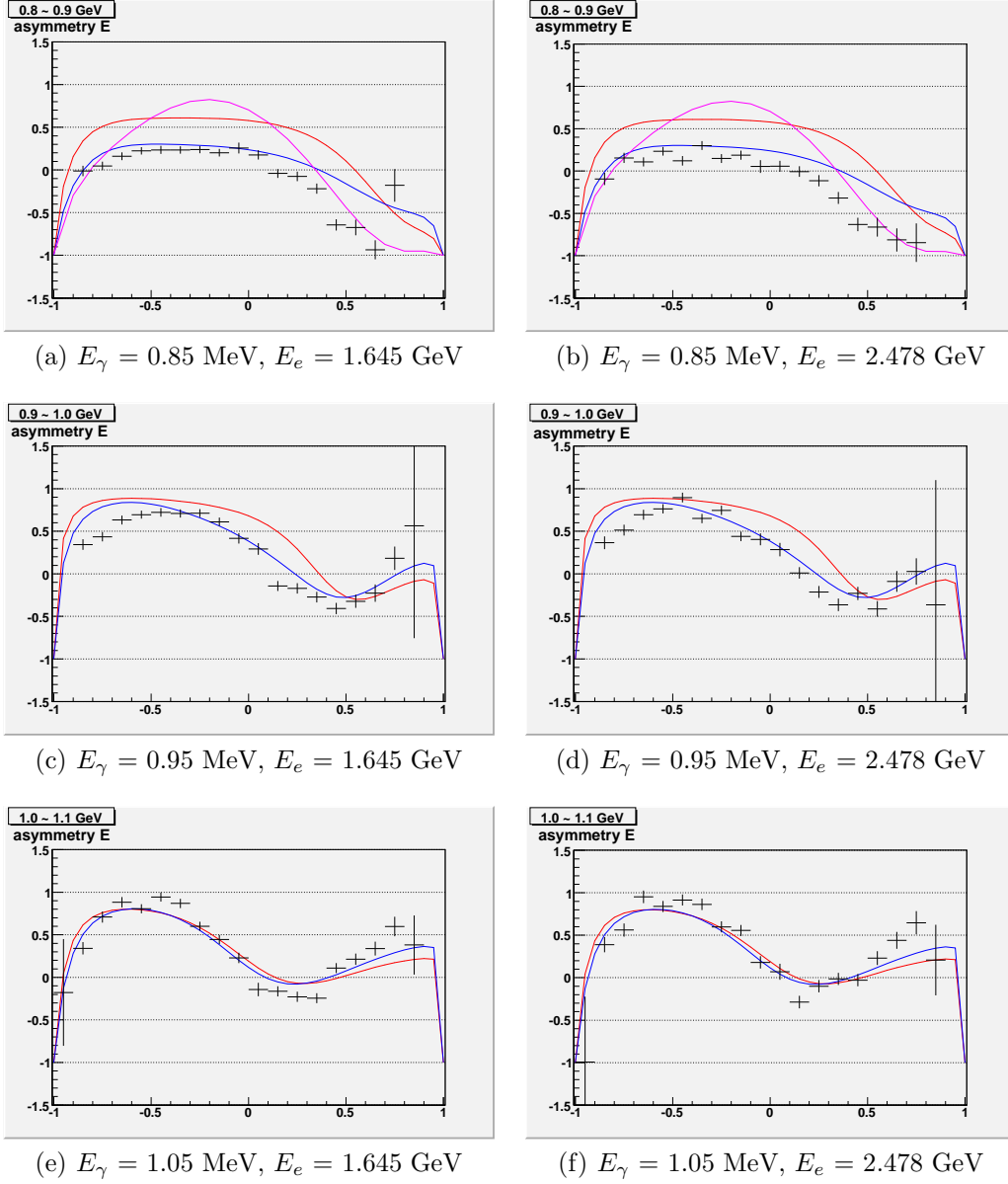


Figure 8.14: The figures show the comparison between group 1 \sim 3 ($E_{\text{electron}} = 1.645$ GeV) and group 4 \sim 7 ($E_{\text{electron}} = 2.478$ GeV) with different E_γ . $\Delta E_\gamma = 100$ MeV bins.

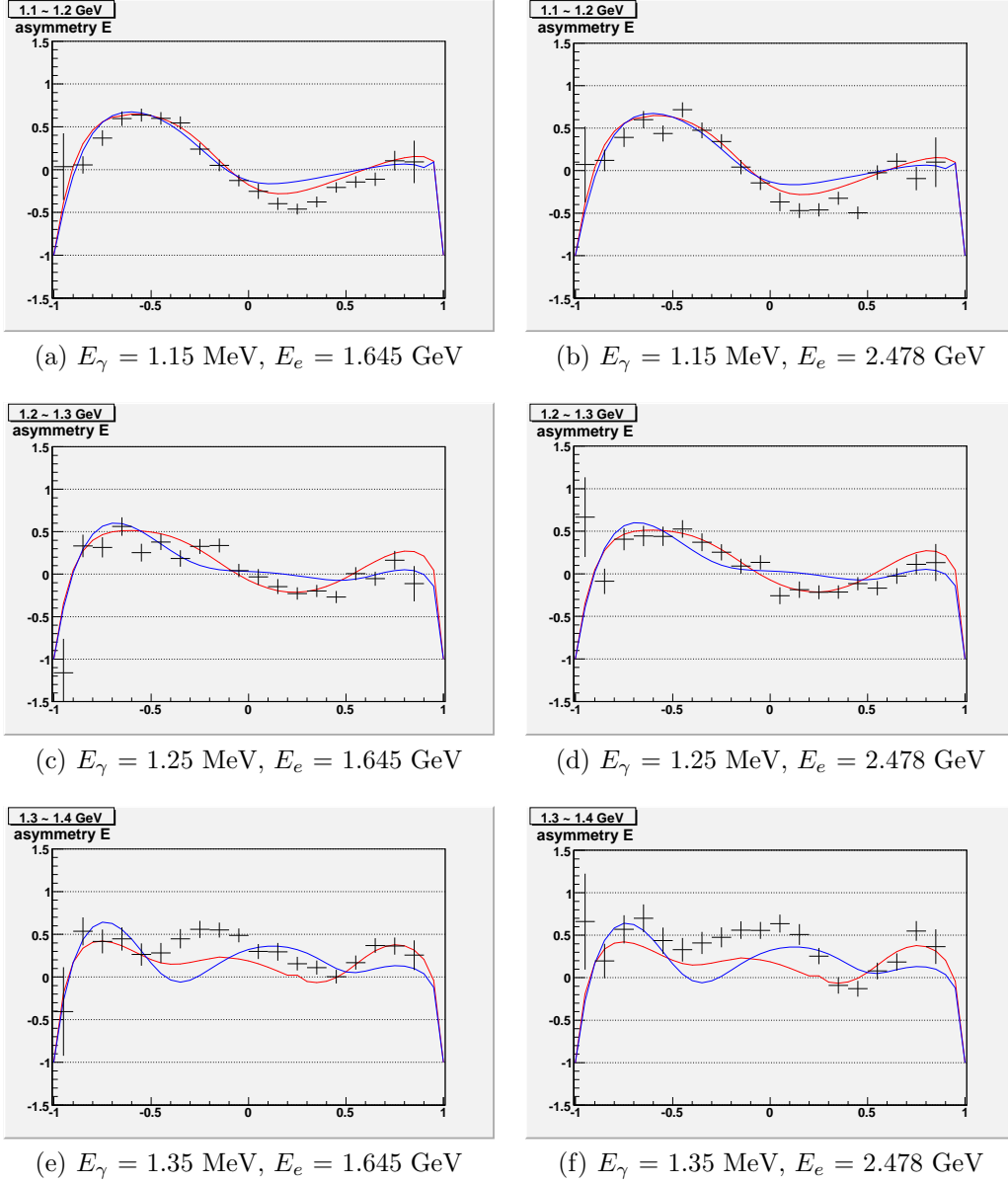


Figure 8.15: The figures show the comparison between group 1 \sim 3 ($E_{\text{electron}} = 1.645$ GeV) and group 4 \sim 7 ($E_{\text{electron}} = 2.478$ GeV) with different E_γ . $\Delta E_\gamma = 100$ MeV bins.

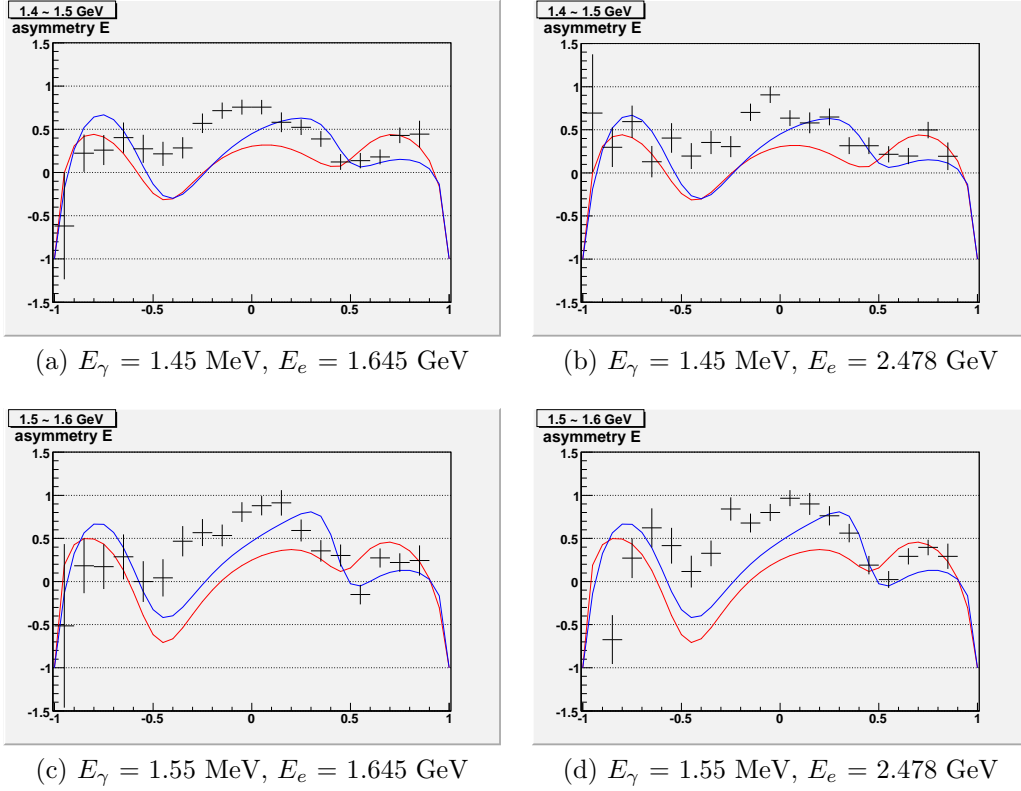
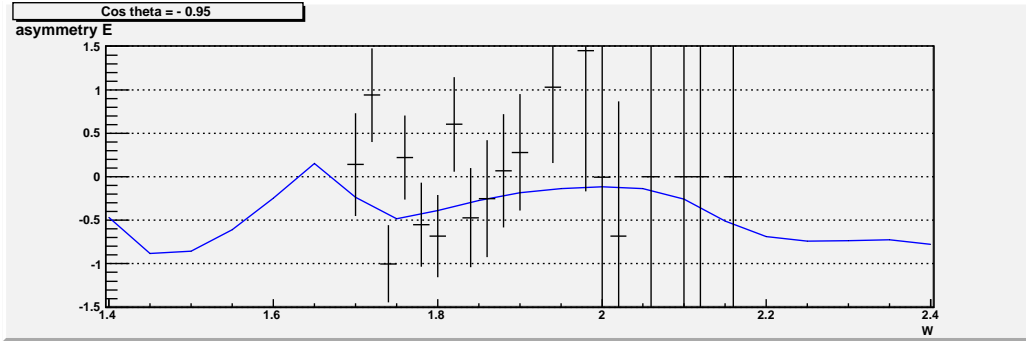


Figure 8.16: The figures show the comparison between group 1 ~ 3 ($E_{\text{electron}} = 1.645$ GeV) and group 4 ~ 7 ($E_{\text{electron}} = 2.478$ GeV) with different E_{γ} . $\Delta E_{\gamma} = 100$ MeV bins.

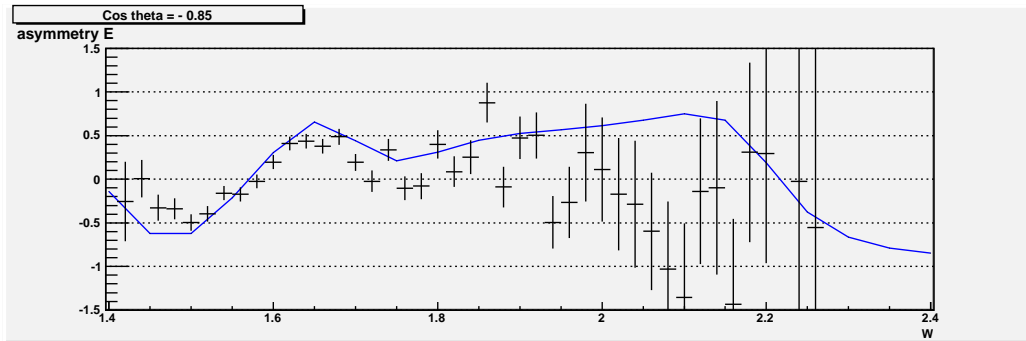
8.2.2 Comparison with the data of MAMI

The helicity states, 1/2 and 3/2, measurement for the reaction $\gamma p \rightarrow \pi^0 p$ is done at MAMI (the Mainz microton, Germany) tagging photon facility to test the GDH sum rule [98, 99] (see Section D). The experiment was done with a 4 π - detector system, and a frozen-spin butanol target. Circularly polarized photons were produced by bremsstrahlung of longitudinally polarized electrons with a degree of polarization of about 75 %. The detection system was able to tag photons in the range from 50 to 800 MeV with a resolution of about 2 MeV [100].

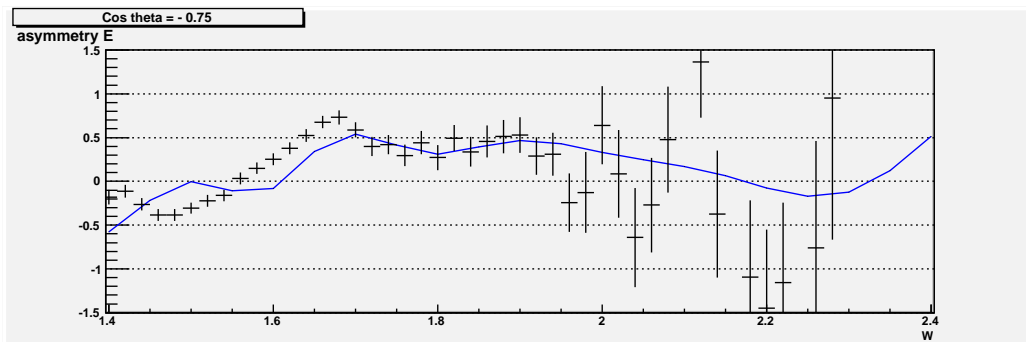
The helicity asymmetry E at MAMI was calculated by the differential cross sections of (1) the unpolarized hydrogen target and (2) the polarized butanol



(a) $\cos \theta = -0.95$

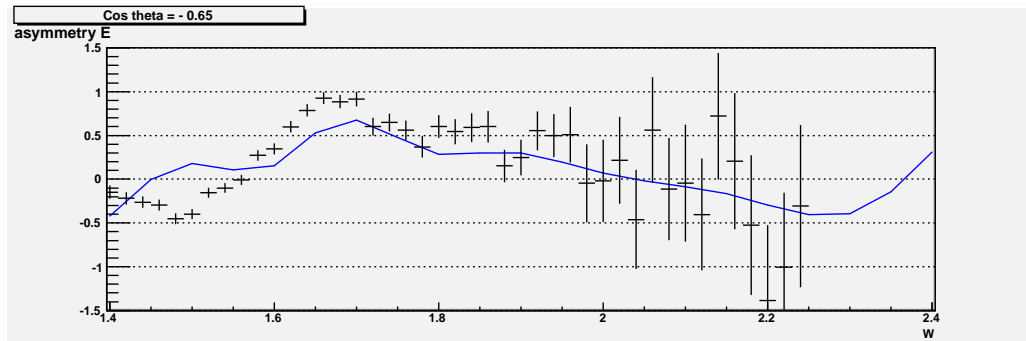


(b) $\cos \theta = -0.85$

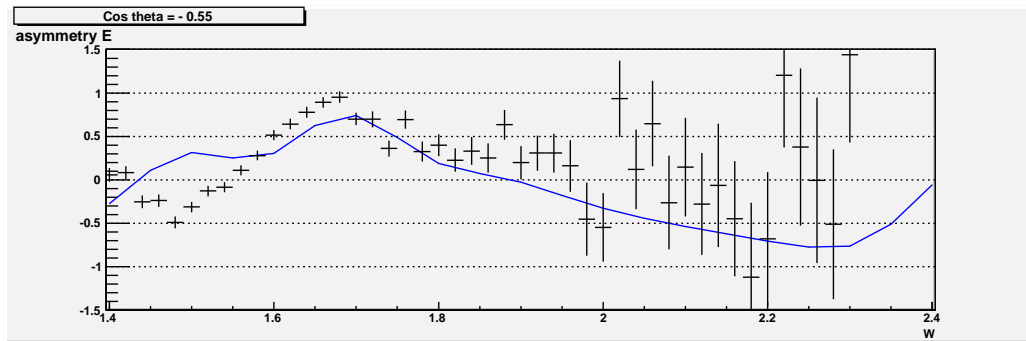


(c) $\cos \theta = -0.75$

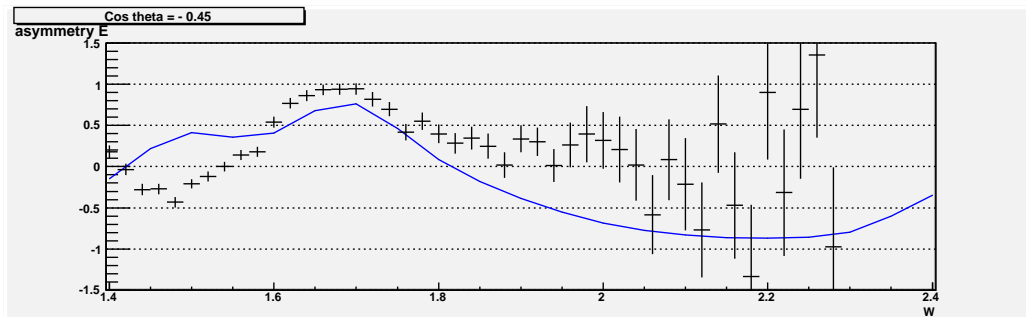
Figure 8.17: The figures show asymmetry E for all groups in the different $\cos \theta$ with different W . The blue line is the prediction by SAID(2009).



(a) $\cos \theta = -0.65$

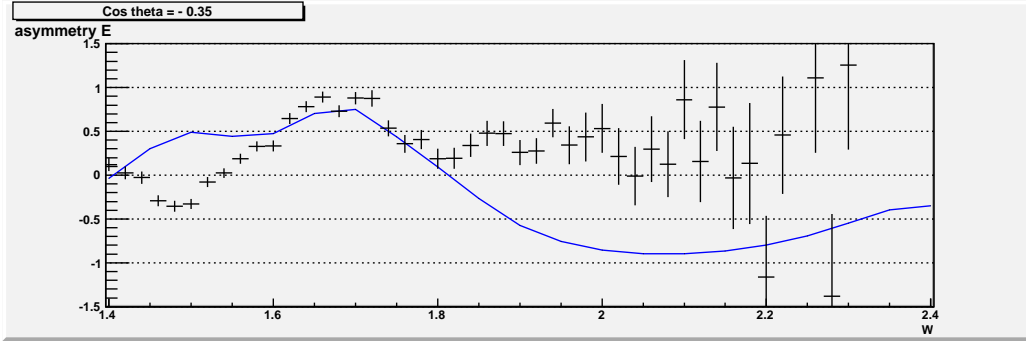


(b) $\cos \theta = -0.55$

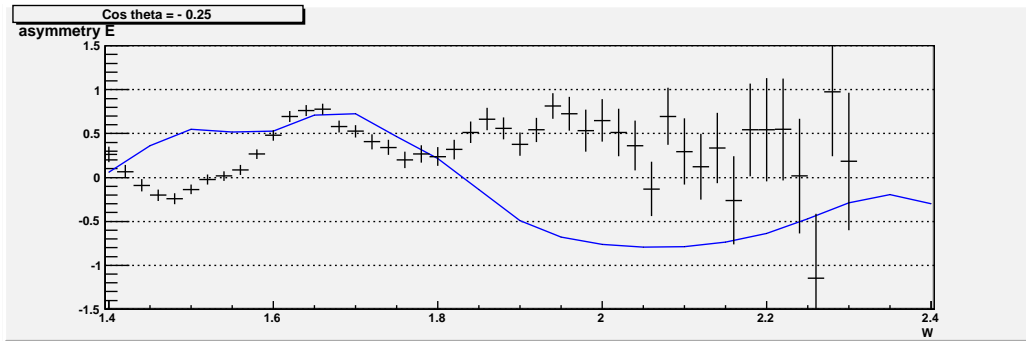


(c) $\cos \theta = -0.45$

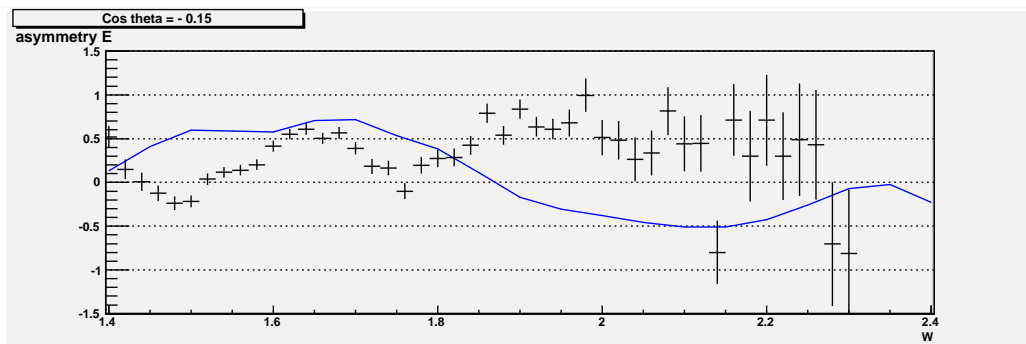
Figure 8.18: The figures show asymmetry E for all groups in the different $\cos \theta$ with different W . The blue line is the prediction by SAID(2009).



(a) $\cos \theta = -0.35$

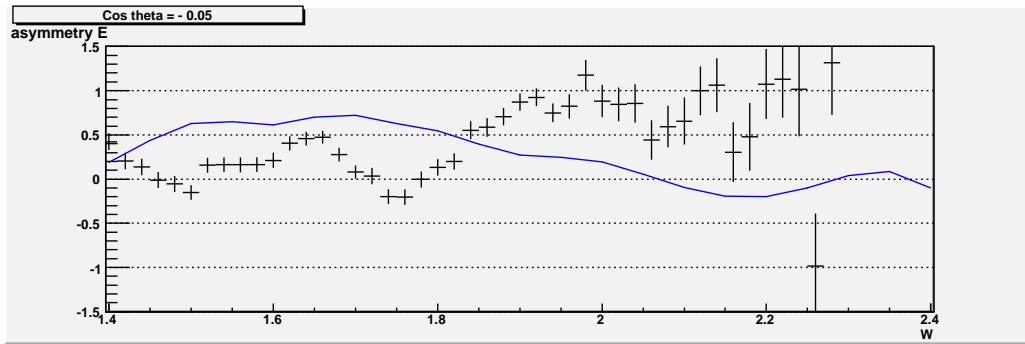


(b) $\cos \theta = -0.25$

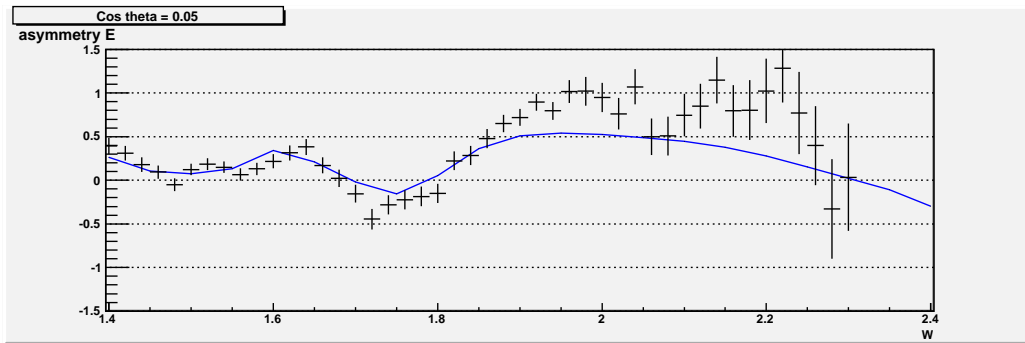


(c) $\cos \theta = -0.15$

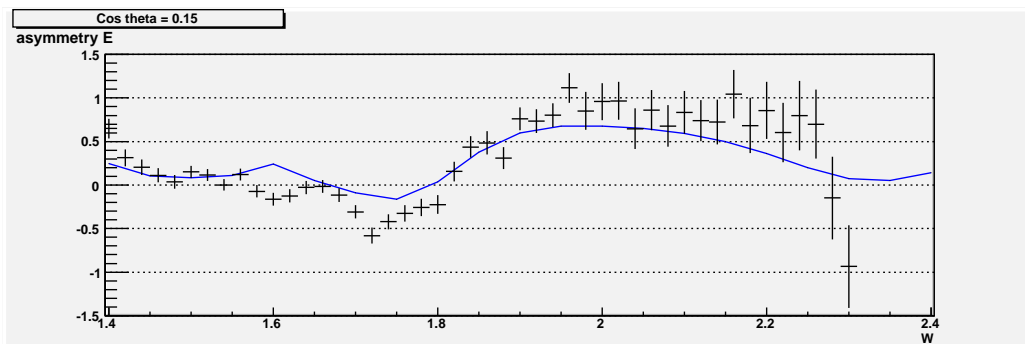
Figure 8.19: The figures show asymmetry E for all groups in the different $\cos \theta$ with different W . The blue line is the prediction by SAID(2009).



(a) $\cos \theta = -0.05$

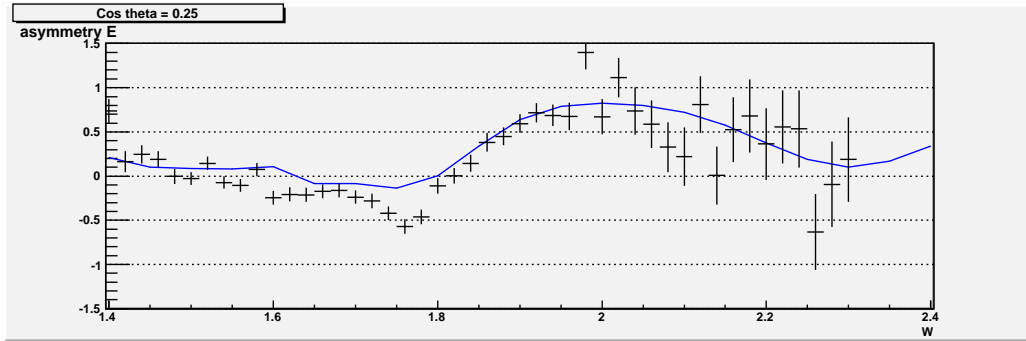


(b) $\cos \theta = 0.05$

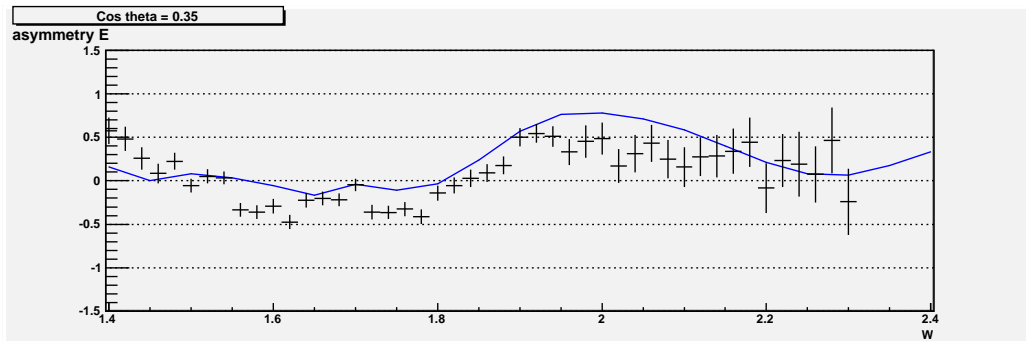


(c) $\cos \theta = 0.15$

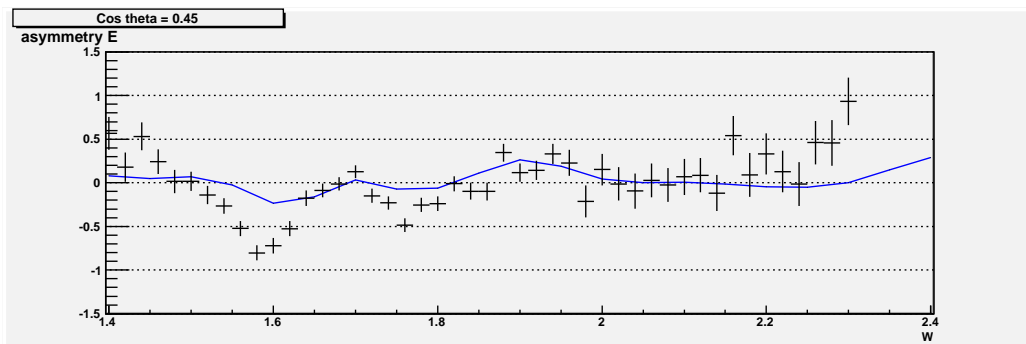
Figure 8.20: The figures show asymmetry E for all groups in the different $\cos \theta$ with different W . The blue line is the prediction by SAID(2009).



(a) $\cos \theta = 0.25$

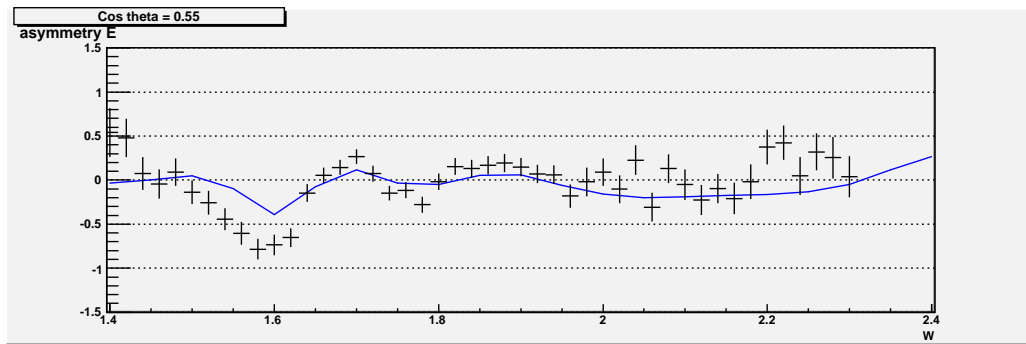


(b) $\cos \theta = 0.35$

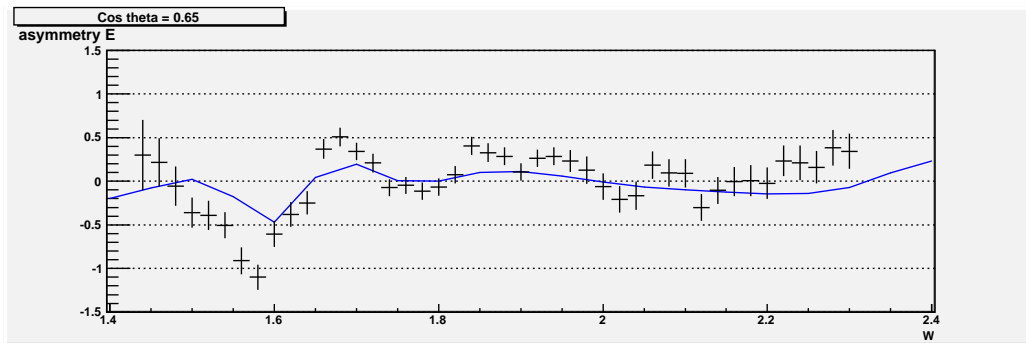


(c) $\cos \theta = 0.45$

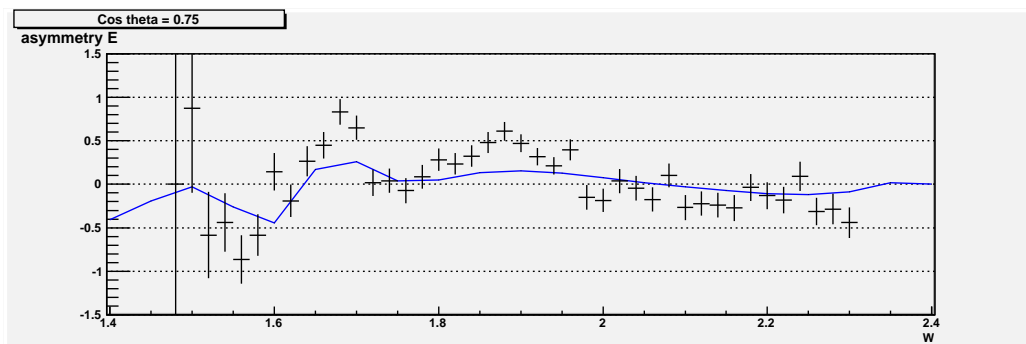
Figure 8.21: The figures show asymmetry E for all groups in the different $\cos \theta$ with different W . The blue line is the prediction by SAID(2009).



(a) $\cos \theta = 0.55$

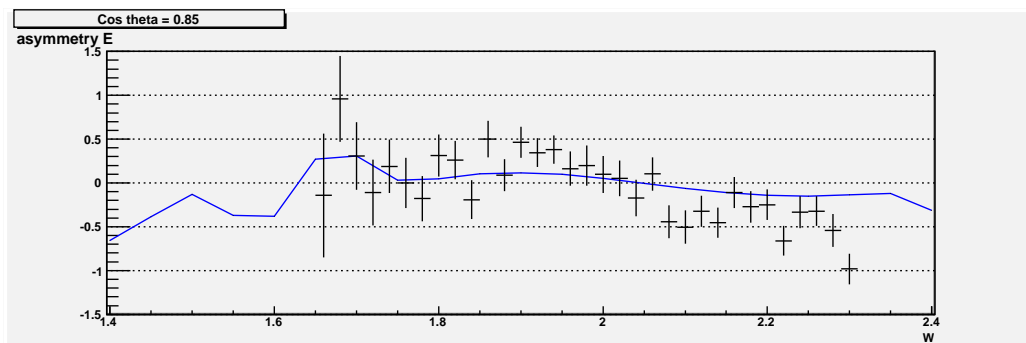


(b) $\cos \theta = 0.65$

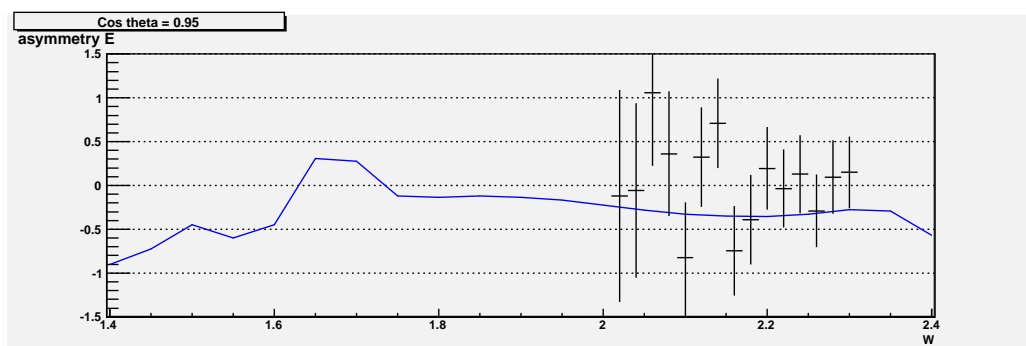


(c) $\cos \theta = 0.75$

Figure 8.22: The figures show asymmetry E for all groups in the different $\cos \theta$ with different W . The blue line is the prediction by SAID(2009).



(a) $\cos \theta = 0.85$



(b) $\cos \theta = 0.95$

Figure 8.23: The figures show asymmetry E for all groups in the different $\cos \theta$ with different W . The blue line is the prediction by SAID(2009).

target [100] with the equation

$$E = \frac{(-1) \times [d\sigma_{3/2(pol)}/d\Omega - d\sigma_{1/2(pol)}/d\Omega]}{2 \times d\sigma_{(unpol)}/d\Omega}, \quad (8.1)$$

where $d\sigma_{1/2(pol)}/d\Omega$, $d\sigma_{3/2(pol)}/d\Omega$, and $d\sigma_{(unpol)}/d\Omega$ are the polarized differential cross sections of helicity 1/2, 3/2, and unpolarized differential cross section, respectively¹.

To get the asymmetry points with Mainz data, the polarization of the butanol target, $P_{\odot} = 85\%$, the polarization of the electron beam, $P_{\text{electron}} = 75\%$, and the energy of the electron beam $E_{\text{electron}} = 855$ MeV are used (energy correction is included). The helicity asymmetry E of my result is compared with that of MAMI for the $p\gamma \rightarrow \pi^0 p$ channel in the photon energy range 550 to 790 MeV with 20 MeV of energy bin.

The main differences of the experiments between MAMI and FROST are

(1) The energy of electron beam;

Two different energies of electron beams are used in FROST experiment, 1.645 GeV and 2.478, but in MAMI, much lower energy 0.855 GeV is used.

(2) The butanol target length;

The length of target is 5 cm in FROST, and 2 cm in MAMI.

The carbon target is used in FROST to get a dilution factor. The comparison between FROST and MAMI experiments are in Table 8.4. Although the size of the error bars is not small, the results from MAMI, for the purpose of evaluating GDH sum rule, agree overall with the results from CLAS FROST experiment except for the lower photon energy bins (Figure 8.24 ~ 8.25).

8.3 Summary

The helicity asymmetry E in the channel of $\gamma p \rightarrow \pi^0 p$ was measured on the longitudinally polarized proton using circularly polarized photon beam with photon beam energy between 550 MeV to 2400 MeV. The experimental result are compared to three available model calculations. The result has a good agreement up to $E_{\gamma} = 1.35$ GeV with the model calculations. However, a significant deviation is observed at the backward pion scattering angle,

¹detailed data information and calculations of E are got from Dr. P.Pedroni (INFN, Sezione di Pavia)

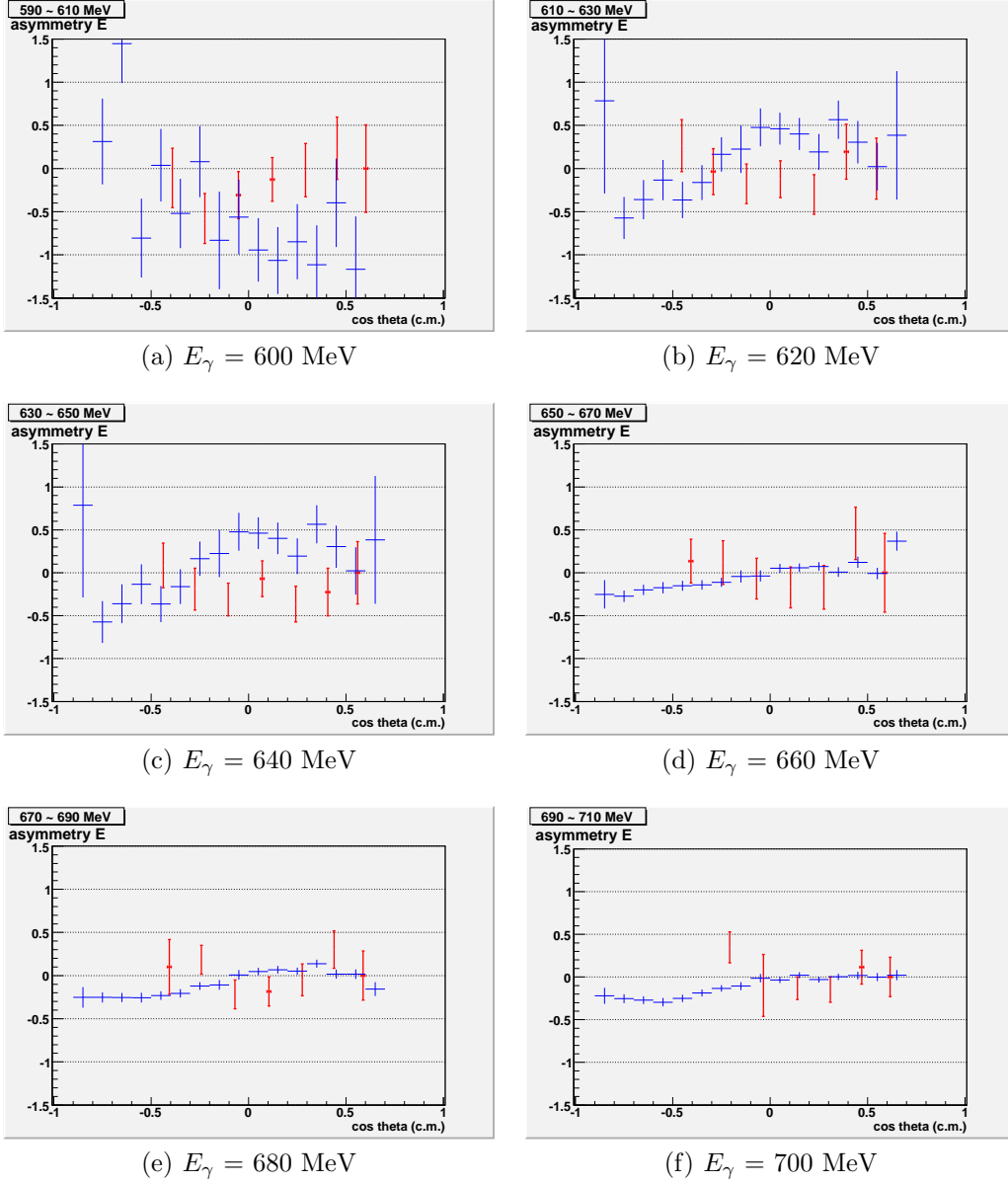


Figure 8.24: The figures show the comparison with the data from Mainz, FROST (blue) and MAMI (red). $\Delta E_\gamma = 20$ MeV bins. $E_\gamma = 855$ MeV, $P_{\text{electron}} = 75\%$, and $P_T = 85\%$.

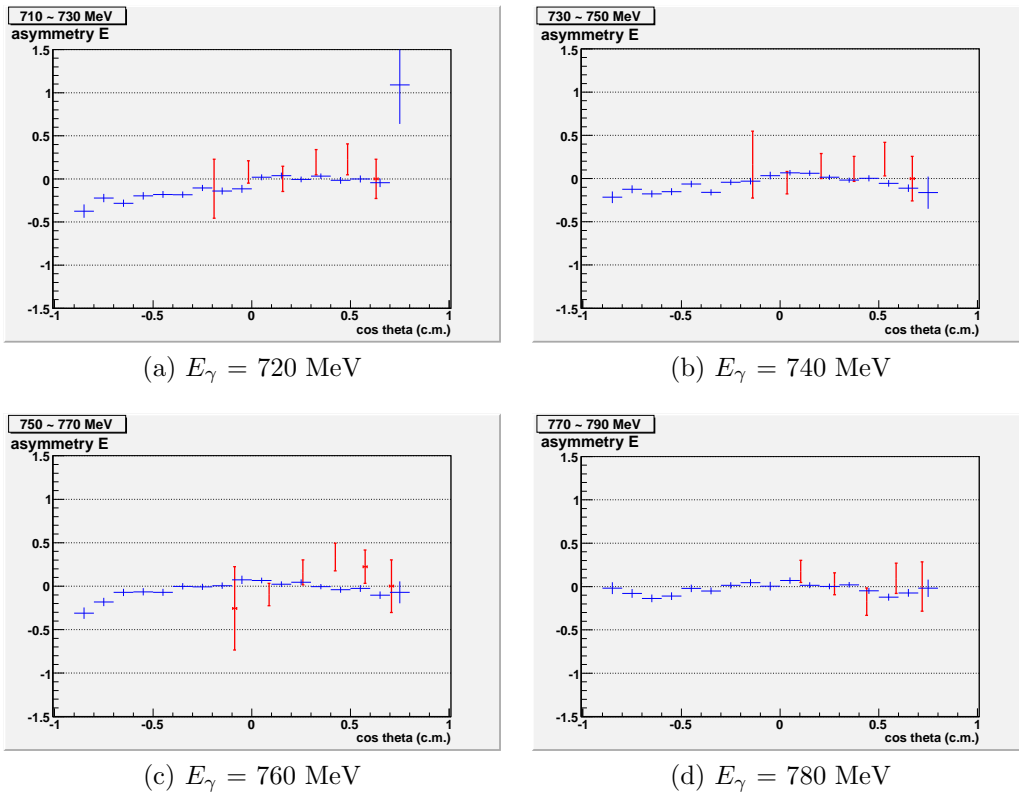


Figure 8.25: The figures show the comparison with the data from Mainz, FROST (blue) and MAMI (red). $\Delta E_\gamma = 20$ MeV bins. $E_\gamma = 855$ MeV, $P_{\text{electron}} = 75\%$, and $P_T = 85\%$.

$-0.75 \leq \cos \theta \leq 0$. The helicity asymmetry is very sensitive to various dynamical reaction effects, such as channel coupling and final state interactions. Therefore, the new data will help to constrain the parameters of the theoretical models.

Table 8.2: Polarization of photon beam, number of events (%) by E_γ (1.645 GeV and 2.478 GeV), by 100 MeV energy E_{electron} bins. The “pol.” is the polarization of photon beam, E_γ , and “evnt num.” is number of events.

E_{electron} E_γ (GeV)	Period 1 ~ 3 1.645 GeV		Period 4 ~ 7 2.478 GeV	
	pol.(%)	evnt num.(%)	pol.(%)	evnt num.(%)
0.35 ± 0.05	20.85	661,401 (5.57)	13.26	0 (0.00)
0.45 ± 0.05	27.68	1,581,294 (13.32)	17.48	0 (0.00)
0.55 ± 0.05	34.75	1,111,922 (9.36)	21.86	1,086,143 (9.15)
0.65 ± 0.05	41.93	726,202 (6.11)	26.40	1,320,303 (11.12)
0.75 ± 0.05	49.05	615,668 (5.18)	31.04	1,082,831 (9.12)
0.85 ± 0.05	55.96	384,418 (3.24)	35.77	765,793 (6.45)
0.95 ± 0.05	62.44	248,309 (2.09)	40.54	518,011 (4.36)
1.05 ± 0.05	68.33	195,563 (1.65)	45.29	353,843 (2.98)
1.15 ± 0.05	73.47	119,469 (1.01)	50.00	202,808 (1.71)
1.25 ± 0.05	77.72	78,213 (0.66)	54.59	157,041 (1.32)
1.35 ± 0.05	81.01	62,361 (0.53)	59.01	100,161 (0.84)
1.45 ± 0.05	83.30	53,428 (0.45)	63.22	97,382 (0.82)
1.55 ± 0.05	84.61	30,277 (0.25)	67.15	77,992 (0.66)
1.65 ± 0.05	85.00	0 (0.00)	70.76	59,605 (0.50)
1.75 ± 0.05			74.01	44,818 (0.38)
1.85 ± 0.05			76.87	37,968 (0.32)
1.95 ± 0.05			79.30	31,251 (0.26)
2.05 ± 0.05			81.30	23,496 (0.20)
2.15 ± 0.05			82.86	21,230 (0.18)
2.25 ± 0.05			83.99	15,459 (0.13)
2.35 ± 0.05			84.69	11,182 (0.09)
2.45 ± 0.05			84.99	0 (0.00)
total		5,868,525 (49.42)		6,007,317 (50.58)

Table 8.3: Polarization of photon beam, number of events (%) by E_γ (Total), by 100 MeV energy E_{electron} bins. The “pol.” is the polarization of photon beam, E_γ , and “evnt num.” is number of events.

E_γ (GeV)	Total	
	evnt num.	(%)
0.35 ± 0.05	661,401	(5.57)
0.45 ± 0.05	1,581,294	(13.32)
0.55 ± 0.05	2,198,065	(18.51)
0.65 ± 0.05	2,046,505	(17.23)
0.75 ± 0.05	1,698,499	(14.30)
0.85 ± 0.05	1,150,211	(9.69)
0.95 ± 0.05	766,320	(6.45)
1.05 ± 0.05	549,406	(4.63)
1.15 ± 0.05	322,277	(2.71)
1.25 ± 0.05	235,254	(1.98)
1.35 ± 0.05	162,522	(1.37)
1.45 ± 0.05	150,810	(1.27)
1.55 ± 0.05	108,269	(0.91)
1.65 ± 0.05	59,605	(0.50)
1.75 ± 0.05	44,818	(0.38)
1.85 ± 0.05	37,968	(0.32)
1.95 ± 0.05	31,251	(0.26)
2.05 ± 0.05	23,496	(0.20)
2.15 ± 0.05	21,230	(0.18)
2.25 ± 0.05	15,459	(0.13)
2.35 ± 0.05	11,182	(0.09)
2.45 ± 0.05	0	(0.00)
total	11,875,842	(100.0)

	FROST[101]	MAMI[98, 99, 100]
Measurement	double polarization observable E	GDH sum rule
Target	frozen-spin butanol (C_4H_9OH) (DNP technique)	frozen-spin butanol (C_4H_9OH) (DNP technique)
Energy of electron beam	1.645 GeV 2.478 GeV	855 MeV
Polarization		
Target	78 % \sim 92 %	max \sim 90 %
Electron	79 % \sim 89 %	\sim 75 %
Target length	5 cm	2 cm
Unpolarized target	Carbon (same experiment; down stream of butanol target)	
Coverage angle (θ_{cm})	8° \sim 140°	21° \sim 159°

Table 8.4: The comparison between FROST and MAMI experiments for the asymmetry E of the $p\gamma \rightarrow \pi^0 p$ channel.

Bibliography

- [1] F. Halzen and A. D. Martin, *Quarks and Leptons: An Introductory Course in Modern Particle Physics* (John Wiley and Sons, Inc., 1984).
- [2] N. Isgur and G. Karl, Phys. Rev. D **18**, 4187 (1978).
- [3] N. Isgur and G. Karl, Phys. Rev. D **19**, 2653 (1979).
- [4] P. Bogolioubov, Ann. Inst. Henri Poincare **8**, 163 (1967).
- [5] A. Chodos, R. Jaffe, K. Johnson, C. Thorn, and V. Wesskopf, Phys. Rev. D **9**, 3471 (1974).
- [6] A. Chodos, R. Jaffe, K. Johnson, and C. Thorn, Phys. Rev. D **10**, 2599 (1974).
- [7] L. L. Ferreira, J. Helayyel, and N. Zagury, Nuovo Chim. A **55**, 215 (1980).
- [8] W. Weise, International Review on Nuclear Physics **1**, 116 (1984).
- [9] P. D. Group, Phys. Lett. B **667**, 1075 (2008).
- [10] K. Brueckner, Phys. Rev. **86**, 106 (1952).
- [11] T.-S. H. Lee, A. Matsuyama, and T. Sato, Phys. Rep. **439**, 193 (2007).
- [12] J. J. Sakurai, *Modern Quantum Mechanics* (Addison-Wesley Publishing Company, Inc., 1994).
- [13] R. Shankar, *Principles of Quantum Mechanics* (Springer Science+Business Media. Inc., 1994).
- [14] M. E. Peskin and D. V. Schroeder, *An Introduction to Quantum Field Theory* (Westview Press, 1995).

- [15] J. J. Sakurai, *Advanced Quantum Mechanics* (Addison-Wesley Publishing Company, Inc., 1967).
- [16] J. R. Taylor, *Scattering Theory* (Dover Publications, Inc., 1972).
- [17] J. Mathews and R. Walker, *Standard Mathematical Tables* (McGraw-Hill, Inc., 1954).
- [18] O. Hanstein, D. Drechsel, and L. Tiator, Nucl. Phys. A **632**, 561 (1998).
- [19] I. G. Aznauryan, Phys. Rev. C **57**, 2727 (1998).
- [20] I. G. Aznauryan *et al.*, Phys. Rev. C **67**, 015209 (2003).
- [21] I. G. Aznauryan *et al.*, Phys. Rev. C **68**, 065204 (2003).
- [22] R. A. Arndt *et al.*, Phys. Rev. C **52**, 2120 (1995).
- [23] R. A. Arndt *et al.*, Phys. Rev. C **52 or 53**, 430 (1996).
- [24] R. A. Arndt *et al.*, Mod. Phys. A **18** (2003).
- [25] D. Manley, Int. J. Mod. Phys. A **18**, 441 (2003).
- [26] D. Manley and E. Saleski, Phys. Rev. D **45**, 4002 (1992).
- [27] F. Feuster and U. Mosel, Phys. Rev. C **58**, 457 (1998).
- [28] F. Feuster and U. Mosel, Phys. Rev. C **59**, 460 (1999).
- [29] G. Penner and U. Mosel, Phys. Rev. C **66**, 055211 (2002).
- [30] G. Penner and U. Mosel, Phys. Rev. C **66**, 055212 (2002).
- [31] R. L. Walker, Phys. Rev. **182**, 1729 (1969).
- [32] D. Drechsel, Nucl. Phys. A **645**, 145 (1999).
- [33] R. E. Cutkosky *et al.*, Phys. Rev. D **20**, 2839 (1979).
- [34] M. Batimic, I. Slaus, and A. Svarc, Phys. Rev. C **20**, 2310 (1995).
- [35] T. Vrama, S. Dytman, and T.-S. H. Lee, Phys. Rep. **328**, 181 (2000).

- [36] D. Drechsel, O. Hanstein, S. Kamalov, and L. Tiator, Nucl. Phys. A **645**, 145 (2007).
- [37] H. Tanabe and T. Ohta, Phys. Rev. C **31**, 1876 (1985).
- [38] S. Yang, J. Phys. G **11**, L200 (1985).
- [39] S. Nozawa, B.Blankenleider, and T.-S.H.Lee, Nucl. Phys. A **513**, 459 (1990).
- [40] F.Gross and Y.Surya, Phys. Rev. C **47**, 703 (1993).
- [41] F.Gross and Y.Surya, Phys. Rev. C **53**, 2422 (1996).
- [42] T.Sato and T.-S.H.Lee, Phys. Rev. C **54**, 2660 (1996).
- [43] T.Yoshimoto, T.Sato, M.Arima, and T.-S.H.Lee, Phys. Rev. C **61**, 065203 (2000).
- [44] T.Sato and T.-S.H.Lee, Phys. Rev. C **63**, 055201 (2001).
- [45] S.S.Kamalov and S.N.Yang, Phys. Rev. Lett. **83**, 4494 (1999).
- [46] G.-Y. Chen, S.S.Kamalov, S.N.Yang, D.Drechsel, and L.Tiator, Nucl. Phys. A **723**, 447 (2003).
- [47] W.-T. Chiang, F. Tabakin, T.-S.H.Lee, and B.Saghai, Phys. Lett. B **517**, 101 (2001).
- [48] M.G.Fuda and H.Alharbi, Phys. Rev. C **68**, 064002 (2003).
- [49] N.Kaiser, P.B.Siegel, and W.Weise, Nucl. Phys. A **594**, 325 (1995).
- [50] N.Kaiser, T.Waas, and W.Weise, Nucl. Phys. A **612**, 297 (1997).
- [51] E.Oset and A.Ramos, Nucl. Phys. A **635**, 99 (1998).
- [52] V. Burkert and T.-S. H. Lee, Int. J. Mod. Phys. E **13**, 1035 (2004).
- [53] G. Penner, (2002), Vector Meson Production and Nucleon Resonance Analysis in a Coupled-Channel Approach.
- [54] M. W.Paris and R. L. Workman, Phys. Rev. C **82**, 035202 (2010).

- [55] D. Drechsel, S. Kamalov, and L. Tiator, Phys. Rev. **106**, 27 (2007).
- [56] S.S.Kamalov, S.N.Yang, D.Drechsel, O.Hanstein, and L.Tiator, Phys. Rev. C **64**, 032201(R) (2001).
- [57] G. F. Chew, M. L. Goldberger, F. E. Low, and Y. Nambu, Phys. Rev. **106**, 1337 (1957).
- [58] G. F. Chew, M. L. Goldberger, F. E. Low, and Y. Nambu, Phys. Rev. **106**, 1345 (1957).
- [59] F. Tabakin and W. Chiang, Phys. Rev. C **55**, 2054 (1997).
- [60] F. Tabakin, C. Fasano, and B. Saghai, Phys. Rev. C **46**, 2430 (1992).
- [61] I. S. Berker, A. Donnachie, and J. K. Storrow, Nucl. Phys. B **95**, 347 (1975).
- [62] R. P. Worden, Nucl. Phys. B **37**, 253 (1972).
- [63] Proposal, E-03-105.
- [64] Proposal, E-04-102.
- [65] Proposal, E-05-012.
- [66] Proposal, E-89-004.
- [67] Proposal, E-02-112.
- [68] Proposal, E-06-013.
- [69] L. C. Maximon and H. Olsen, Phys. Rev. **114**, 887 (1959).
- [70] F. J. Klein *et al.*, (2002), E-02-112.
- [71] D. G. Crabb and W. Meyer, Ann. Rev. Nucl. Part. Sci. **47**, 67 (1997).
- [72] G. R. Court, Nucl. Instr. Meth. **A**, 433 (1993).
- [73] E. S. Smith *et al.*, Nucl. Instr. Meth. A **503**, 513 (2003), CLAS Collaboration.

- [74] B. Mecking *et al.*, Prog. Part. Nucl. Phys. **34**, 53 (1995).
- [75] J. Alcorn *et al.*, Nucl. Instr. Meth. A **522**, 294 (2004).
- [76] O. K. Baker *et al.*, Nucl. Instr. Meth. A **367**, 92 (1995).
- [77] F. Barbosa *et al.*, Nucl. Instr. Meth. A **323**, 191 (1992).
- [78] M. D. Mestayer *et al.*, Nucl. Instr. Meth. A **449**, 81 (2000).
- [79] G. Heath, Nucl. Instr. Meth. A **A**, 431 (1989).
- [80] D. Doughty(Jr.) *et al.*, IEEE Trans. Nucl. Sci. **NS**, 241 (1992).
- [81] D. Doughty(Jr.) *et al.*, IEEE Trans. Nucl. Sci. **NS**, 680 (1993).
- [82] D. Doughty(Jr.) *et al.*, IEEE Trans. Nucl. Sci. **NS**, 267 (1994).
- [83] D. Doughty(Jr.) *et al.*, IEEE Trans. Nucl. Sci. **NS**, 111 (1996).
- [84] S. Taylor *et al.*, Nucl. Instr. Meth. A **462**, 484 (2001).
- [85] Y. Sharabian *et al.*, Nucl. Instr. Meth. A **556**, 246 (2006).
- [86] E. S. Smith *et al.*, Nucl. Instr. Meth. A **432**, 265 (1999).
- [87] G. Adams *et al.*, Nucl. Instr. Meth. A **465**, 414 (2001).
- [88] M. Amarian *et al.*, Nucl. Instr. Meth. A **460**, 239 (2001).
- [89] M. Anghinolfi *et al.*, Nucl. Instr. Meth. A **537**, 562 (2005).
- [90] R. Nasseripour *et al.*, Bull. Am. Phys. Soc **45**, 91 (2000).
- [91] D. I. Sober *et al.*, Nucl. Instr. Meth. A **440**, 263 (2000).
- [92] K. Livingston, Nucl. Instr. Meth. A **603**, 205 (2009).
- [93] F. A. Natter *et al.*, Nucl. Instr. Meth. B **211**, 465 (2003).
- [94] D. Cords *et al.*, CLAS note (1994), 94-012.
- [95] M. Anghinolfi, M. Baattaglieri, and R. D. Vita, CLAS note (2000).

- [96] P. R. Bevington and D. K. Robinson, *Data Reduction and Error Analysis for Physical Science* (WCB/McGraw-Hill, 1992).
- [97] FROST group, http://www.jlab.org/~clasg9/g9a_allruns.dat, target polarization of g9a.
- [98] J. Ahrens *et al.*, Phys. Rev. Lett. **84**, 5950 (2000).
- [99] J. Ahrens *et al.*, Phys. Rev. Lett. **87**, 022003 (2001).
- [100] J. Ahrens *et al.*, Phys. Rev. Lett. **88**, 232002 (2002).
- [101] C. Keith, <http://www.jlab.org/~ckcith/Frozen/Frozen.html>, Jefferson Lab Frozen Spin Target.
- [102] M. L. Goldberger and K. M. Watson, *Collision Theory* (John Wiley and Sons, Inc., 1964).
- [103] M. Jacob and G. C. Wick, Annals Phys. **7**, 404 (1959).
- [104] S. Gerasimov, Sov. J. Nucl. Phys. **2**, 430 (1996).
- [105] S. Drell and A. Hearn, Phys. Rev. Lett. **16**, 908 (1996).

Appendix A

Double polarization observables

The expressions for the sixteen spin observables are given with the differential cross section $\mathcal{I}(\theta)$ [60] for simplicity.

A.1 Using electric and magnetic multipole amplitudes

The spin observables (beam-target polarization) are given in terms of electric and magnetic multipole amplitudes and as expansions in $x = \cos \theta$. The Eq. 3.9 are used with $L \leq 1$.

A.2 Observables using CGLN amplitudes

The spin observables are given in terms of four CGLN amplitudes where $x = \cos \theta$, and $\frac{q}{k}$ is the ratio of the final to initial state momenta.

Table A.1: The spin observables in terms of Electromagnetic multipole amplitudes [60].

Spin observables	EM representation
$\mathcal{I}(\theta) =$	$Re\{ E_0^+ ^2 + \frac{9}{2} E_1^+ ^2 + M_1^- ^2 + \frac{5}{2} M_1^+ ^2 + M_1^{-*}(3E_1^+ + M_1^+) - 3E_1^{+*}M_1^+ + x[2E_0^{+*}(3E_1^+ + M_1^+) - 2E_0^{+*}M_1^-] + x^2[\frac{9}{2} E_1^+ ^2 - \frac{3}{2} M_1^+ ^2 - 3M_1^{-*}(3E_1^+ + M_1^+) + 9E_1^{+*}M_1^+]\}$
$\mathbf{PI} =$	$-\sin\theta Im\{(E_0^{+*} - 3xM_1^{-*})(3E_1^+ + 2M_1^- + M_1^+)\}$
$\Sigma\mathcal{I} =$	$\frac{3\sin^2\theta}{2} Re\{-3 E_1^+ ^2 + M_1^- ^2 - 2M_1^{-*}(E_1^+ - M_1^+) + 2E_1^{+*}M_1^+\}$
$\mathbf{TI} =$	$3\sin\theta Im\{E_0^{+*}(E_1^+ - M_1^+) - x[M_1^{-*}(E_1^+ - M_1^+) - 4M_1^{+*}E_1^+]\}$
$\mathbf{EI} =$	$Re\{- E_0^+ ^2 - M_1^- ^2 + 2 M_1^+ ^2 - M_1^{-*}(3E_1^+ + M_1^+) - 6E_1^{+*}M_1^+ - x[2E_0^{+*}(3E_1^+ + M_1^+) - 2E_0^{+*}M_1^-] + x^2[-9 E_1^+ ^2 - 3 M_1^+ ^2 + 3M_1^{-*}(3E_1^+ + M_1^+)]\}$
$\mathbf{GI} =$	$3\sin^2\theta Im\{M_1^{-*}(E_1^+ - M_1^+) - 2E_1^{+*}M_1^+\}$
$\mathbf{HI} =$	$-\sin\theta Im\{(E_0^{+*} - 3xM_1^{-*})(3E_1^+ + 2M_1^- + M_1^+)\}$
$\mathbf{FI} =$	$3\sin\theta Re\{E_0^{+*}(E_1^+ - M_1^+) + x[3 E_1^+ ^2 - M_1^+ ^2 - M_1^{-*}(E_1^+ - M_1^+) - 2E_1^{+*}M_1^+]\}$

Table A.2: The spin observables in terms of CGLN amplitudes [60].

Spin observables	CGLN representation
$\mathcal{I}(\theta) =$	$Re\{ \mathcal{F}_1 ^2 + \mathcal{F}_1 ^2 - 2x\mathcal{F}_2\mathcal{F}_1^* + \frac{\sin^2\theta}{2}[\mathcal{F}_3 ^2 + \mathcal{F}_4 ^2 + x\mathcal{F}_4\mathcal{F}_1^* + x\mathcal{F}_3\mathcal{F}_2^* + 2x\mathcal{F}_4\mathcal{F}_3^*]\}$
$\frac{d\sigma_0}{d\Omega} =$	$\frac{q}{k}\mathcal{I}(\theta)$
$\mathbf{PI} =$	$\sin\theta Im\{[2\mathcal{F}_2 + \mathcal{F}_3 + x\mathcal{F}_4]^*\mathcal{F}_1 + \mathcal{F}_2^*(x\mathcal{F}_3 + \mathcal{F}_4) + \sin^2\theta\mathcal{F}_3^*\mathcal{F}_4\}$
$\mathbf{\Sigma I} =$	$-\frac{\sin^2\theta}{2} Re\{ \mathcal{F}_3 ^2 + \mathcal{F}_4 ^2 + 2[\mathcal{F}_1^*\mathcal{F}_4 + \mathcal{F}_2^*\mathcal{F}_3 + x\mathcal{F}_3^*\mathcal{F}_4]\}$
$\mathbf{TI} =$	$\sin\theta Im\{\mathcal{F}_1^*\mathcal{F}_3 - \mathcal{F}_2^*\mathcal{F}_4 + x(\mathcal{F}_1^*\mathcal{F}_4 - \mathcal{F}_2^*\mathcal{F}_3) - \sin^2\theta\mathcal{F}_3^*\mathcal{F}_4\}$
$\mathbf{EI} =$	$-Re\{ \mathcal{F}_1 ^2 + \mathcal{F}_2 ^2 - 2x\mathcal{F}_2\mathcal{F}_1^* + \sin^2\theta(\mathcal{F}_1\mathcal{F}_4^* + \mathcal{F}_2\mathcal{F}_3^*)\}$
$\mathbf{GI} =$	$-\sin^2\theta Im\{\mathcal{F}_1\mathcal{F}_4^* + \mathcal{F}_2\mathcal{F}_3^*\}$
$\mathbf{HI} =$	$\sin\theta Im\{\mathcal{F}_1[\mathcal{F}_2 + \mathcal{F}_3 + x\mathcal{F}_4]^* - \mathcal{F}_2[\mathcal{F}_1 + \mathcal{F}_4 + x\mathcal{F}_3]^*\}$
$\mathbf{FI} =$	$\sin\theta Re\{\mathcal{F}_1[\mathcal{F}_2 + \mathcal{F}_3 + x\mathcal{F}_4]^* - \mathcal{F}_2[\mathcal{F}_1 + \mathcal{F}_4 + x\mathcal{F}_3]^*\}$
$\mathbf{O}_{x'}\mathcal{I} =$	$\sin\theta Im\{\mathcal{F}_2\mathcal{F}_3^* - \mathcal{F}_1\mathcal{F}_4^* + x(\mathcal{F}_2\mathcal{F}_4^* - \mathcal{F}_1\mathcal{F}_3^*)\}$
$\mathbf{C}_{x'}\mathcal{I} =$	$\sin\theta Re\{ \mathcal{F}_2 ^2 - \mathcal{F}_1 ^2 + \mathcal{F}_2\mathcal{F}_3^* - \mathcal{F}_1\mathcal{F}_4^* + x(\mathcal{F}_2\mathcal{F}_4^* - \mathcal{F}_1\mathcal{F}_3^*)\}$
$\mathbf{O}_{z'}\mathcal{I} =$	$-\sin^2\theta Im\{\mathcal{F}_1\mathcal{F}_3^* + \mathcal{F}_2\mathcal{F}_4^*\}$
$\mathbf{C}_{z'}\mathcal{I} =$	$Re\{-2\mathcal{F}_1\mathcal{F}_2^* + x \mathcal{F}_1 ^2 + x \mathcal{F}_2 ^2 - \sin^2\theta(\mathcal{F}_1\mathcal{F}_3^* + \mathcal{F}_2\mathcal{F}_4^*)\}$
$\mathbf{T}_{x'}\mathcal{I} =$	$-\frac{\sin^2\theta}{2} Re\{x(\mathcal{F}_3 ^2 + \mathcal{F}_4 ^2) + 2(\mathcal{F}_3\mathcal{F}_4^* + \mathcal{F}_1\mathcal{F}_3^* + \mathcal{F}_2\mathcal{F}_4^*)\}$
$\mathbf{T}_{z'}\mathcal{I} =$	$\sin\theta Re\{\frac{\sin^2\theta}{2}(\mathcal{F}_4 ^2 - \mathcal{F}_3 ^2) + (\mathcal{F}_1\mathcal{F}_4^* - \mathcal{F}_2\mathcal{F}_3^*) + x(\mathcal{F}_1\mathcal{F}_3^* - \mathcal{F}_2\mathcal{F}_4^*)\}$
$\mathbf{L}_{x'}\mathcal{I} =$	$\sin\theta Re\{ \mathcal{F}_1 ^2 - \mathcal{F}_2 ^2 + (\mathcal{F}_1\mathcal{F}_4^* - \mathcal{F}_2\mathcal{F}_3^*) + x(\mathcal{F}_1\mathcal{F}_3^* - \mathcal{F}_2\mathcal{F}_4^*) + \frac{\sin^2\theta}{2}(\mathcal{F}_4 ^2 - \mathcal{F}_3 ^2)\}$
$\mathbf{L}_{z'}\mathcal{I} =$	$Re\{2\mathcal{F}_1\mathcal{F}_2^* - x(\mathcal{F}_1 ^2 + \mathcal{F}_2 ^2) + \sin^2\theta[\frac{x}{2}(\mathcal{F}_3 ^2 + \mathcal{F}_4 ^2) + \mathcal{F}_1\mathcal{F}_3^* + \mathcal{F}_2\mathcal{F}_4^* + \mathcal{F}_3\mathcal{F}_4^*]\}$

Appendix B

Isospin amplitude

The isospin amplitudes are used in analyzing pseudo-scalar meson productions, such as π , η , K in order to understand the resonance properties of the nucleon. Isospin is used since it is conserved to a good approximation in the strong interaction. The hadron current matrix elements can be written as

$$\epsilon_\mu(q)J^\mu(k, p'; q, p) = \sum_{i=1,6} \bar{u}(\mathbf{p}') [A_i(s, t, u) M_i] u(\mathbf{p}) \quad (\text{B.1})$$

because of Lorentz invariance and gauge invariance. In Eq. (B.1),

$u(\mathbf{p})$: the Dirac spinor,

$A_i(s, t, u)$: Lorentz invariant functions,

M_i : independent invariants formed from γ^μ , γ_5 , and momentum variables. (B.2)

The initial state is characterized by the target nucleon, which is total isospin $1/2$ and isospin projection $\pm 1/2$ for proton/neutron. Its isospin couples to the electromagnetic current with isospin structure containing isoscalar and isovector components. The pion in the final state is an isovector particle. Assuming isospin conservation in the hadronic system, the interaction in the isospace has to be $\boldsymbol{\tau} \cdot \boldsymbol{\Phi}$, where $\boldsymbol{\tau}$ is the isospin Pauli operator and $\boldsymbol{\Phi}$ is an isovector particle.

The amplitudes can be further classified by isospin quantum numbers for π production. The amplitude $A^{(0)}$ is for the isoscalar photon, the amplitudes $A^{(1/2)}$ and $A^{(3/2)}$ are for the isovector for the final πN system with total isospin $I = 1/2$ and $I = 3/2$, respectively. Each invariant amplitude in Eq. (B.1) can be expanded as

$$A_i = \frac{1}{2} A_i^{(-)} [\tau_\alpha, \tau_3] + A_i^{(+)} \delta_{\alpha,3} + A_i^{(0)} \tau_\alpha, \quad (\text{B.3})$$

where α is the isospin quantum number associated with the produced pion. From Eq. B.3:

$$\begin{aligned} A_i^{(1/2)} &= A_i^{(+)} + 2A_i^{(-)} \\ A_i^{(3/2)} &= A_i^{(+)} - A_i^{(-)}. \end{aligned} \quad (\text{B.4})$$

For proton and neutron amplitudes, $A_{p,i}^{(1/2)}$ and $A_{n,i}^{(1/2)}$, respectively, with total isospin $I = 1/2$ we have:

$$\begin{aligned} A_{p,i}^{(1/2)} &= A_i^{(0)} + \frac{1}{3}A_i^{(1/2)} \\ A_{n,i}^{(1/2)} &= A_i^{(0)} - \frac{1}{3}A_i^{(1/2)}. \end{aligned} \quad (\text{B.5})$$

Thus, the amplitudes for one pion photo-production can be written as:

$$\begin{aligned} A_i(\gamma^*p \rightarrow n\pi^+) &= \sqrt{2}[A_{p,i}^{(1/2)} - \frac{1}{3}A_i^{(3/2)}] \\ A_i(\gamma^*p \rightarrow p\pi^0) &= A_{p,i}^{(1/2)} + \frac{2}{3}A_i^{(3/2)} \\ A_i(\gamma^*n \rightarrow p\pi^-) &= \sqrt{2}[A_{n,i}^{(1/2)} + \frac{1}{3}A_i^{(3/2)}] \\ A_i(\gamma^*n \rightarrow n\pi^0) &= -A_{n,i}^{(1/2)} + \frac{2}{3}A_i^{(3/2)}. \end{aligned} \quad (\text{B.6})$$

Neglecting isospin symmetry breaking forces, all invariants and multipole amplitudes can be decomposed into the isospin amplitudes.

Appendix C

Error Calculation and Formulae

C.1 Error Calculation

Error is the difference between an observed value and the true value. I used error propagation equation for the error calculation of the asymmetry E,

$$f(N_{1/2}, N_{3/2}) \equiv \frac{f(N_{3/2} - N_{1/2})}{f(N_{3/2} + N_{1/2})} \quad (\text{C.1})$$

where

$N_{1/2}$ and $N_{3/2}$ is the number of counts whose total helicity state is $\frac{1}{2}$ and $\frac{3}{2}$, respectively. The error propagation equation for asymmetry E $f(N_{1/2}, N_{3/2})$:

$$\begin{aligned} \sigma_f^2 &\simeq \sigma_{1/2}^2 \left(\frac{\partial f}{\partial N_{1/2}} \right)^2 + \sigma_{3/2}^2 \left(\frac{\partial f}{\partial N_{3/2}} \right)^2 \\ &= \sigma_{1/2}^2 \left(\frac{(-2)N_{3/2}}{N^2} \right)^2 + \sigma_{3/2}^2 \left(\frac{2N_{1/2}}{N^2} \right)^2 \\ &= \frac{4}{N^2} [\sigma_{1/2}^2 (N_{3/2})^2 + \sigma_{3/2}^2 (N_{1/2})^2] \\ &= \frac{4N_{1/2}N_{3/2}}{N^3} \end{aligned} \quad (\text{C.2})$$

where $N = N_{1/2} + N_{3/2}$. Using the Poisson distribution, $\sigma_{1/2} = \sqrt{N_{1/2}}$ and $\sigma_{3/2} = \sqrt{N_{3/2}}$, the uncertainty is:

$$\sigma_f \simeq \sqrt{\frac{4N_{1/2}N_{3/2}}{N^3}} \quad (\text{C.3})$$

C.2 Wigner d - functions

The Wigner functions [12, 102, 103]

$$\mathfrak{D}_{mm'}^j(\alpha, \beta, \alpha) = e^{-i\alpha m} d_{mm'}^j(\beta) e^{-i\alpha m'} \quad (\text{C.4})$$

are the matrix elements of a rotation. This transforms the $|j, m\rangle$ component of the unit vector \mathbf{e}_z into the $|j, m'\rangle$ component of the unit vector $(\cos \alpha \sin \beta, \sin \alpha \sin \beta, \cos \beta)$. In the Wigner Simplified Rotation Matrices (d -functions), the non-trivial part of the Wigner functions is contained. The Wigner d -functions describe the middle rotation about the y -axis, which mixes different M - values. They are given by in general:

$$d_{\lambda\lambda'}^j(\theta) = \sum_k (-1)^{k+\lambda-\lambda'} \frac{\sqrt{(j+\lambda)!(j-\lambda)!(j+\lambda')!(j-\lambda')!}}{(j-\lambda-k)!(j+\lambda'-k)!(k+\lambda-\lambda')!k!} \times \left(\cos \frac{\theta}{2}\right)^{2j-2k+\lambda'-\lambda} \left(\sin \frac{\theta}{2}\right)^{2k+\lambda-\lambda'} \quad (\text{C.5})$$

C.2.1 Properties

Some important properties of Wigner d - functions are:

$$\begin{aligned} d_{\lambda\lambda'}^j(\theta) &= d_{-\lambda'-\lambda}^j(\theta) \\ d_{\lambda\lambda'}^j(\theta) &= (-1)^{\lambda-\lambda'} d_{\lambda'\lambda}^j(\theta) = (-1)^{\lambda-\lambda'} d_{-\lambda-\lambda'}^j(\theta) \\ d_{\lambda\lambda'}^j(\theta) &= d_{\lambda\lambda'}^j(-\theta) \\ d_{\lambda\lambda'}^j(\theta) &= (-1)^{j+\lambda} d_{\lambda-\lambda'}^j(\pi - \theta) \\ d_{\lambda\lambda'}^j(180^\circ) &= (-1)^{j-\lambda'} \delta_{\lambda-\lambda'} \\ d_{\lambda\lambda'}^j(0^\circ) &= (-1)^{j+\lambda} d_{\lambda-\lambda'}^j(180^\circ) = (-1)^{j+\lambda-j-\lambda'} \delta_{\lambda\lambda'} = (-1)^{\lambda-\lambda'} \delta_{\lambda\lambda'} = \delta_{\lambda\lambda'} \end{aligned} \quad (\text{C.6})$$

C.3 Cross section

The differential cross section in the symbolic form is

$$d\sigma = \frac{|\mathcal{M}|^2}{F} dLips \quad (\text{C.7})$$

where $dLips$ is the Lorentz invariant phase space factor and F is the incident flux in the laboratory.

$$\begin{aligned}
dLips &= (2\pi)^4 \delta^{(4)}(p_c + p_D - p_A - p_B) \frac{d^3 \mathbf{p}_C}{(2\pi)^3 2E_C} \frac{d^3 \mathbf{p}_D}{(2\pi)^3 2E_D} \\
F &= |\mathbf{v}_A - \mathbf{v}_B| \cdot 2E_A \cdot 2E_B \\
&= \left| \frac{\mathbf{p}_A}{E_A} - \frac{\mathbf{p}_B}{E_B} \right| \cdot 2E_A \cdot 2E_B \\
&= 4|\mathbf{p}_A|E_B + |\mathbf{p}_B|E_A \\
&= [(p_A \cdot p_B)^2 - m_A^2 m_B^2]^{1/2}
\end{aligned} \tag{C.8}$$

The differential cross section in the c.m. system with $|\mathbf{p}_a| = |\mathbf{p}_b| = p_i$, $|\mathbf{p}_c| = |\mathbf{p}_d| = p_f$, $s = (E_a + E_b)^2 = (E_c + E_d)^2$, and $d\Omega$ as a element of solid angle about \mathbf{p}_c is:

$$\begin{aligned}
dLips &= (2\pi)^4 \delta^{(4)}(p_c + p_d - p_a - p_b) \frac{d^3 \mathbf{p}_c}{(2\pi)^3 2E_c} \frac{d^3 \mathbf{p}_d}{(2\pi)^3 2E_d} \\
&= \frac{1}{(2\pi)^2} \frac{\delta(E_c + E_d - E_a - E_b) d^3 \mathbf{p}_c \delta^{(3)}(\mathbf{p}_c + \mathbf{p}_d - \mathbf{p}_a - \mathbf{p}_b) d^3 \mathbf{p}_d}{4E_c E_d} \\
&= \frac{1}{(2\pi)^2} \frac{d^3 \mathbf{p}_c}{4E_c E_d} \delta(E_c + E_d - E_a - E_b)
\end{aligned} \tag{C.9}$$

using $d^3 \mathbf{p}_c = p_f^2 dp_f d\Omega$

$$dLips = \frac{1}{(2\pi)^2} \frac{p_f^2 dp_f}{4E_c E_d} \delta(E_c + E_d - \sqrt{s}) d\Omega \tag{C.10}$$

using

$$\begin{aligned}
\frac{d\sqrt{s}}{dp_f} &= \frac{d(E_c + E_d)}{dp_f} = \frac{d(\sqrt{p_f^2 + m_c^2} + \sqrt{p_f^2 + m_d^2})}{dp_f} = p_f \left(\frac{1}{E_c} + \frac{1}{E_d} \right) = \frac{p_f \sqrt{s}}{E_c E_d} \\
\Rightarrow \frac{p_f^2 dp_f}{E_c E_d} &= \frac{d\sqrt{s}}{\sqrt{s}}
\end{aligned} \tag{C.11}$$

$$\begin{aligned}
dLips &= \frac{1}{(2\pi)^2} \frac{p_f d\Omega}{4\sqrt{s}} \delta(E_c + E_d - \sqrt{s}) d\sqrt{s} \\
&= \frac{1}{(2\pi)^2} \frac{p_f}{4\sqrt{s}} d\Omega
\end{aligned} \tag{C.12}$$

$$\begin{aligned}
F &= 4[(p_a \cdot p_b)^2 - m_a^2 m_b^2]^{1/2} \\
&= 4[(E_a E_b + p_i^2)^2 - (E_a^2 - p_i^2)(E_b^2 - p_i^2)]^{1/2} \\
&= 4[p_i^2 E_a E_b + p_i^2(E_a^2 + E_b^2)]^{1/2} \\
&= 4p_i(E_a + E_b) \\
&= 4p_i\sqrt{s}
\end{aligned} \tag{C.13}$$

Therefore, the cross section for the reaction $a + b \rightarrow c + d$ in the c.m. frame is:

$$\left(\frac{d\sigma}{d\Omega}\right)_{cm} = \frac{|\mathcal{M}|^2}{4p_i\sqrt{s}} \frac{1}{4\pi^2} \frac{p_f}{4\sqrt{s}} = \frac{1}{64\pi^2 s} \frac{p_f}{p_i} |\mathcal{M}|^2 \tag{C.14}$$

Appendix D

GDH Sum Rule

D.0.0.1 GDH sum rule

Since the result of asymmetry E will be compared with the data of MAMI (see section 8.2.2), whose experiment was done to check the GDH sum rule, this rule is summarized in this section. The GDH sum rule is based on basic physics principles, Lorentz and gauge invariance, unitarity, and causality, applied to the forward Compton scattering amplitude. This amplitude becomes spin independent at infinite photon energies. The prediction provides an excellent test of the nucleon spin structure because of its fundamental character. This sum rule, derived in the 1960s by Gerasimov[104] and independently by Drell and Hearn[105], relates static properties of the nucleon, the anomalous magnetic moment (κ_p), the charge (e), and mass (M_p), to the difference in the total photoabsorption on longitudinally polarized nucleons. It is written as

$$\int_{\nu_0}^{\infty} \frac{d\nu}{\nu} [\sigma_{3/2} - \sigma_{1/2}] = \frac{2\pi^2\alpha}{M_p^2} \kappa_p^2, \quad (\text{D.1})$$

where ν , $\sigma_{3/2}$ and $\sigma_{1/2}$ are the photon energy, the photoabsorption cross sections for the total helicity states 3/2 and 1/2, respectively. The experimental result (Helbing, 2006) shows remarkable agreement with the theoretical calculation.